SPATIO-TEMPORAL CHARACTERIZATION OF FRACTAL INTRA-URBAN HEAT ISLETS

A Dissertation

Submitted to the Faculty

of

Purdue University

by

Anamika Shreevastava

In Partial Fulfillment of the

Requirements for the Degree

of

Doctor of Philosophy

December 2020

Purdue University

West Lafayette, Indiana

THE PURDUE UNIVERSITY GRADUATE SCHOOL
STATEMENT OF APPROVAL

Dr. P. Suresh C. Rao, Advisor

Lyles School of Civil Engineering, Purdue University

Dr. Matthew Huber

Dept. of Earth, Atmospheric, and Planetary Sciences, Purdue University

Dr. Joaquín C. Goñi

Department of Industrial Engineering, Purdue University

Dr. Gavan S. McGrath

Department of Biodiversity Conservation, Government of Western Australia

Dr. Prathap Ramamurthy

Department of Mechanical Engineering, City College New York

Approved by:

Dr. Linda S. Lee

Head of the ESE Interdisciplinary Program, Purdue University

TABLE OF CONTENTS

Page

LIST OF FIGURES

Figure Page

Figure Page

Figure Page

Figure Page

Figure Page

Figure Page

Figure Page

ABBREVIATIONS

BEP	Building Effect Parametrization
BEM	Building Energy Modeling
GOES	Geostationary Operational Environmental Satellite
LCZ	Local Climate Zone
LST	Land Surface Temperature
LULC	Land Use Land Cover
MODIS	Moderate Resolution Imaging Spectro-radiometer
SUHI	Surface Urban Heat Island
T2	Air temperature at 2 meters
UHI	Urban Heat Island
WRF	Weather Research Forecast
WUDAPT	World Urban Database Access and Portal Tools

ABSTRACT

Shreevastava, Anamika Ph.D., Purdue University, December 2020. Spatio-Temporal Characterization of Fractal intra-Urban Heat Islets. Major Professor: P. Suresh C. Rao.

Extreme heat is one of the deadliest health hazards that is projected to increase in intensity and persistence in the near future. Temperatures are further exacerbated in the urban areas due to the Urban Heat Island (UHI) effect resulting in increased heat-related mortality and morbidity. However, the spatial distribution of urban temperatures is highly heterogeneous. As a result, metrics such as UHI Intensity that quantify the difference between the average urban and non-urban air temperatures, often fail to characterize this spatial and temporal heterogeneity. My objective in this thesis is to understand and characterize the spatio-temporal dynamics of UHI for cities across the world. This has several applications, such as targeted heat mitigation, energy load estimation, and neighborhood-level vulnerability estimation.

Towards this end, I have developed a novel multi-scale framework of identifying emerging heat clusters at various percentile-based thermal thresholds (T_{thr}) and refer to them collectively as *intra-Urban Heat Islets*. Using the Land Surface Temperatures from Landsat for 78 cities representative of the global diversity, I have showed that the heat islets have a fractal spatial structure. They display properties analogous to that of a percolating system as T_{thr} varies. At the percolation threshold, the size distribution of these islets in all cities follows a power-law, with a scaling exponent $\sim$ 1.88 and an aggregated Area-Perimeter Fractal Dimension $\sim$ 1.33. This commonality indicates that despite the diversity in urban form and function across the world, the urban temperature patterns are different realizations with the same aggregated statistical properties. In addition, analogous to the UHI Intensity, the mean islet intensity, i.e., the difference between mean islet temperature and thermal threshold,

is estimated for each islet, and their distribution follows an exponential curve. This allows for a single metric (exponential rate parameter) to serve as a comprehensive measure of thermal heterogeneity and improve upon the traditional UHI Intensity as a bulk metric.

To study the impact of urban form on the heat islet characteristics, I have introduced a novel lacunarity-based metric, which quantifies the degree of compactness of the heat islets. I have shown that while the UHIs have similar fractal structure at their respective percolation threshold, differences across cities emerge when we shift the focus to the hottest islets ($T_{thr} = 90^{\text{th}}$ percentile). Analysis of heat islets' size distribution demonstrates the emergence of two classes where the dense cities maintain a power law, whereas the sprawling cities show an exponential deviation at higher thresholds. This indicates a significantly reduced probability of encountering large heat islets for sprawling cities. In contrast, analysis of heat islet intensity distributions indicates that while a sprawling configuration is favorable for reducing the mean Surface UHI Intensity of a city, for the same mean, it also results in higher local thermal extremes.

Lastly, I have examined the impact of external forcings such as heatwaves (HW) on the heat islet characteristics. As a case study, the European heatwave of 2018 is simulated using the Weather Research Forecast model with a focus on Paris. My results indicate that the UHI Intensity under this HW reduces during night time by 1°C on average. A surface energy budget analysis reveals that this is due to drier and hotter rural background temperatures during the HW period. To analyze the response of heat islets at every spatial scale, power spectral density analysis is done. The results show that large contiguous heat islets (city-scale) persist throughout the day during a HW, whereas the smaller islets (neighborhood-scale) display a diurnal variability that is the same as non-HW conditions.

In conclusion, I have presented a new viewpoint of the UHI as an *archipelago* of intra-urban heat islets. Along the way, I have introduced several properties that enable a seamless comparison of thermal heterogeneity across diverse cities as well

as under diverse climatic conditions. This thesis is a step towards a comprehensive characterization of heat from the spatial scales of an urban block to a megalopolis.

1. INTRODUCTION

Public interest in climate change impacts tends to be focused on rapid-onset disasters such as hurricanes, floods, and earthquakes. On the contrary, extreme heat is a slow-onset disaster that claims more lives than other natural hazards due to prolonged exposure[1]. More than 50% of the world's population currently resides in cities, and the number continues to increase rapidly with a projection that 70% of the global population will be urbanized by 2050 [1]. As urbanization is rapidly accelerating, cities face the growing burden of adapting to the *new normal* of scorching heat every summer, which is further exacerbated by the anthropogenic modifications of local weather. The impacts of extreme heat in cities range from increased energy consumption, critical pressure on power supply grids, and heat-related morbidity and mortality. As a result, the problem of urban heat has become an urgent scientific and societal issue. In this thesis, I focus on the intra-urban spatio-temporal complexity of extreme heat.

1.1 The Urban Heat Island

The first instance of anthropogenic modification of local weather was recorded in the form of Urban Heat Island (UHI) by Luke Howard in 1833. Cities ever since have only grown bigger, and their environmental impacts have become more visible. Several other pioneers, such as Oke, have investigated the occurrence and driving mechanisms of this phenomena and have built a sub-discipline, called *Urban Climate*, around it [2]. Formally defined as the excess heat in urban areas compared to its rural surroundings, UHIs have been observed and reported in a diverse range of cities, large or small, in warm or cold climates [3]. The main cause behind the excess heat

[1]Source: `https://www.weather.gov/hazstat/`

is increased absorption and storage of incoming solar radiation due to an excess of concrete, increased anthropogenic heat fluxes due to air-conditioning and vehicular emissions, coupled with decreased evapotranspiration and decreased wind-driven heat transport due to increased roughness of urban surfaces. It is known to be the strongest in the urban canopy layer, i.e., the region between the ground level and the mean roof height, where it is strongly influenced by local site characteristics such as building geometry and construction materials [4]. But it is also detectable in the boundary layer, which resides above the urban canopy, typically up to two kilometers [5].

The traditional approach used to quantify UHI is the metric UHI Intensity i.e., the difference between point measurements of temperature in a representative urban area and similar measurements in the surrounding non-urban environment [6]. However, urban areas are highly heterogeneous in nature, and the choice of a "representative" urban area can often lead to very different estimates that do not adequately describe the urban temperatures throughout a city. Notable efforts have been made at a city scale to collect data at a higher spatial sampling, such as the Basel Urban Boundary Layer Experiment [7], but such examples remain rare. Furthermore, the methods of collecting data are expensive and labor-intensive, thereby making it prohibitively difficult to replicate for other cities across the world.

As a solution to these limitation, the Surface UHI (SUHI), has emerged as an alternative metric [8, 9] . As elevated urban air temperatures characterize the atmospheric UHI, the SUHI refers to the increased Land Surface Temperatures (LST) compared to the rural areas. High-resolution Earth-monitoring satellites such as Landsat, Moderate Resolution Imaging Spectro-radiometer (MODIS), and Geostationary Operational Environmental Satellite (GOES) allow a broader coverage and more uniform sampling than in-situ data. Furthermore, globally consistent methods of observation enable inter-city comparison minimizing the challenge of maintaining data quality. Features within urban areas such as building roofs and wall exteriors, surface materials, albedo, impervious, and vegetated fractions determine the resultant LST within each pixel (resolution $\sim$ 90 m). In other words, LST observations

from satellites at the resolution should be interpreted as a resultant temperature of a heterogeneous urban block. Furthermore, while SUHI bears similarity in spatial and temporal patterns to UHI [6], LST is more coupled with urban form and function, whereas air temperatures are subject to the boundary layer wind profiles as well. Therefore, a point-to-point correspondence between the two can not be expected [10].

Lastly, modeling environments such as the Weather Research Forecast (WRF) model help in studying the phenomenon from a multi-dimensional perspective [11]. They assimilate surface and atmospheric boundary conditions using reanalysis datasets and estimate relevant fields such as LST, air temperature at a 2-meter height (T2), moisture, precipitation, and surface energy fluxes and provide a comprehensively modeled dataset for further diagnostics. Current modeling efforts for urban regions include the incorporation of high-resolution urban Land Use Land Cover (LULC) maps coupled with advanced urban surface parameterization schemes such as Building Effect Parameterization - Building Energy Model (BEP-BEM) into the WRF model [12]. A combination of satellite remote sensing and WRF model outputs are used as the main dataset for this thesis.

1.2 Spatial heterogeneity of urban temperatures

A version of this section is published in collaboration with the World Urban Database Access and Portal Tools (WUDAPT) in Bulletin of American Meteorological Society [2].

A growing body of heat mitigation research suggests that the UHI can be significantly reduced by altering parts of the urban form, increasing the albedo of bup ilt surfaces, and/or incorporating more vegetation within the city, to name a few [13–15]. However, the UHI is a collection of multiple hot and cold regions that emerge within the city. For example, a pond within a bustling urban area can serve as a heat

[2]Ching, J. et al., including Shreevastava, A. (2018). WUDAPT: An urban weather, climate, and environmental modeling infrastructure for the Anthropocene. Bulletin of the American Meteorological Society, 99(9), 1907-1924.

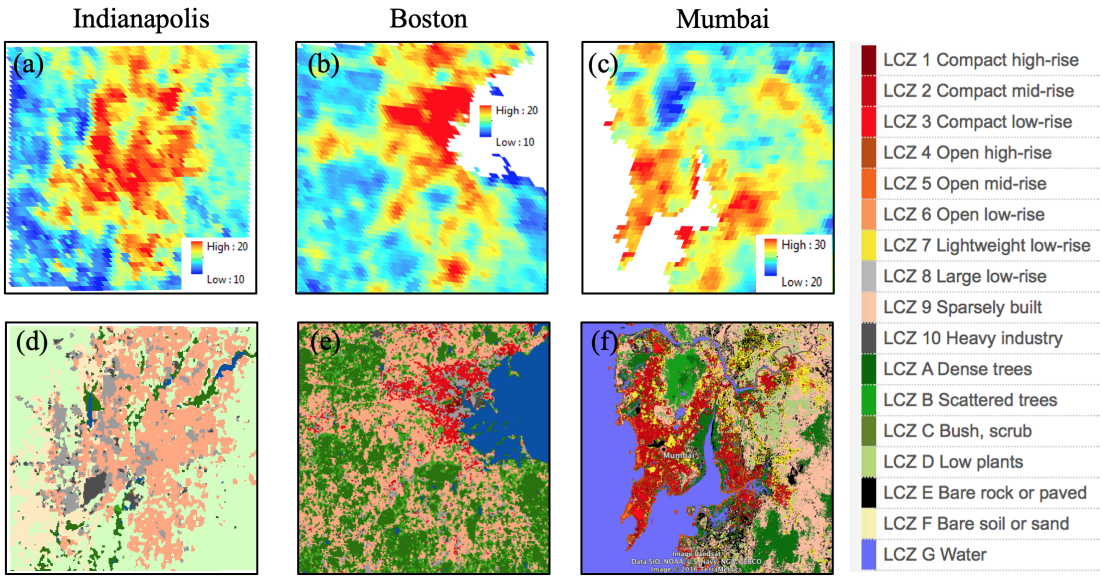

Figure 1.1. 8-day average surface temperature (in Celcius) derived from MODIS and Local Climate Zone maps for (a,d) Indianapolis, USA, (b,e) Boston, USA, and (c,f) Mumbai, India. The legend for LCZ classes is shown on the right. Note the elevated LSTs in regions corresponding to the urban LCZ classes. Resolution = 1 km.

sink within the heat island. Similarly, a hotter heat island such as downtown can peak above a larger UHI. In order to make informed, spatially optimized decisions regarding the areas where mitigation resources are most required and will be most effective, it is necessary to comprehensively characterize the spatial heterogeneity of urban temperatures. Towards that, bulk estimates such as UHI Intensity are inadequate to address the problem of *intra-urban* spatial heterogeneity and often impede the analysis of urban temperatures at an intra-urban scale.

The primary cause of thermal variability is the heterogeneity of urban form itself. One of the most significant advancements towards a climatologically relevant LULC classification of the city is developed by Stewart and Oke (2012). The intra-urban classes are called Local Climate Zones (LCZ) and are formally defined as regions of uniform surface cover, structure, material, and human activity that span hundreds of

meters to several kilometers on the horizontal scale. Each LCZ has a characteristic thermal regime that is most apparent over dry surfaces, on calm, clear nights, and in areas of simple relief [3]. Examples of three cities, Indianapolis, Boston, and Mumbai, mapped as LCZs using the methodology described in ref. [16] are given in figure 1.1a. The random-forest based supervised classification scheme that uses a training dataset based on observable parameters such as building heights, spacing, and the amount of vegetative fraction, provided by the user. Schematic representations of LCZ classes are given in Appendix A. International collaborative efforts such as the World Urban Database Portal and Access Tools (WUDAPT) are implementing the standardization of the methodology across the urban climate scientific community [17].

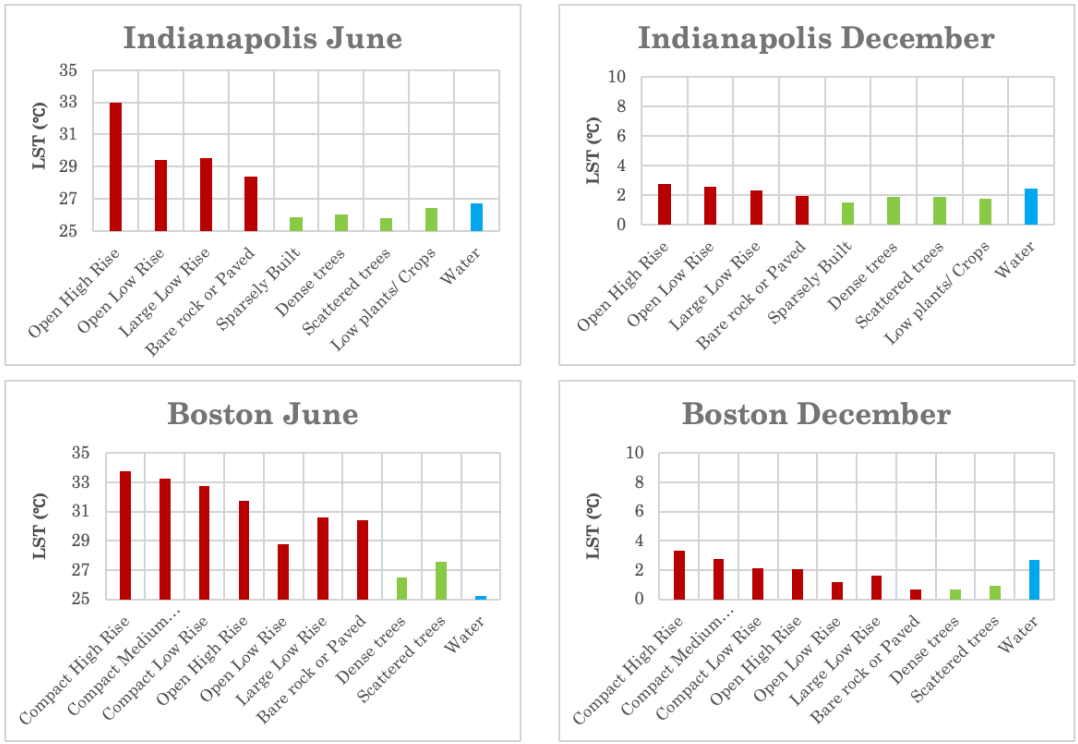

Figure 1.2. Barplot of mean LST temperatures for each LCZ of (a,b) Indianapolis and (c,d) Boston corresponding to an 8-day composite LST (from MODIS) in June and December respectively.

In an analysis of the correlation between LCZs and LSTs, I examine the case of Indianapolis and Boston for two distinct weeks in June and December, respectively, as a representative of summer and winter temperatures. A composite 8-day average LST product from MODIS (MOD11A2) was used for analysis (Figure 1.1). The mean LST value over each LCZ class is shown as a barplot in figure 1.2. Note that the thermal variability within the urban classes (shown in red) are as significant as the difference between urban and rural LCZs (up to 2°C in summer). These findings are also discussed in several other papers, such as refs. [3, 18, 19]. There is growing consensus in the urban climate community that while the terms "urban" and "rural" may be evocative of the landscape, they are vague as objects of scientific UHI analyses and the urban-rural divide has blurred into a gradual continuum of diverse urban forms and functions [3].

Beyond the heterogeneity across LCZ, there is an inherent variability within the same LCZ as well (Figure 1.3a-c). Under the assumption of a non-parametric distribution, pairwise Mann-Whitney's U test is conducted for the LST pdfs across all LCZs. The results indicate that there is no statistically significant difference across the temperatures for some pairs of LCZs (Figure 1.3d-f). Lastly, the pdf of temperatures within the LCZ class also depends on the spatial aggregation of the LCZ patches. As an example, the spatial organization of the LCZ 8, i.e., the Large Low Rise urban type (for instance, blocks of American supermarket and parking lots), is discussed. In figure 1.3g, the urban patches corresponding to LCZ 8 (in red) are larger and more aggregated in space. In contrast, LCZ8 patches for Boston (figure 1.3h) are dispersed throughout the city. Subsequently, the variance of LSTs within LCZ 8 is larger for the city of Boston, as compared with Indianapolis (Figure 1.3i). As a result, studying urban thermal differences based on a purely LULC methodology is inadequate.

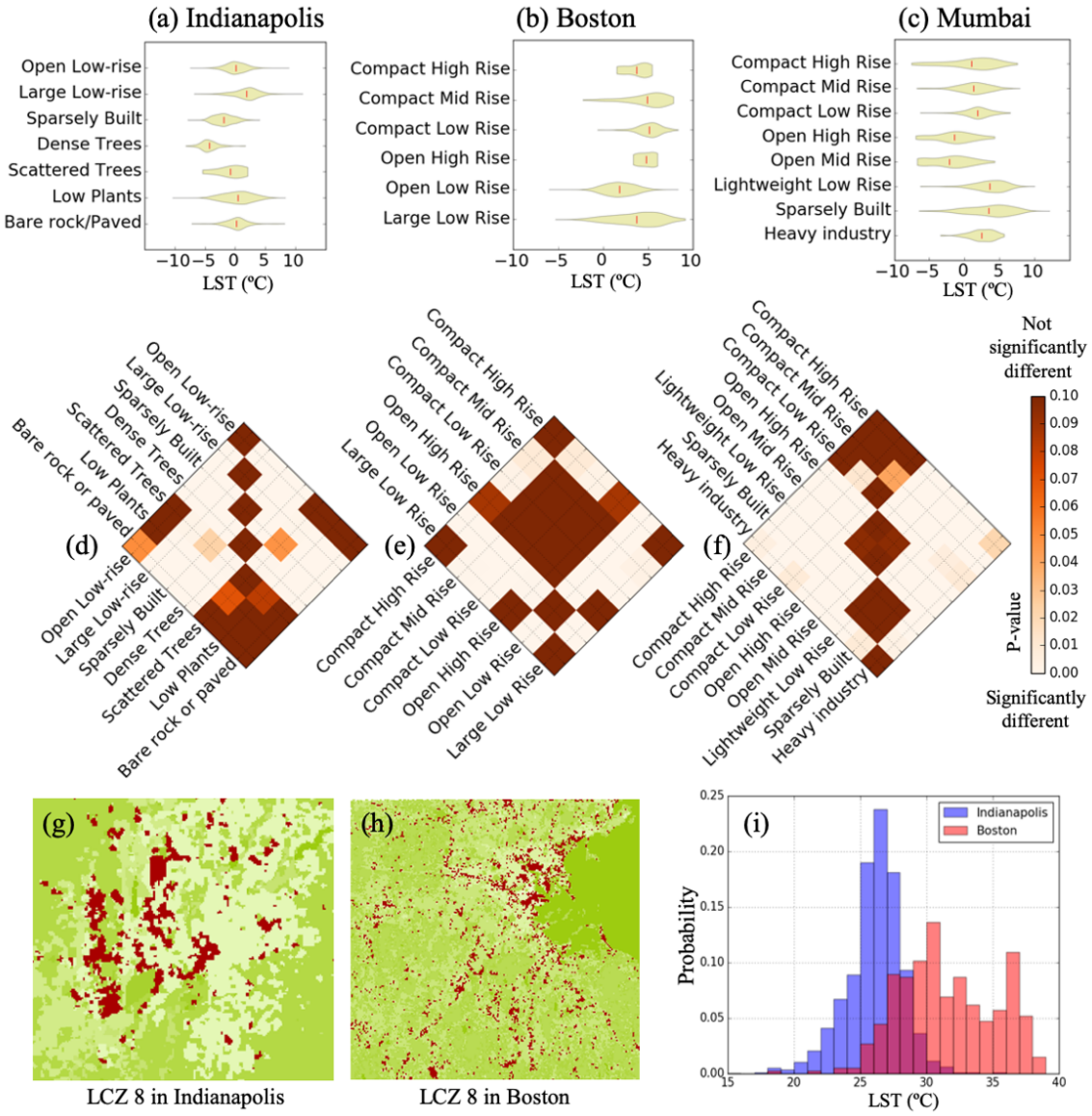

Figure 1.3. Probability distribution functions for LST within each LCZ is shown for (a) Indianapolis, (b) Boston, and (c) Mumbai. The LCZ classes present in each city are listed along the y-axis, and the variability in LSTs are displayed as a violin plot along the x-axis. The short vertical lines within the violin plots correspond to the mean LST. (d,e,f) P-value of Mann Whitney's U test to estimate statistical significance in the difference between LST populations is shown for each pair of LCZs for the three cities. In the bottom row, all regions corresponding to LCZ 8 for (d) Indianapolis, and (f) Boston, are highlighted in red. (e) The variability in temperatures corresponding to LCZ8 for the two (in blue and red respectively) are drawn for comparison.

2. COMPLEX CITIES AND THEIR THERMAL LANDSCAPES

"Clouds are not spheres, mountains are not cones, coastlines are not circles, and bark is not smooth, nor does lightning travel in a straight line."

– Benoit Mandelbrot, *Fractal geometry of nature*

I view *"extreme heat in cities"* as a Complexity problem at the nexus of two interacting complex systems - extreme weather and urbanization. Weather and climate are extremely dynamic complex systems that span a multitude of temporal and spatial scales. They range from turbulent wind gusts to seasonal fluctuations (weather), to macroscopic trends spanning decades (climate). Moreover, we are currently witnessing an upheaval of climate regimes wherein extreme weather events such as heatwaves are becoming more intense, frequent, and persistent. Alongside increasing temperatures, there is also the challenge of accelerated urbanization [20]. Cities are multi-scale systems consisting of *spatially heterogeneous* urban form, such as buildings and socio-technological networks such as roads, railways, power grids, etc. that grow and decay on a *timescale of decades* while many urban functions such as mobility, energy consumption, anthropogenic emissions, etc. that vary within the *timescale of hours*. One of the manifestations of the dynamic multi-scale interactions between these two systems is the UHI, which causes a further increase in energy consumption and heat-related casualties. In other words, *while extreme weather influences human behavior; collective human behavior impacts the weather itself.* As UHI is a manifestation of urban form and function itself, I build on the properties of fractal cities to characterize the spatio-temporal complexity of the thermal landscape.

2.1 Fractal form and function

The field of fractal geometry was developed by Benoit Mandelbrot in the mid 20^{th} century. Its applications to a wide variety of real-world problems were exemplified and popularized by his remarkable book, *Fractal Geometry of Nature* [21]. The irregular and complex geometrical shapes, such as coastlines of countries and perimeters of lakes that were earlier considered untenable, became widely studied and characterized using techniques developed by Mandelbrot.

Cities are some of the best examples of fractals. Urban form is defined as the physical characteristics that make up built-up areas, including the shape, size, density, and configuration of settlements. From the favelas of Mexico City or the neat urban blocks of Barcelona to haphazardly heterogeneous neighborhoods of Mumbai, the urban form is diverse. Yet, despite these differences, cities across the world show similar fundamental patterns. Most notably, in the past few decades, Batty and others have shown that the commonalities between urban spatial patterns are best characterized as fractals [22]. Various elements of the urban form, such as impervious area, road networks, sewage networks, etc. have been shown to have fractal properties [23–26]. Similarly, the metabolic functions of cities, such as population distribution, traffic flow, human mobility, and energy use, display self-similarity in the spatial patterns as well [27–29]. The spatial organization of physical assets, i.e., the urban form (e.g., impervious areas; buildings), in turn, governs the distribution of heat sources in a city. These distributed and fixed sources add excess heat and modify the cooling effect of heat sinks (e.g., vegetation and water bodies).

Based on these prior findings and the established correlation between urban surface temperatures and urban morphology [30–32], **I hypothesize that the SUHI should follow a fractal spatial structure as well.** While similar scaling laws and fractal metrics have been developed in atmospheric sciences [33], their application in SUHI studies remains limited [14, 34].

2.2 Percolation theory of fractal landscapes

Fractal geometry also has a long history of application in the field of **percolation theory**, a canonical branch of statistical physics that focuses on the connectivity of clusters in a system [35,36]. In particular, it is used to characterize the complex topographical surfaces (such as a DEM) as iso-lines (or contour lines). At any threshold, the continuously connected regions above the threshold are referred to as a cluster. In percolation theory, the coagulation of dispersed clusters into a giant contiguous component is referred to as percolation, and the largest cluster is identified as the *percolating cluster*. The threshold at which the single connected component appears is referred to as the *percolation threshold*. For statistically self-similar (or fractal) surfaces, the set of areas of clusters follows a probability distribution with a power-law tail at the percolation threshold [37,38]. This was first presented as an empirical rule by physicist and geographer Jaromir Korčák, who suggested a scaling law describing the size-distribution of various geographical objects, including lakes and archipelago of islands [39]. In summary, this law is expressed as the relative number of islands with an area equal to a is given by the power-law: $N(a) \propto a^{(-\beta)}$. Multiple studies have reported the occurrence of such scaling in natural topography such as islands [40], lakes [41], where the respective size distributions are well described by a power-law tail. For example, in hydrology, the power-law distribution of area exceedance for flow accumulation is a well-established signature of self-organization [42].

Another feature of fractal systems is the scaling of fluctuations as a function of the mean. This type of scaling relationship is called Taylor's law by ecologists after L.R. Taylor and his influential paper on natural populations [43]. In the ecological context, the law states that for any fixed species, the fluctuations in the size of a population (characterized by the standard deviation) can be approximately written as α: $fluctuations = k * mean^{\alpha}$ for a wide range of the average. This is since found several other applications in other complex systems such as traffic, stock market, precipitation, and networks [44,45].

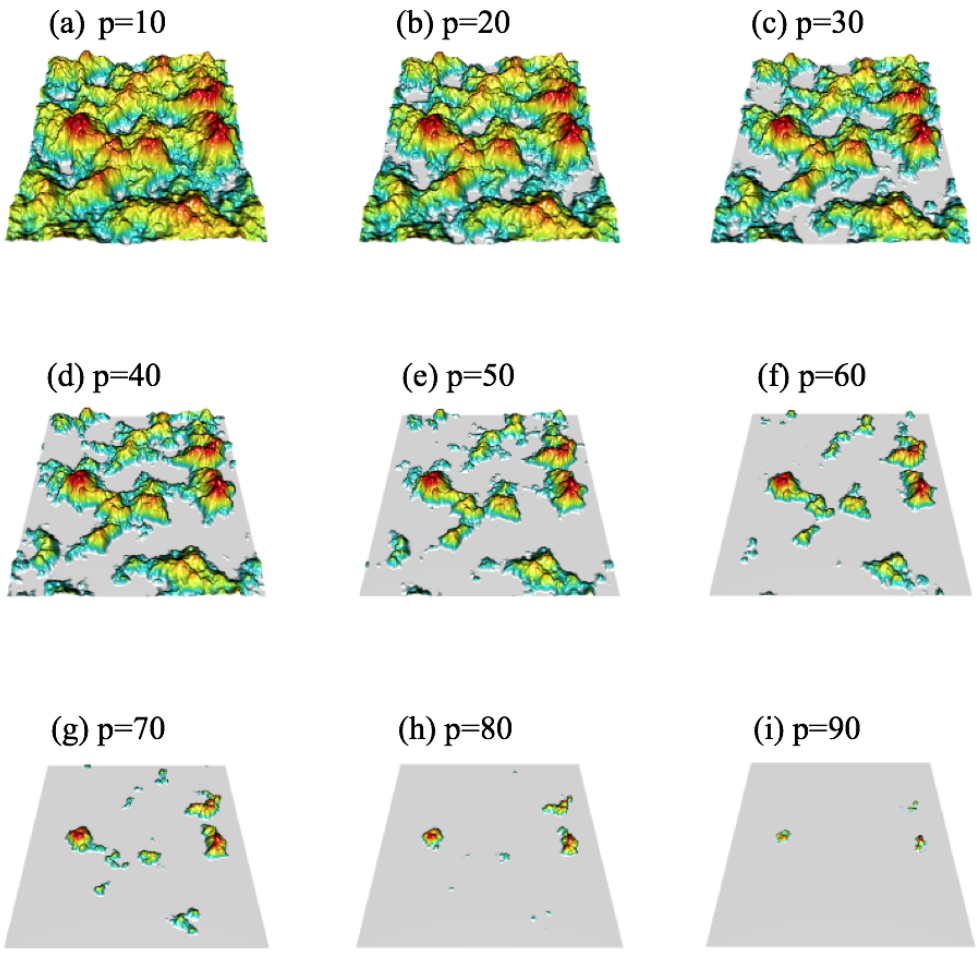

Figure 2.1. Illustrated above in an example of thresholding by percentile. The thermal maps are represented as 3-d elevation maps where height, as well as color, corresponds to a higher temperature. For each percentile of the thermal threshold, the areas above that are selected and connected pixels (by Moore neighborhood) are grouped into a cluster. Figures (a-i) show the clusters that emerge above nine incremental percentiles (shown as p, here).

2.3 Mathematical formulation of intra-urban heat islets

For UHIs, the most popular metric of quantifying the excess urban heat is the UHI Intensity, which is defined as the difference between the mean urban temperature and the mean background temperature of surrounding non-rural regions. However, the urban-rural classification has its limitations. "Rural" in this context is characterized by non-urban, sparsely populated regions surrounding the denser "urban" counterpart. However, as the peri-urban settlements increase and cities sprawl farther into the non-urban neighborhoods, the standardization of reference rural temperatures has become very difficult. Subsequently, the UHI Intensity varies significantly depending on the choice of a rural neighborhood. A solution to this problem is the use of percentile-based thermal thresholds to identify anomalously hot regions.

To characterize the complex spatial structure of the urban thermal, I conceptualize the thermal map as a Digital Elevation Model (DEM) where temperatures substitute for elevation (See figure 2.1). For a given LST map, I select regions with temperatures above specified percentile thresholds (T_{thr}) and group the connected regions together using a Moore neighborhood to define clusters, thereby identifying islets of higher heat for each incremental threshold [46]. In this way, the thermal threshold is analogous to the water level flooding a landscape so that only the islands above the water are considered for analysis [47]. Using this framework, we can capture the heat islets across several spatial scales at several thermal thresholds.

As T_{thr} is decreased, the total number of clusters increases as more regions with $T > T_{thr}$ are selected. However, at a certain threshold, the number of clusters start declining as they coalesce to form a giant connected component. This threshold is referred to as the **percolation threshold**. This is illustrated in figure 2.2 using the example of Boston, USA. Note that corresponding to the percolation threshold (marked in dark red), the total number of clusters reaches a maximum and starts declining. At the same threshold, the size of the largest cluster starts increasing as it continues to absorb smaller clusters. I refer to the set of clusters obtained at any

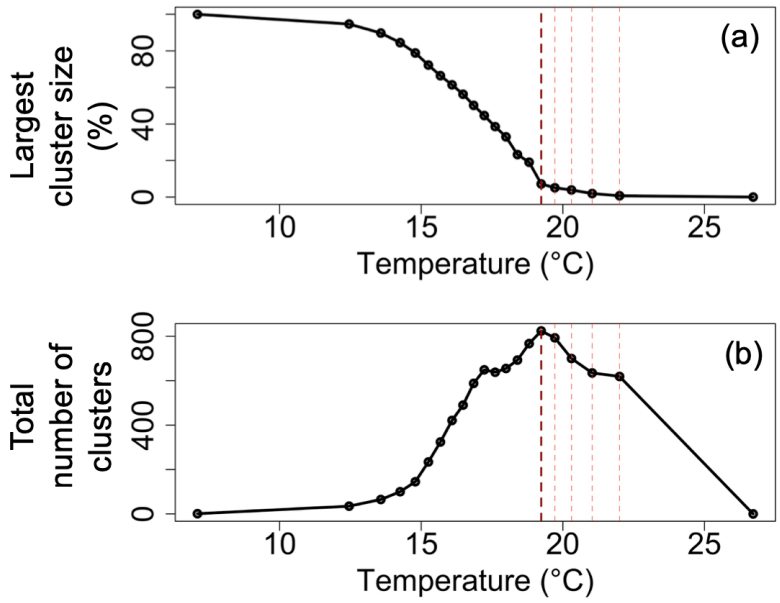

Figure 2.2. (a) Plot of largest cluster size as a function of the thermal threshold for the case of Boston city (b) Total number of clusters shown for each thermal threshold. The first dashed red line shows the percolation threshold (75^{th} percentile in this case) identified as the threshold where the total number of clusters is the maximum and below which the largest connected component emerges. Lighter red lines towards its right mark the subsequent percentiles of threshold which were considered for the analysis.

threshold as ***intra-urban heat islets***. As a result, the SUHI can be viewed as a collection of several *intra*-urban heat **islets** that emerge and interact to form the "mega heat island" that is notable at a regional scale. When the thermal threshold is equal to the rural background temperature, the resultant set of heat islets corresponds to the SUHI as per its conventional definition. In this way, I present a new viewpoint of the UHI as an *archipelago* of intra-urban heat islets. This opens up the opportunity to condense the spatial complexity of UHI into quantifiable heat islet characteristics. These properties are systematically explored using the key questions and hypotheses that are discussed next.

2.4 Key research questions

- *What is the islet's characteristic shape and geometric properties?* **Hypothesis:** Since, urban form and function is fractal in nature, the resulting heat islets will also have a fractal geometry.

- *How many and how big are the islets? What is their size distribution?* **Hypothesis:** Given the hypothesis stated in the previous question, like other fractal landscapes in the world, such as wetlands, lakes, and islands, it would have a power-law size distribution within the percolation range of thresholds and display exponential tempering at thresholds above.

- *What is their spatial structure? Does the spatial pattern play a role in heat mitigation?* **Hypothesis:** The spatial distribution urban form and function, such as sprawl or compactness, will play a role in heat mitigation and can, therefore, influence the spatial organization of heat islets.

- *What are their diurnal temporal dynamics?* **Hypothesis:** SUHI is known to be the strongest during the daytime. As a result, the heat islets as well should be the most numerous and largest during the daytime and dissipate during the night.

- *How do they interact with a heatwave?* **Hypothesis:** Heatwaves are persistent high-pressure systems that have been observed to both enhance as well as suppress the UHI Intensity. I hypothesize that this interaction would be governed by the urban form. A spatially aggregated system of heat islet might grow stronger, whereas, for a dis-aggregated city, the smaller islets might be dissipated easily, resulting in a smaller difference between urban and non-urban temperatures, hence lower intensities.

3. STATISTICAL CHARACTERIZATION OF HEAT ISLETS FOR GLOBAL CITIES

"Science begins with counting. To understand a phenomenon, we must first describe it; to describe it objectively, we must first measure it."

– Siddhartha Mukherjee, *The Emperor of all Maladies*

In this chapter, first, the methodology of selecting cities from across the world (in Section 3.1) and derivation of their LST from Landsat 8 (in Section 3.2) is discussed. Then, to describe the complexity of heat islets in a rigorous, reliable, and reproducible way, properties such as **shape, size, temperature, and spatial structure** of heat islets are quantified. Shape in this context refers to their collective irregularity that is quantified by the aggregated area-perimeter fractal dimension of the entire set of islets (section 3.3.1). Their spatial organization is quantified using a novel Lacunarity-based metric (section 3.3.3). Sizes are calculated as the set of areas of each islet, which are then modeled as a probabilistic distribution function (pdf) (section 3.3.2). Similarly, the set of islet intensities, defined as the difference between the mean LST for each islet and the thermal threshold, are also modeled as a pdf (section 3.3.4). These analyses serve to answer questions such as *"How many and how big are the islets? How much hotter than a given thermal threshold are they?"*. Lastly, discussions pertaining to the similarities and dissimilarities of islet properties across global cities are presented at the end of the chapter (section 3.4). Parts of this chapter are published in Physical Review E[1] and Scientific Reports[2].

[1]Shreevastava, A., Rao, P. S. C., & McGrath, G. S. (2019). Emergent self-similarity and scaling properties of fractal intra-urban heat islets for diverse global cities. Physical Review E, 100(3), 032142.

[2]Shreevastava, A., Bhalachandran, S., McGrath, G. S., Huber, M., & Rao, P. S. C. (2019). Paradoxical impact of sprawling intra-Urban Heat Islets: Reducing mean surface temperatures while enhancing local extremes. Scientific Reports, 9(1), 1-10.

3.1 Set of 78 globally diverse cities

Initially a set of 100 cities that are representative of diverse climate types [48] as well as cultural backgrounds were selected, including but not limited to the C-40 (`http://www.c40.org/cities`). Since the focus of this thesis is intra-urban heat, only the cities that exhibited elevated temperatures within the urban boundaries were selected. Cities which showed inversion of the heat island effect [49] due to hotter background climates such as Phoenix, Cairo, or Jaipur or cities with a significant coastal influence such as San Francisco, Mumbai, or Singapore were removed from the set. Lastly, cities containing significant topographic relief dominating the LST patterns such as Medellin, Ulaanbaatar, or Lima were removed as well. The remaining cities comprise of a suite of case studies containing 78 cities. These range from small cities such as Bern and Tbilisi (population 200 k) to the largest metropolitan regions

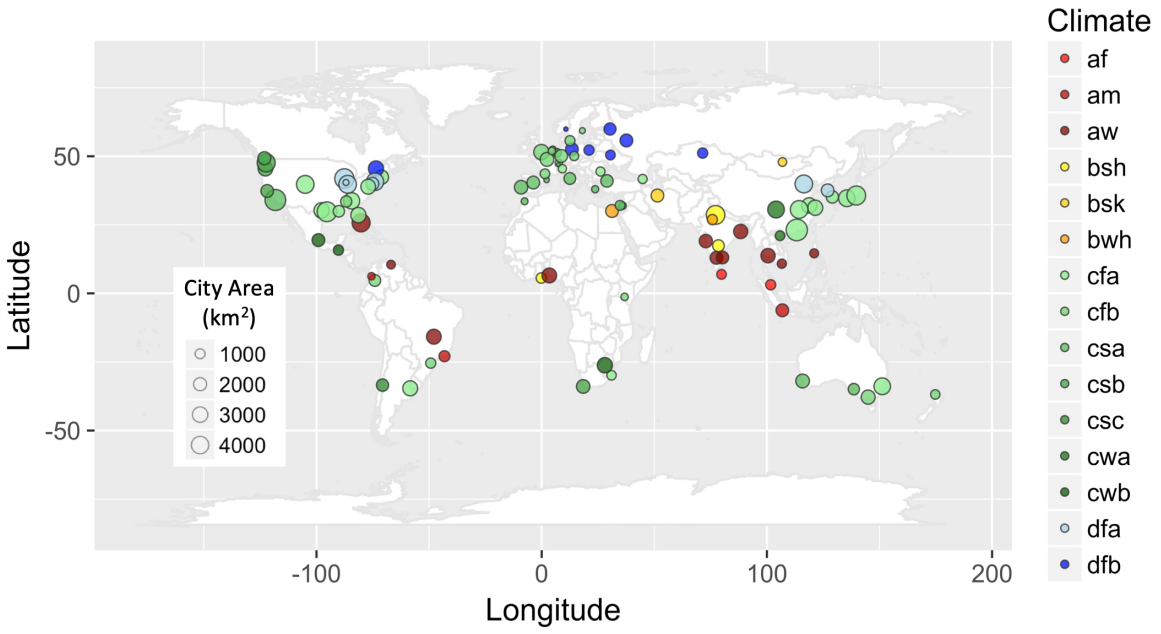

Figure 3.1. World map showing the locations of 78 cities considered in this study. The marker size is representative of the city size, and the colour represents their Koppen-Geiger climate classification [48].

like Tokyo and Osaka with a net population of $\sim$ 30 M. It includes densely packed cities, such as Seoul and Beijing, as well as agglomerated cities such as Mexico City and Jakarta; spatially heterogeneous cities like Mumbai and Shanghai, to structured and grid-like ones such as Los Angeles and Houston. It should be noted that the selected list is not exhaustive in any way but a representative subset of diverse global cities. Complete list of cities studied is attached as Table S1 of Appendix B.

For each of the selected cities, the urban area was estimated using Land Cover Type dataset (MCD12Q1) derived from MODIS (Figs 3.2a, and 3.2e). The exact definition of urban boundaries and city area plays a significant role in urban scaling laws where different urban extents can produce different statistical exponents [50], therefore, a buffer of 5 km in the rural regions was taken to account for the peri-urban settlements. However, as the heat islets occur well within the city boundaries, the estimated exponents were found to be independent of the buffer width. Lastly, in case of coastal cities, the Large Scale International Boundary (LSIB) dataset provided by United States Office of the Geographer was used to crop out the oceans and delineate coastal boundaries.

3.2 Data: Land Surface Temperatures from Landsat 8

The primary source of LST in this thesis is Landsat 8. Low Earth Orbiting imagers such as Landsat 8 have a high spatial resolution of 100 m but an infrequent repeat of every 16 days. Since, in this section I am only focusing on a spatial characterization, one Landsat image per city was selected. An initial screening was implemented using Google Earth Engine [51] to select cloud-free summertime days for each city with an incident solar angle of at least 60 degrees. LST was derived by a Single Channel Algorithm as detailed in [52] using data from Landsat 8 (Bands 4, 5, 10, and 11) daytime images (Figs 3.2b, and 3.2f). While the native resolution of Thermal Infrared sensor (bands 10 and 11) is 100 m, they are sampled to match the other bands at 30 m in the Landsat composite product. In order to avoid any error that might

have been introduced due to the downscaling of thermal band datasets, we opted to aggregate the resolution to 90m (which is closer to the native TIRS resolution). Given the abundance of surface types in the urban environment, the net estimated LST is a resultant of several reflective materials within the pixel area. Therefore, anomalous LSTs lying outside the 99.9 percentile were smoothed out by assigning them the average value of their neighborhood pixels. Figure 3.2 serves to visualize the geospatial format of data collected using the example of Boston, USA, and Kolkata, India. See Appendix C for algorithm and Table S1 further information on Landsat scenes used.

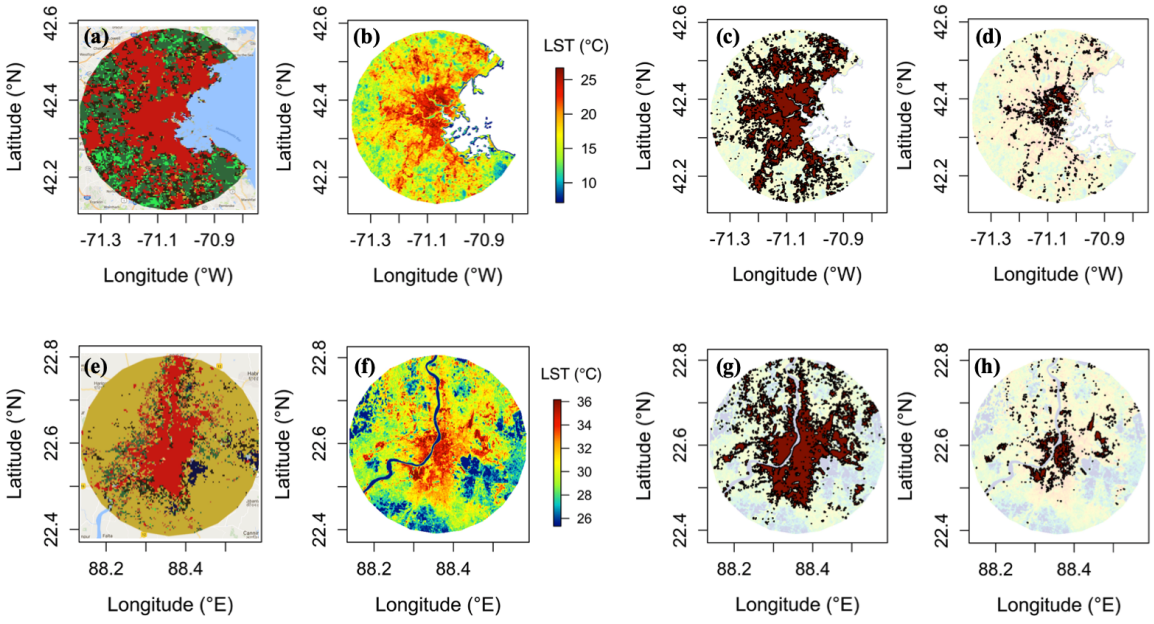

Figure 3.2. Maps for Boston (top) and Kolkata (bottom) are shown here as examples. (a, e) Land use map derived from MODIS - Land Cover Type dataset for the year 2016. (b, f) Land Surface Temperature (in °C) map derived from Landsat 8. (c, g) Heat islets above the percolation temperature (19°C for Boston and 32°C for Kolkata) obtained using Moore neighborhood clustering algorithm are indicated as red. (d,h) Extreme high heat islets obtained at the 95th percentile temperature of each city.

3.3 Properties

3.3.1 Self-similarity and Fractal Dimension

As a primary test of fractality, the aggregated Area-Perimeter fractal dimension (D) [40] is chosen. Total area and perimeter of the islet set is estimated at multiple values of thermal threshold, T_{thr} (50^{th}, 60^{th}, $\cdots$, 90^{th} percentiles), and D is calculated using the following equation:

$$\Sigma P = k \cdot \Sigma A^{\frac{D}{2}} \tag{3.1}$$

where, $k = 2 * \sqrt{\pi} = 3.545$, that is determined for the limiting case of a circle, and the summation of perimeters (P) and areas (A) goes over the set of islets. Note that this refers to the fractal dimension of the ensemble iso-thermal contour lines [22]. In the limiting case of a circle, $P \propto \sqrt{A}$ and $D = 1$. For more irregular and convoluted shapes, the perimeter becomes increasingly plane-filling or elongated, and the area tends to zero, resulting in linear shapes where $P = A$ and $D = 2$ (solid bounding lines in figures 3.3a and 3.3b). For statistically self-similar surfaces, not only is D a fractional value between 1 and 2, but it is also the same for all thresholds used for clustering [38]. In figure 3.2, I use the example of Boston and Kolkata to illustrate the collection of islets that appear at two different thermal thresholds, one corresponding to the percolation threshold, and another corresponding to the 95^{th} percentile. At higher temperature thresholds we can delineate areas within cities that experience extreme temperatures.

For each city, D is found to be consistent for all values of T_{thr} as shown by the same $log(Area) : log(Perimeter)$ ratio. Figure 3.3a shows the area perimeter scatter plot for two example cities, Bern and Atlanta, at the five thermal thresholds. Note that for each city, the Area-perimeter ratio, i.e. D remains constant. This is a novel and key finding, demonstrating the statistical self-similarity of SUHIs and empirically establishing fractal geometry of urban thermal landscape. Figure 3.3b serves to demonstrate the same for all cities under consideration. Note that as cities

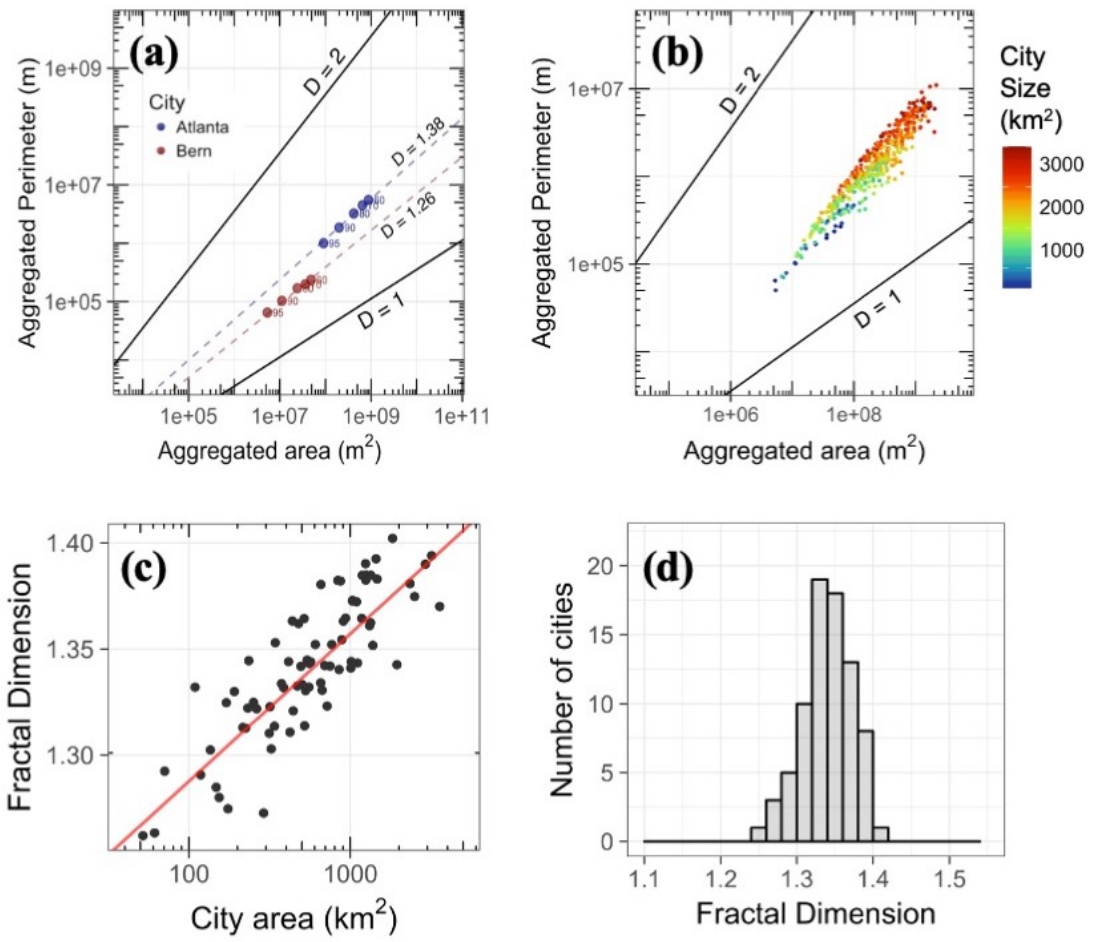

Figure 3.3. (a) Aggregated perimeters versus aggregated areas at 60, 70, 80, and 90 percentiles thresholds are shown here for two cities, Bern (in red) and Atlanta (in blue), demonstrating the same ratio of log(Area) and log(Perimeter) and hence the same Fractal Dimension (D) of iso-thermal contour lines as indicated by the grey, dashed lines show examples of two cities with $D = 1.38$ for Atlanta and $D = 1.26$ for Bern. D of the perimeter of a circle ($D = 1$) and a space-filling plane ($D = 2$) are plotted to show the physical bounds for D. (b) The same plot for all cities shown with a single colour attributed to each city that corresponds to its area. (c) D as a function of the city area. This plot serves to illustrate that D increases with city area as per $D = 0.0695\, logA_{city} + 1.15$ ($R^2 = 0.7$). (d) Histogram of D for all cities at their respective percolation thresholds with mean $= 1.33 \pm 0.033$ (std. dev.).

grow in size, as indicated by the colorbar from blue to red, the corresponding sets of areas and perimeters increase. This results in an upward shift in the plot and an increase of D. The same can be observed in figure 3.3a, where Atlanta has larger values of both area and perimeter and a resultant slope corresponding to $D = 1.38$ compared to $D = 1.26$ for Bern.

The scaling of D with city size is demonstrated more clearly as a scatter plot between D and city area, where D is weakly correlated to the city size following the relation $D = 0.0695 \cdot log(A_{city}) + 1.15\,(R^2 = 0.7)$ (Figure 3.3c). The tendency for D to

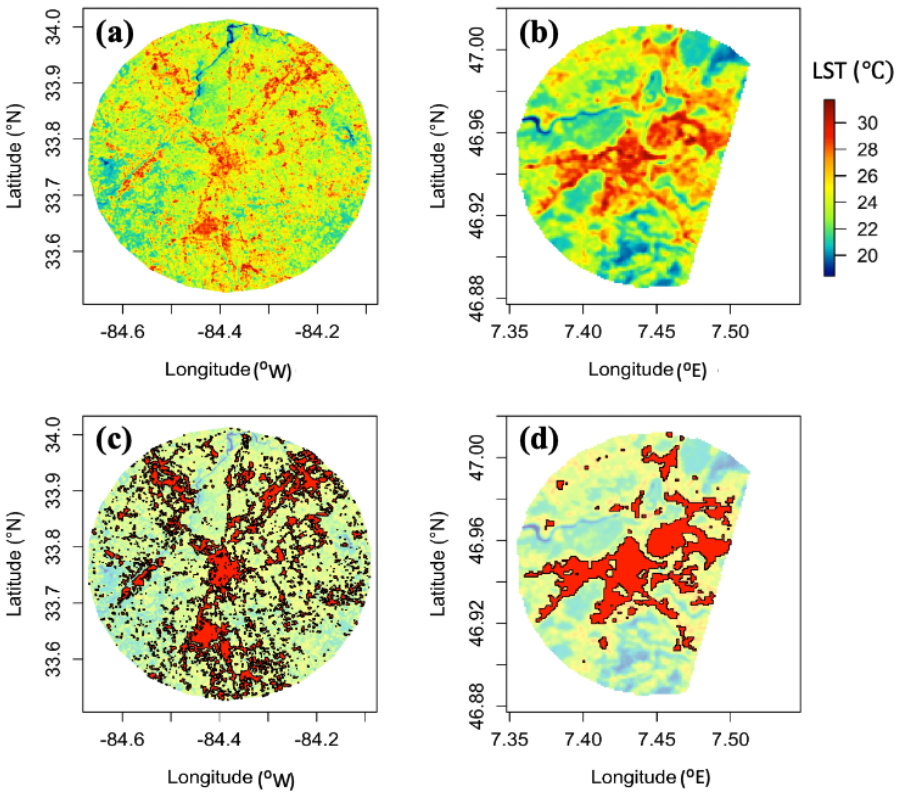

Figure 3.4. (a,b) LST maps of Atlanta and Bern, respectively. (c,d) Heat islets obtained at the percolation temperature for each city are overlaid (in red) on top of the LST maps. The islet perimeter is shown in black. Note that the maps are not drawn to scale. The diameter of region of interest for Atlanta is 54 km, whereas the same for Bern is 14 km.

be smaller for small cities is reflective the evolving urban morphology of cities as they grow. Smaller cities are often mono-centric (more circle-like) with fewer heat islets, as a result, D tends toward a value of 1. While megalopolises, on the other hand, formed from agglomeration of multiple peri-urban settlements are expected to have higher number of heat islets scattered throughout the city, thereby, increasing the net perimeter of heat islets, and thereby D. Maps of LST and heat islets (obtained at their respective percolation thresholds) for Atlanta and Bern are shown in figure 3.4 to illustrate this difference. Moreover, in larger cities, the islets are more abundant, as can be seen in the total number of islets for each city that scales linearly as $N = 0.038 * A_{city} + 40$ ($R^2 = 0.8$) (See figure 3.5). This indicates that the limitation of resolution of data in case of Bern is another contributing factor, where the smaller scale irregularities are not captured.

The histogram of D values (Figures 3.3d) indicates a normal distribution with a mean $D = 1.33$ and standard deviation of 0.033. This is an extremely narrow spread about the mean suggesting a strikingly similar D for all cities despite their diversity. Please refer to Table S2 in Appendix B for a complete list of D values. Lastly, to

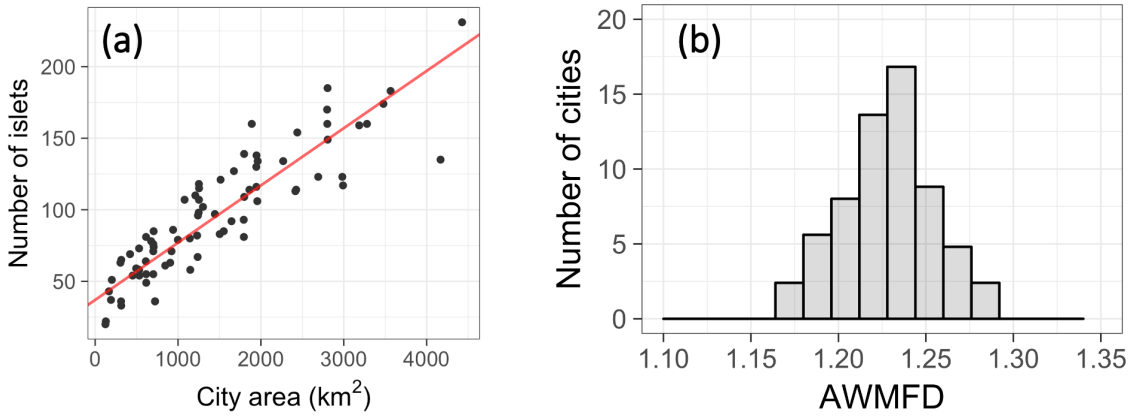

Figure 3.5. (a) Scatter plot showing the correlation between number of islets and city size that scales linearly as indicated by the red line. (b) Histogram of Area Weighted Mean Fractal Dimension (AWMFD) for all cities with mean $= 1.22 \pm 0.025$.

examine the average shape of a single islet within a city, area-weighted mean fractal dimension (AWMFD) can also be a useful alternative [14]. The AWMFD for heat islet sets were found to be normally distributed as well with a mean AWMFD = 1.227 (s.d. = 0.025; See figure 3.5b).

As LST and urban LULC are strongly coupled, these findings are compared with the reported fractal dimension of urban impervious area. In a study by Makse et. al., $1.2 < D < 1.4$ with a mean value of 1.33 was reported [24]. Another study found $D = 1.22 \pm 0.08$ for 68 Chinese cities [23]. Therefore, the fractal dimensions of heat islets as well are in agreement with that of urban impervious area.

3.3.2 Islet Size distribution

I now examine the variability in heat islets sizes. For fractal landscapes, clusters are statistically self-similar at the percolation threshold over certain ranges of sizes, with the cluster areas following a power law probability distribution [38]. This is the same as the relative number of islands with an area equal to a is given by the power-law: $N(a) \propto a^{-\beta}$ as discussed in section 2.1. As an exceedance probability distribution function, the size distribution can be written as the following:

$$P(A \geq a) \propto a^{1-\beta}, \quad \forall a \geq a_{min} \tag{3.2}$$

where, for a given area a, the probability of an islet having an area A larger than a is represented by P, the scaling exponent is represented by β, and the minimum area at or above which the power law is valid is represented as a_{min}. This is hypothesized to be valid for the set of heat islets sizes if they are fractal in nature. Above the percolation threshold, as described in section 2.3, the size distribution deviates from the power-law resulting in some form of tempering, often modeled as an exponential tempering (Figure 3.8a).

A preliminary indicator of a heavy tailed distribution (such as a power law) can be found by the "fluctuation scaling analysis" of islet sizes. Here, the relationship between the fluctuations in islet areas (characterized as the standard deviation) and

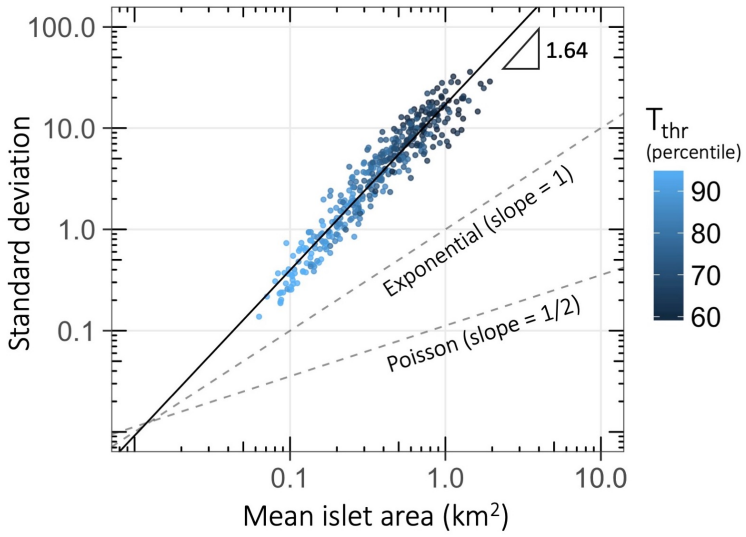

Figure 3.6. Scatter plot showing the correlation between mean islet area and its standard deviation. The solid line represents a slope of 1.64, referred to as the fluctuation scaling exponent α. Two additional dashed lines corresponding to exponential ($\alpha = 1$) and poisson ($\alpha = 1/2$) distribution are drawn.

the mean islet area for each city at each thermal threshold are evaluated. In agreement with the Taylor's law, the fluctuations are found to scale with the mean islet area as per the equation $s.d. \propto mean^{1.64}$ for all cities. Figure 3.6 serves to illustrate this where each point represents the std. dev. and mean for one set of heat islets obtained at a single threshold for a single city. As T_{thr} decreases, the mean area as well as std. dev. is observed to increase, while maintaining the scaling relationship as indicated by the slope of 1.64. Most complex systems report the scaling exponent, α, to fall within 1/2 to 1 [44] corresponding to a Poisson or Exponential distribution respectively (indicated as dashed lines in figure 3.6). A much higher scaling exponent in this case indicates a stronger spatial correlation and a heavier tailed distribution.

First, in order to test the hypothesis, the percolation threshold is identified for each city using the method described in section 2.2. For some cities, a sharp percolation transition was observed which corresponded to the maximum number of heat islets

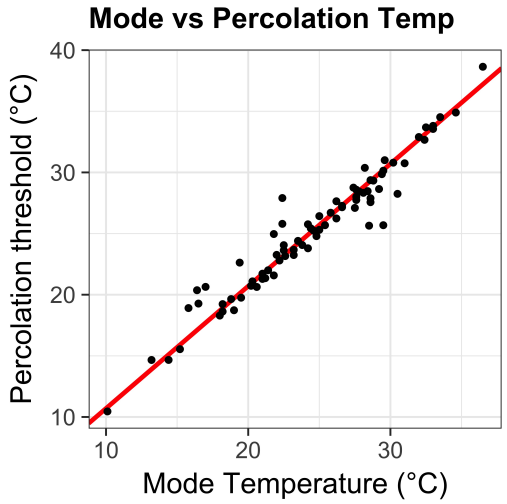

Figure 3.7. Scatter plot showing the correlation between mode temperature and the percolation threshold ($R^2 = 0.93$)

as well. The temperature corresponding to percolation threshold, in such cases, was found to be the same as statistical mode of the temperature distribution i.e. the most frequently encountered temperature in the city (figure 3.7). However, for the other cities, a more gradual change in largest islet size was observed which made the precise identification of percolation threshold difficult. For those cases as well, thresholds corresponding to the mode temperature (which also correspond to the threshold at which maximum number of islets are obtained) is chosen as the percolation threshold in this section. A detailed discussion pertaining to the two classes is presented in the next subsection.

In agreement with the hypothesis, for the heat islets across all cities, The area-exceedance probability distribution was found to follow a power-law tail at the percolation threshold which then deviates at higher thermal thresholds (example of Guangzhou shown in Figure 3.8a). This is consistent throughout all the cities with the scaling exponent normally distributed with mean $\beta = 1.88$ and s.d. $= 0.12$ (Figures 3.8b and 3.8c). Here, I have used a conservative approach to test for and fit the power-law distributions using a combination of maximum-likelihood fitting

methods with goodness-of-fit tests based on the Kolmogorov-Smirnov (KS) statistic and likelihood ratios [53]. Alternative distributions, such as log-normal, exponential and Weibull, were tested as potential candidates; however, they were all rejected (at $p > 0.1$), while the same tests suggested that the distributions could not be rejected as having power-law tails. See Appendix D for detailed methodology on probabilistic distribution fitting and Table S2 of Appendix B for results.

The power-law tails are curtailed on the higher end by limits of the study domain i.e. the total city size, in this case, [54], and on the lower end, by spatial resolution. Numerous smaller heat clusters are either not captured or are rounded off to integer multiples of the lowest available resolution. Interestingly, in this case, the lower bound (a_{min} at which the power-law tail starts) is ~ 0.25 km^2, which corresponds to the size of a couple of urban blocks. This suggests that below this, the heat islets may indeed scale differently as the individual building level features become evident. A relationship between D and β can be derived for Gaussian surfaces as $\beta - 1 = D/2$ [38]. However, this was not found to be true for heat islets indicating a departure from random Gaussian topography.

The power-law size distribution is another key finding that further supports the fractal structure. The area scaling exponent, β, varies between 1.6 and 2.2 for small cities ($A_{city} < 1000$ km^2), but for the larger cities it converges to the mean (see Figure 3.8d). One explanation for this is statistical, wherein for small cities, fewer islets obtained at 90 m resolution results in higher statistical fluctuations about the mean. As the number of islets increases with city size, larger sample sets are obtained, which results in a convergence of the scaling exponent towards the mean. However, from an urban growth perspective, this behavior is consistent with several other complex systems that operate within cities [55, 56]. For smaller cities, the variability due to factors unrelated to city size, such as diversity of urban form, results in more detectable fluctuations. As cities grow in size, the spatial patterns converge due to self-organization [57].

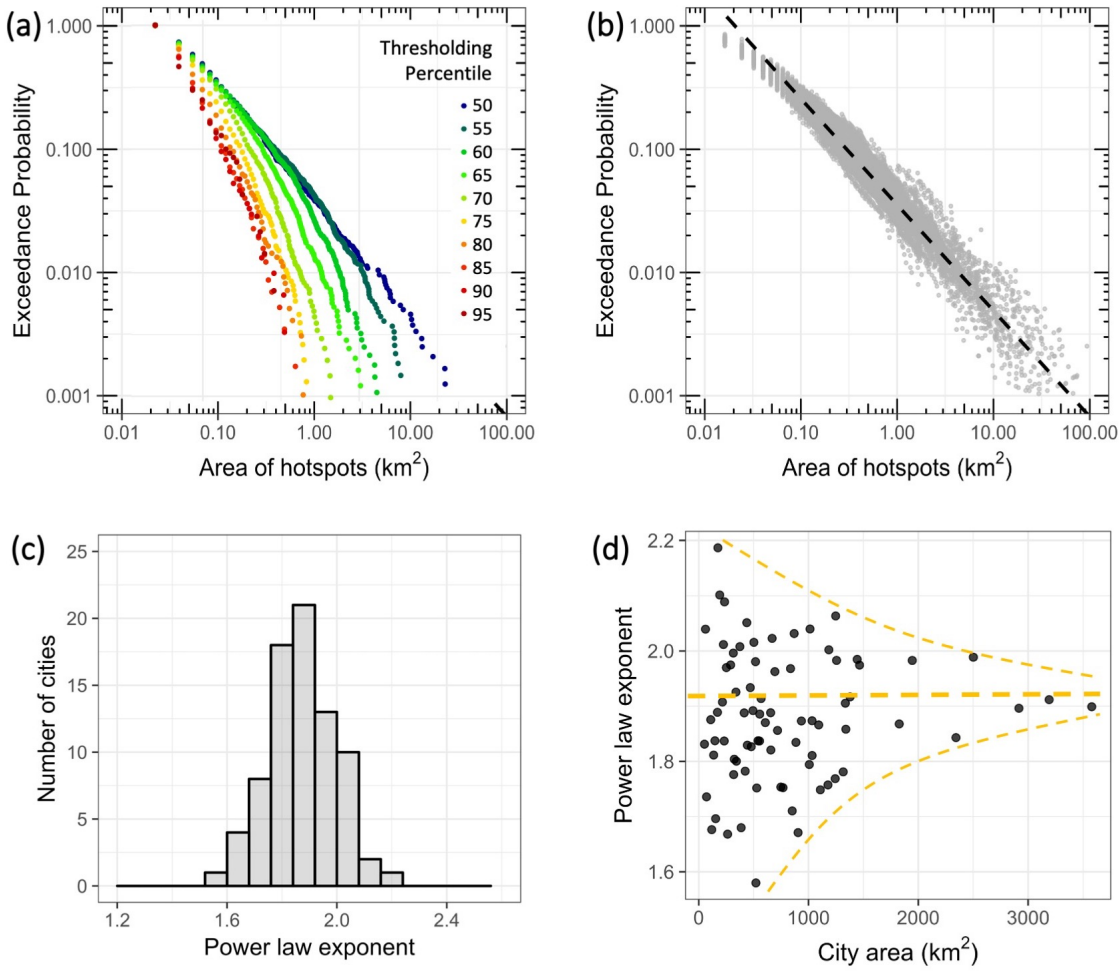

Figure 3.8. (a) Area Exceedance Probability Distributions for the city of Guangzhou (as an example) is shown at multiple T_{thr}. As T_{thr} increases (indicated in color from blue to red), the size distribution deviates gradually from the power law obtained at the percolation threshold (corresponding to 50^{th} percentile in this case). (b) Area Exceedance Probability Distributions for all cities at their respective percolation thresholds are shown here in grey. Overlaid as a dashed black line is the line demonstrating the mean scaling exponent, $\beta = 1.88$. (c) A histogram of β of all cities. (d) Scatter plot of β and city area for each city. Yellow dashed lines serve to highlight this convergence of β to mean with an increase in the city area.

Comparing with the literature of size distribution for fractal surfaces, I find that for the case uncorrelated percolation, β is estimated to be 187/91 ($\sim$ 2.05) [36, 37]. Moreover, empirical distributions of land classified as urban and cities modeled with correlated percolation as well have found similar size distributions with $\beta \sim 2$ [24, 58, 59]. A slightly smaller exponent of 1.88, in this case, indicates a greater probability of occurrence of heat islets than what would be expected from impervious area alone. Lastly, fractal landscapes are expected to yield the same scaling exponents irrespective of the resolution. To test their sensitivity to input resolution, LST maps were aggregated at a range of resolutions from 90 m to 720 m. Scaling exponents were found to be the same, adding further support to the self-similar topography of SUHI.

Percolation transition and tempering of power law

While the power law size distribution is consistent at the percolation temperature for all cities, the difference across cities become apparent in how the exceedance probability distributions change as the threshold increases. In case of some cities, such as Lagos and Jakarta (Figure 3.9a,b), the power law size distribution is maintained even at higher thresholds (Figure 3.9e). For others, such as Chicago and Guangzhou (Figure 3.9c,d), the heat islet size distributions deviate significantly from the power law in the form of an exponential tempering (Figure 3.9f), such that their distributions more closely follow:

$$P(A \geq a) \propto a^{1-\beta} \cdot e^{-c \cdot a}, \quad \forall\, a \geq a_{min} \tag{3.3}$$

where c represents the exponential tempering coefficient for each thermal threshold (See Supplementary Table 3 for the complete set of coeffecients).

This behavior is explained by looking closely at the percolation threshold discussed earlier [36, 37]. In fractal landscapes, the power law size distribution of clusters holds true only at the percolation threshold, i.e., until which the percolating cluster retains

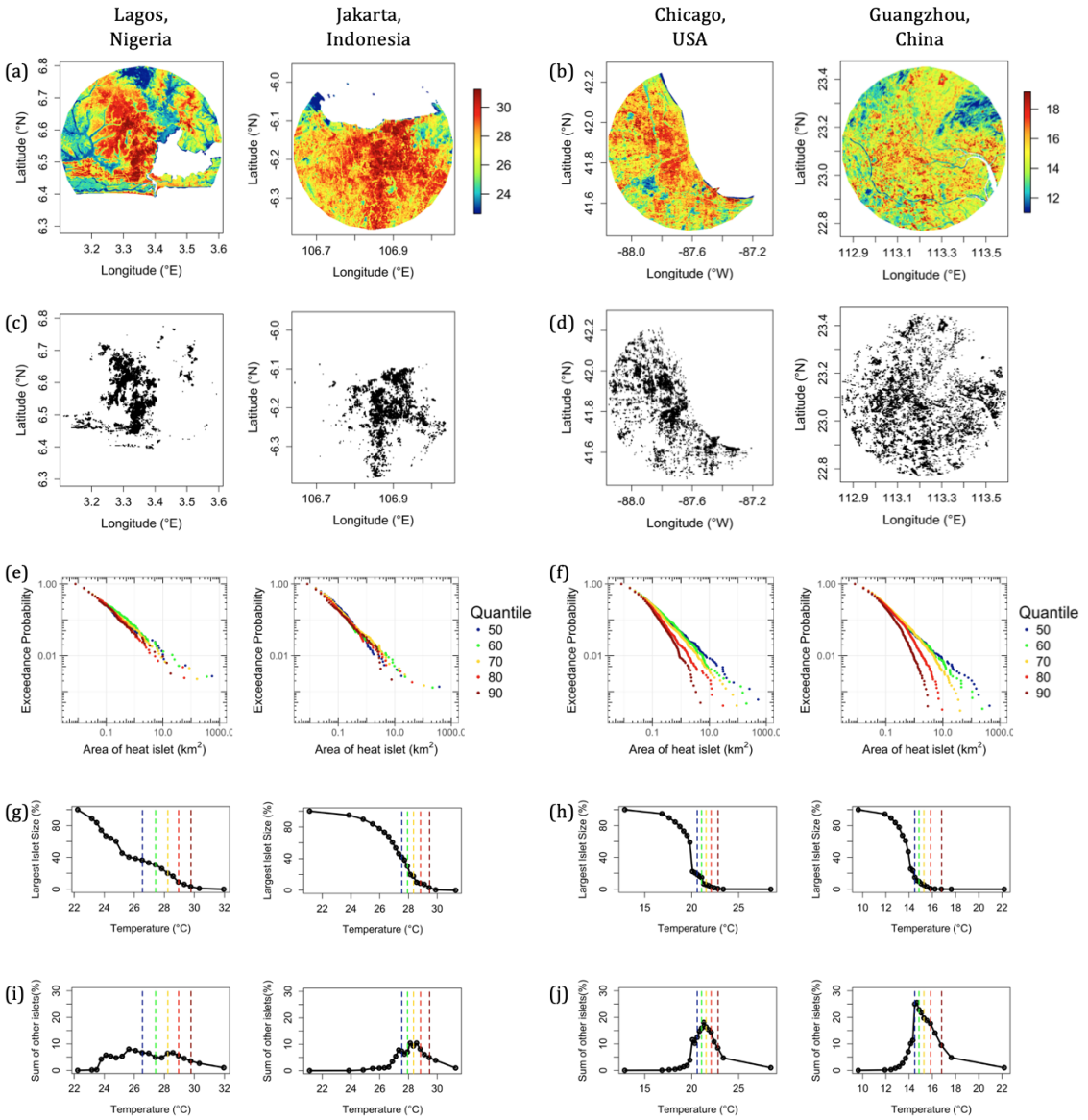

Figure 3.9. Two groups of cities emerge based on the size distributions of heat islets at incremental thermal thresholds. Two representative cities for each group - Jakarta, Indonesia, and Lagos, Nigeria; and Chicago, USA, and Guangzhou, China - are shown for each. (a,b) Land Surface Temperature map (in °C), (c,d) Heat islets that emerge at the 90$^{\text{th}}$ percentile thermal threshold. (e,f) Exceedance probability plots for heat islets at several thermal thresholds. Note the leftward shift in size distribution as the thresholds increase, especially the exponential tempering evident in second set of cities. (g,h) Largest islet size, and (i,j) sum of remaining islets (as a % of total city area), as a function of thermal threshold. The vertical dashed colored lines mark the temperatures corresponding to the percentiles used in (e,f).

its identity. In some cases (such as Jakarta and Lagos), this transition is not sharp enough to be defined by a single threshold. As a solution to that, the range of thresholds over which the transition takes place are identified and referred to as *Percolation Transition Range*. This is done by identifying the inflection points in the rate of change of the largest cluster size as a function of thermal threshold as illustrated in figure 3.10. The range is then normalized using the minimum and maximum temperatures for each city such that the range is restricted to 0 and 1. I refer to this new term as the *Normalized Percolation Range (NPR)*.

In the case of cities like Jakarta and Lagos, as the temperature threshold is increased, the largest connected islet decreases in size gradually, and the resulting NPR is large (Figure 3.9g). Conversely, in the case of cities that show exponential tempering, such as Chicago and Guangzhou, there is a much sharper decrease in the size

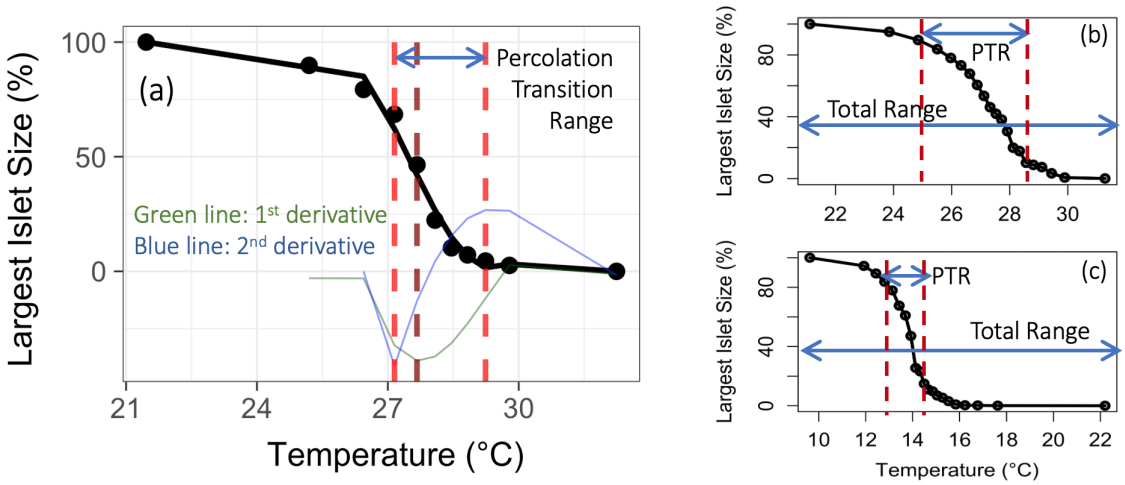

Figure 3.10. This figures serves to diagrammatically illustrate the Normalized Percolation Range (NPR). (a) Largest cluster size (A_L) as a function of temperature (T) was plotted. d^2A_L/dT^2 (shown in blue) at each thermal threshold was computed to find the inflection points. The range where rapid decrease in the largest cluster size takes place is referred to as the Percolation Transition Range (PTR). PTR is then divided by the total range to obtain the Normalized Percolation Range (NPR) for each city. (b,c) The same is illustrated for Jakarta and Guangzhou, respectively.

of the percolating cluster (Figure 3.9h) resulting in a narrow NPR (Figure 3.9i,j). As the 90^{th} percentile thresholds in these cases fall outside the NPR Figure 3.9j), exponential tempering is observed. In such cases, from the perspective of the size distribution of heat islets, fewer and smaller heat islets are captured as the thermal threshold is increased. Therefore, an exponential tempering can be interpreted as a reduced probability of encountering large heat islets of higher temperatures.

3.3.3 Spatial organization (Lacunarity)

Fractal surfaces with the same aggregated iso-line fractal dimensions can look very different depending on how the islets are located in space with respect to each other. Popular metrics such as root mean square distances work well for Gaussian systems, but for fractal landscapes, a metric of spacing called *lacunarity* is better-suited [60].

Lacunarity (represented as Λ), a word derived from the latin word "lacuna" which means holes or gaps, is a scale-dependent measure of the *gaps* between heat islets [21]. The 'gliding box counting' algorithm [61] was adopted for calculating Λ, which is described here. First, using the thermal thresholding technique (section 2.3), the LST maps were converted to a binary map of heat islets where each pixel with $T > T_{thr}$ is assigned the value 1, and others are assigned 0. Then, square boxes of increasing size ($1 < r < A_{city}$) are placed on a corner of the binary map and within each box size, the number of occupied pixels (value=1 corresponding to the islets) are measured. The number of occupied sites is referred to as the box mass. The box was then moved one column to the right, and the box mass was again counted. This process was repeated over all rows and columns, producing a frequency distribution of the box masses. The number of boxes of size r containing S occupied sites were designated by n(S,r) and the total number of boxes of size r by N(r). This frequency distribution was converted into a probability distribution: $Q(S, r) = \frac{n(S,r)}{N(r)}$. Lacunarity is calculated as per the following equation for each box size, r.

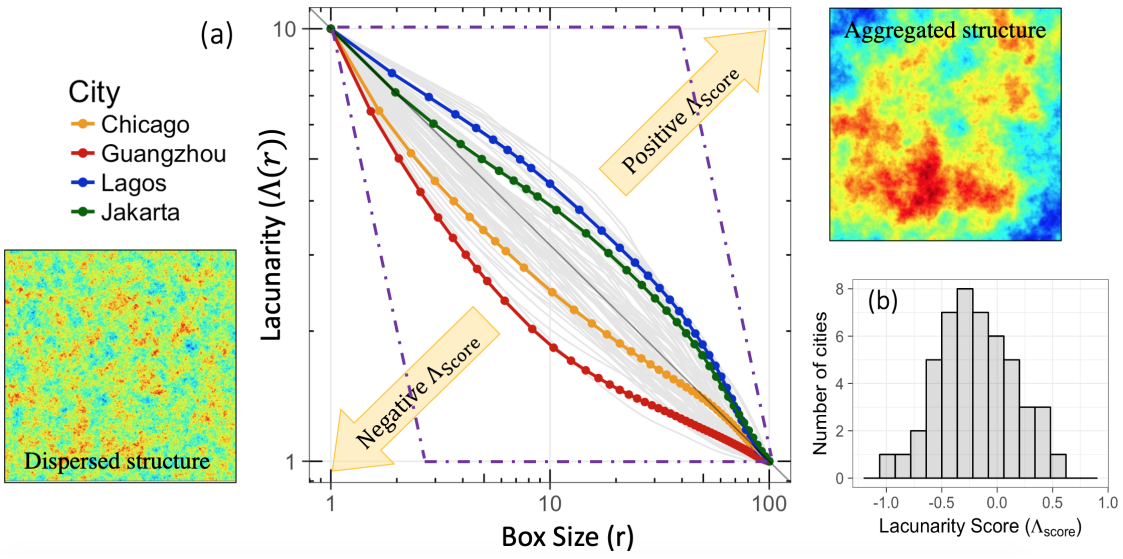

Figure 3.11. (a) Lacunarity curves of all cities (in grey) and the four archetype cities (in colour) shown on a $log(\Lambda)$ vs $log(r)$ plot. The cities with a concave downwards shape in the upper side of the diagonal indicate larger and more aggregated gaps, whereas cities underneath the curve indicate a more uniform dispersed pattern of islets and smaller gaps. (b) Histogram of Lacunarity scores (Λ_{score}) of all cities (mean = 0.04, s.d. = 0.38).

$$\Lambda(r) = \frac{Variance[Q(S,r)]}{Mean[Q(S,r)]^2} + 1 \tag{3.4}$$

While the absolute values of Λ offer little insight, the utility of lacunarity analysis is in examining the rate of change of Λ as a function of r. Therefore, as a final step, a graph of $\Lambda(r)$ vs r on a log-log scale is plotted for analysis. The presence of spacing corresponding to a length scale, r is indicated in the slope of Lacunarity curves as shown in figure 3.11. The two extremes of lacunarity curvature can be best conceptualized as a chessboard-type homogeneously dispersed structure of small-scale spacings (shown by a dashed line on the lower edge of 3.11a), and a single contiguous cluster with a single contiguous mass of "spacing" surrounding it (shown by the dashed line on the upper edge of 3.11a). For fractal surfaces, however, as gaps of all

spatial scales are present, the portions corresponding to the steepest slopes should be interpreted as the dominant scale of spacing.

As the differences in the spatial organization of heat islets are most apparent at higher temperature thresholds, here, we characterized the spatial structure obtained at the 90^{th} percentile of LST for all cities. In other words, the total *islet area* under consideration corresponds to the hottest 10% of the total city area. The largest box size taken under consideration is normalized from 0 to 100 to account for the variable sizes of cities. Note that the curvature of the Lacunarity curve was unaffected by these transformations.

Lacunarity curves for the four representative cities discussed in the previous section are highlighted (in colour) on top of other cities (in grey) in figure 3.11a. Cities with larger and aggregated heat islets also result in aggregation of gaps, as can be seen in case of Lagos and Jakarta Figure 3.8c). The lacunarity curve for these cities lay above the diagonal. Conversely, a dispersed spatial structure of the heat islets manifests as smaller spacings, such as Chicago and Guangzhou (Figure 3.8d) and the lacunarity curve falls under the diagonal. We assign a single score (Λ_{score}) to quantify the convexity of the curves in Figure 3.11a such that positive scores indicate larger spacing and vice-versa. This is achieved using the following empirical equation:

$$log_{10}\big(\Lambda(r)\big) = \left(1 - \frac{log_{10}(r)}{2}\right)^{2^{\Lambda score}} \tag{3.5}$$

where constants 1 and 2 are used to fix the end points of the curve at $log(\Lambda(r)) = 1$ and $log(r) = 2$, and the exponent, Λ_{score} is scale-independent measure of the shape of the lacunarity curve (See Methods section). The cities have Λ_{score} ranging between -0.9 to 0.6, and distributed normally (Figure 3.11b).

Therefore, in this framework, the complex spatial organization of heat islets can be quantified and compared using a single metric, Λ_{score}. Note that a bi-modal distribution corresponding to the two distinct classes was not observed. Rather, Λ_{score} was normally distributed around a mean value close to zero, indicating that most cities display a balance between the two extreme cases.

3.3.4 Intensity distribution

Analogous to the UHI Intensity, I introduce a *"heat islet intensity"* metric, where instead of setting rural temperature as a benchmark to study excess urban heat, the thermal threshold is used as a reference. The islet intensity, ΔT, is defined as the difference between the mean temperature of *each islet* and T_{thr}. Figure 3.12a shows the heterogeneity of their mean islet intensity for the city of Boston. At the percolation threshold corresponding to $T_{thr} = 19°C$, the set of heat islets each display a different value of ΔT. Within this set, larger islets have higher temperatures (Figure 3.12b), which is also observed at a city scale, where the UHI Intensity scales up with log of city size (indicated using population) [62]. The probability distribution of ΔTs captures the question: *"How much hotter are the islets than the threshold used to define them?"* and serves as a complementary metric of thermal variability across heat islets.

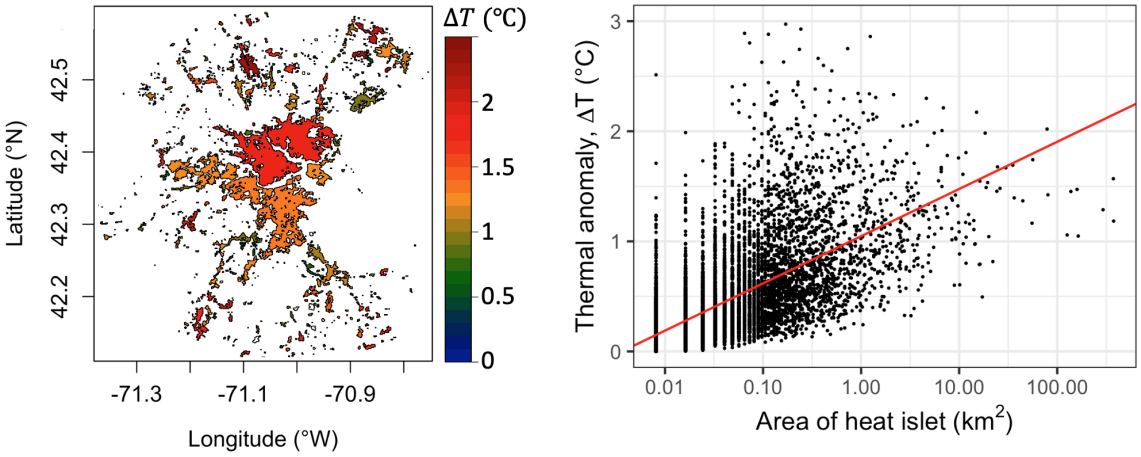

Figure 3.12. (a) Map of heat islets obtained for the city of Boston at percolation temperature (19°C, in this case) with colour representing the islet intensity (ΔT) above the threshold. Please refer to figure 3.2b for the original LST map of Boston. (b) Scatter plot of heat islet sizes and intensities (ΔT) shows the scaling of islet intensity with the log of islet size. The red line demonstrates the linear regression line corresponding to the following equation:$\Delta T \propto log(a)^{0.43}$; $R^2 = 0.4$)

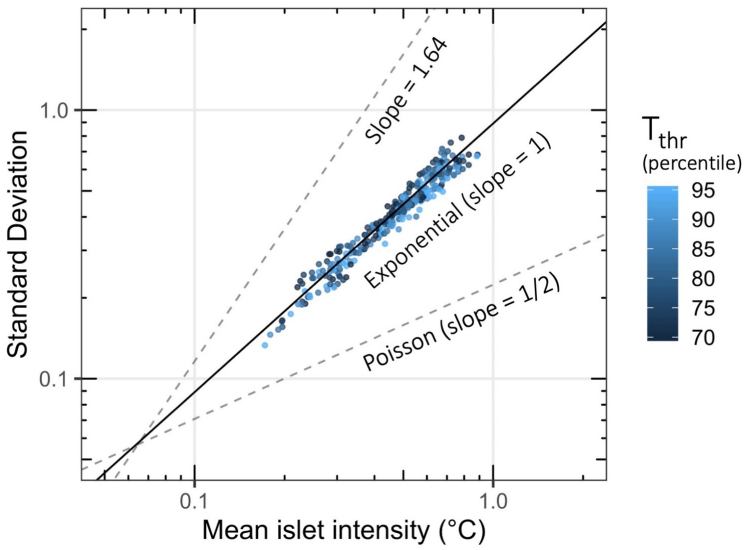

Figure 3.13. Scatter plot showing the correlation between mean islet intensity and its standard deviation. The solid line represents a slope (α) of 1 corresponding to an exponential distribution. Two additional dashed lines corresponding to the mean islet sizes (Figure 3.6) with $\alpha = 1.64$ (top) and poisson distribution with $\alpha = 1/2$ (bottom) are drawn.

For each set of islets obtained at a few thermal thresholds, mean and variance of ΔT values are estimated. The fluctuation scaling analysis of ΔT reveals that the fluctuations (std. devs.) are equal to the mean, indicating a scaling exponent $\alpha = 1$, which corresponds to an underlying exponential distribution (Figure 3.13). Unlike the fluctuation analysis of size distributions (Figure 3.6), no discernible pattern as a function of T_{thr} is observed. Expressed as an exceedance probability, the exponential distribution can be written as:

$$P(\Delta T \geq x) \propto 1 - e^{-\lambda x} \tag{3.6}$$

where the probability of an islet intensity, ΔT, exceeding a value x is represented by an exponential distribution characterized by λ.

The exponential distribution obtained for each city at their respective percolation thresholds are shown visually with the aid of an exceedance probability plot drawn

on semi-log axes (Figure 3.14a). Note that unlike the fractal dimension and islet size distribution, the islet intensity distributions vary widely across the cities. In figure 3.14b, the same is shown on a linear scale for all cities (in grey), with special emphasis on the 4 representative cities from figure 3.9. Lagos and Jakarta (shown in blue

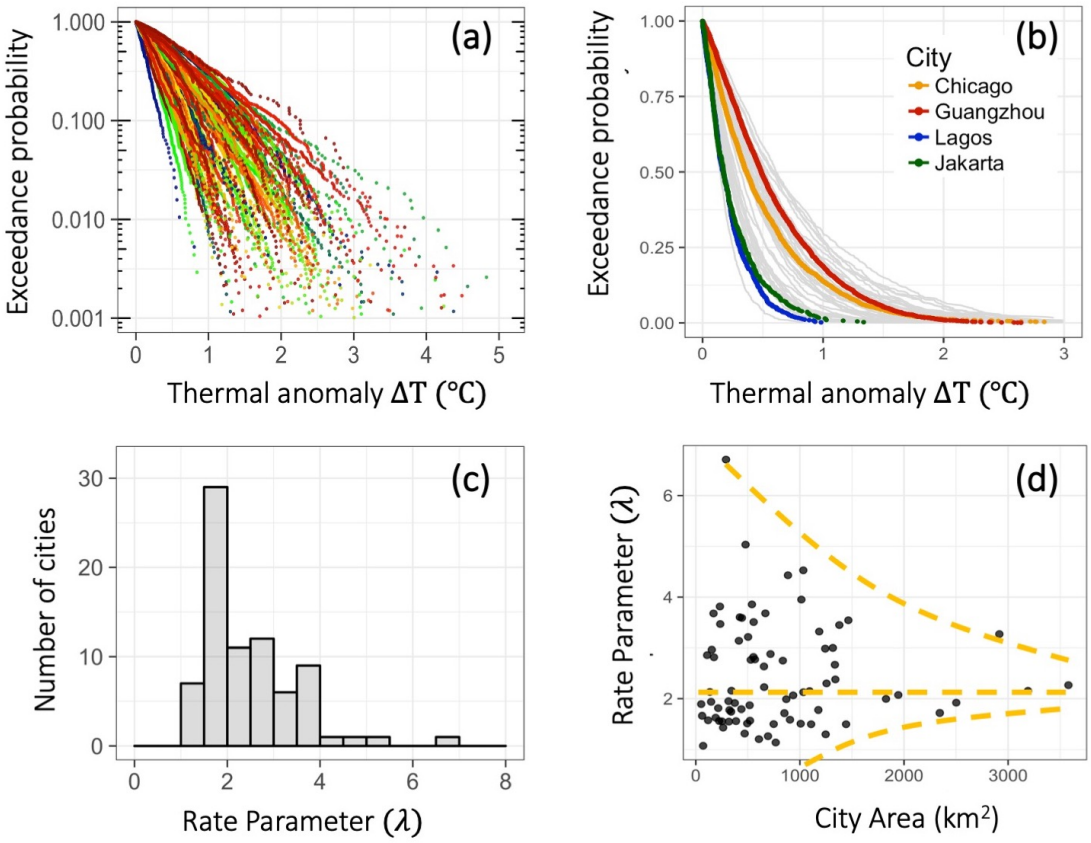

Figure 3.14. (a) Exceedance probability plots of islet intensities for all cities are shown on a semi-log graph with each color corresponding to a single city. This figure serves to illustrate the varibility in pdfs across all cities. (b) The exponential pdfs of ΔT for the four archetype cities is shown on a *linear graph* at their 90^{th} percentile thermal thresholds, respectively. The same for all other cities are shown in grey in the background. (c) Histogram of rate parameter λ (Eqn. 3.6) with mean $= 2.25K^{-1}$. (d) Scatter plot of λ and area where each point represents one city. Yellow dashed lines highlight the converging behaviour of λ with increasing area.

and green respectively) have a steeper exponential decaying rate than Chicago and Guangzhou (shown in orange and red), which drastically reduces the probability of local thermal extremes within their heat islets. This difference in rate parameters can have significant repercussions in terms of extreme temperatures. While the probability of a heat islet being hotter than the mean by 1°C is almost zero for the first two, the likelihood increases to roughly 20% for the latter two (Figure **??**a).

The rate parameters, λ, across cities display a log-normal distribution with a mean = 2.25 K^{-1} and s.d. = 1.47 K^{-1} (Figure 3.14c; see Table S2 for a complete list). Furthermore, it shows convergence to the mean with increasing city size as well (Figure 3.14d). By definition of exponential distributions, mean of the pdf = $1/\lambda$, which can be interpreted as the representative islet intensity for a given city. Higher values of $1/\lambda$ correspond to an increased probability of higher temperatures within the islets. Since, this pattern is consistent across all cities, a single metric, λ, can be used as a measure of intra-urban thermal heterogeneity. Furthermore, at a thermal threshold corresponding to the rural background temperature, this corresponds to the conventional metric of mean Urban Heat Island Intensity [4].

3.4 Synthesis of islet characteristics

In summary, here, I show that the spatial structure of Surface Urban Heat Island (SUHI) is strongly fractal for 78 diverse global cities. As a result, it can be conceptualized as a collection of **intra-urban heat islets** that occur as local heat clusters within the cities. The heat islets have remarkably similar spatial structure as characterized by the fractal dimension (D), as well as a power-law size distribution with exponent, β at the percolation threshold. This finding is rather surprising given the diversity of geographic, and socioeconomic constraints in the population of cities studied. This commonality indicates that despite the diversity in urban form and function across the world, the urban temperature patterns are different realizations with the same aggregated statistical properties. Difference among cities become ev-

ident at higher thermal thresholds, where deviation from power law is observed in the form of an exponential tempering (c). Further research into the relationship between urban morphology and the exponential tempering is discussed in section 4.1 which can provide some useful insights on urban design solutions for intra-urban heat mitigation.

The narrow distributions of scaling parameters and their convergence are also relevant to model the heat exchange between hot areas and their colder surroundings [4]. Current numerical weather prediction models, such as Weather Research Forecast (WRF) [11], use gridded data formats and, as a result, the perimeter of any heat islet is resolved to the minimum resolution (about $\sim 1 - 9$ km^2). This results in an under-estimation of urban perimeter boundary which is important for modeling heat exchange across the urban-rural transect. A fractal perimeter of iso-thermal contour lines indicates a larger perimeter of contact with cooler regions, which in turn enables a larger heat flux to dissipate from the heat islets. The inclusion of a correction factor to simulate a rough and convoluted perimeter (with $D \sim 1.33$) may improve the modeling of such processes. Furthermore, as the scaling metrics are rather narrowly distributed across diverse cities, we expect such a correction factor to be extendable across all urban areas.

As the pdf describing their distribution follows an exponential distribution, the intensity parameter (λ) can be used to characterize the heterogeneity of thermal extremes and compare across cities. An interesting finding is that while the cities corresponding to an exponential tempering have a significantly smaller area that attains higher temperatures, they are also more likely to experience extreme temperatures in more of the heat islets. This brings us to question, *"which one is better?"* More on this paradoxical observation will be discussed in section 4.1.

The scaling observed in the islet size and intensity distributions are analogous to the scaling laws known for areas and mean stages of lakes and wetlands [41, 47] and can be used to build the empirical basis for an investigation into the scaling theory of intra-urban heat islets. The proposed framework of identifying extreme heat clusters

by using incremental thresholds can be used to describe the patterns of extreme heat clusters in any thermal landscape. For instance, for exposure assessment of urban communities to heat, analysis of surface temperatures itself is not enough. Heat-stress assessment requires the joint consideration of air temperature and humidity [63]. Despite the difference in absolute values of UHI and SUHI, similarities between spatial patterns of the surface and air temperatures have been reported [64, 65]. Therefore, techniques of scaling based on SUHI patterns can be extended to spatial clusters of UHI as well. The additional challenge is to better understand the superimposition of intra-urban heat islets with the spatial distribution of vulnerable communities, such as the poor in mega-cities, the elderly, or critical urban infrastructure such as roads, power grids, and communication networks [66, 67].

Lastly, while the commonalities in the metrics derived here do not help in answering specific questions pertaining to a particular city, the convergence of the metrics with increasing size suggests a common attractor for all cities. Both λ and c were observed to decrease as the cities grow in size indicating an increased likelihood of occurrence larger and hotter heat islets for mega-cities indicating that their residents are at greater risk of extreme heat stress impacts. Therefore, while the effect of diverse urban morphologies is evident in smaller cities, in the mean, the larger cities are alike. This begs the question if this is an inevitable or a desirable trajectory for growing cities? Identifying the common statistical properties of the heat islets across diverse cities provides a means to escape from the geographical malaise of the uniqueness of place, and provides a step towards the improved characterization of its complex thermal landscape.

4. INFLUENCE OF URBAN AND CLIMATIC DRIVERS

Several factors influence UHI Intensity. The reduction of evaporative cooling in urban areas is generally thought to be the most dominant factor. Excessive anthropogenic heat release is another added input to the urban energy balance. Buildings and other artificial materials store more radiation energy in the daytime than can natural vegetation and soil, and release some of the stored energy at night, contributing to night-time UHI [68]. Energy redistribution through convection between the surface and the atmospheric boundary layer can either increase or reduce UHI Intensity, depending on whether the efficiency of convection over urban land is suppressed or enhanced relative to that over adjacent rural land [69, 70]. Finally, an extreme weather event such as a heatwave can disturb the energy budgets and modify the magnitude of UHI Intensity. Although these concepts have been known for some time, a quantitative understanding of their relative roles across different climate backgrounds remains elusive.

Notable studies that have addressed this question have highlighted that background climate plays a significant role in the UHI Intensity. This was also observed in my dataset of 100 cities, where cities located in dry desert climates (such as Cairo and Las Vegas) showed inversion of the UHI effect due to artificial irrigation of city compared to a hotter and drier rural background. Studies based on Community Earth System Model (CESM) simulation of the North American cities show that more than the difference in evaporative cooling between urban and rural areas, the variations in the efficiency with which urban and rural areas convect heat to the lower atmosphere is also a key driver of UHI Intensity [71]. Another study that analyzed MODIS-observed SUHIs of 30000 cities worldwide reported that SUHI Intensities could largely be explained by the climate type, classified in dry vs. wet regimes using the mean annual precipitation (P) as an indicator, and the city size, characterized by total population

(N). For drier regimes ($P < 1500mm/yr$), SUHI Intensity scales with P as well as log(N). However, in wet and humid regions such as Singapore, the influence of both diminishes greatly. Based on these results, the authors suggest that in arid regions, strategies that enhance evapotranspiration, such as green roofing, are effective ways to mitigate urban heat while different strategies (for example, increasing albedo or convection efficiency) will be needed in wetter climates [72].

In this section, I focus on understanding the impact of these drivers on the spatio-temporal dynamics of the intra-urban heat islets. I approach this question by classifying the drivers into two main classes:

1. Factors pertaining to the urban form and function, such as sprawl or compact urban forms (discussed in section 4.1)

2. Climatic background of the city and the mesoscale hydro-climatic forcings, such as heatwaves (section 4.2)

To elucidate the impact of these drivers in isolation, the following questions can be posed: "if two cities are identical in terms of morphological and anthropogenic characteristics but are placed in different climates, will they have the same UHI Intensity?". Similarly, regarding the importance of urban form, one can ask: "if two cities, very different in their urban form and function, are placed in the same hydro-climatic background and subjected to the same mesoscale event such as a heatwave, will the resultant thermal response vary?" To an urban planner, these inquiries can reveal how much heat mitigation is possible by urban design alone and for which climate backgrounds do urban design interventions fail to play a role. This question is particularly urgent now, as an additional 2.5 billion people are projected to urbanize by 2050, with over 90% of this increase taking place in developing countries of the global south.

4.1 Impact of urban form: Paradox of Sprawling vs Compact heat islets

A version of this section is published in Scientific Reports[1].

Cities grow through a combination of parallel and sequential episodes of **expansion** and **densification** at different rates [73, 74]. Depending on local preferences and geographical constraints, neighborhoods are built with different spatial patterns, from dense downtowns to sprawling suburbs. Factors like topography, coastline, and intra-urban commuting time constrain expansion, whereas other factors such as local building laws limit densification. While there are several objective functions such as commuting travel time distribution, net carbon emissions, and socio-economical factors which urban form and functions are optimized for, another growing concern is the aspect of urban heat. From this viewpoint, a natural question follows: *"Is there any optimal trajectory of urban growth that can minimize excessive urban heat?"*

There has been a substantial amount of research towards this question that spans a multitude of spatial scales. At the micro-scale, i.e., within the urban canyon, the surface temperatures are extremely sensitive to the geometrical details of immediate surroundings, such as street canyon geometry, sky-view factor, vegetative fraction, solar access and shading [75–77]. At a neighborhood scale, i.e., from a few hundred meters to a few kilometers, consistent thermal patterns emerge due to locally homogeneous patches of urban form and function [17, 18]. Studies investigating local scale impact of urban form report that high-density urban development leads to higher local temperatures since many of the mechanisms producing the UHI effect are often most pronounced within dense urban cores [19, 78]. In contrast, several others note that sprawling urban development may result in worse thermal conditions since it results in more land clearances, impervious surfaces, and excess heat generated per capita when compared to higher density development [79, 80]. Furthermore, Debbage and Shepherd (2015) [14] show that for air temperature based UHI assessments, re-

[1]Shreevastava, A., Bhalachandran, S., McGrath, G. S., Huber, M., & Rao, P. S. C. (2019). Paradoxical impact of sprawling intra-Urban Heat Islets: Reducing mean surface temperatures while enhancing local extremes. Scientific Reports, 9(1), 1-10.

gardless of the urban density type *within a patch*, the relative spatial contiguity of these land use patches is a critical variable as well. As a result, we do not have a clear consensus on the optimal urban form and function to minimize excess heat locally as well as at a city-scale.

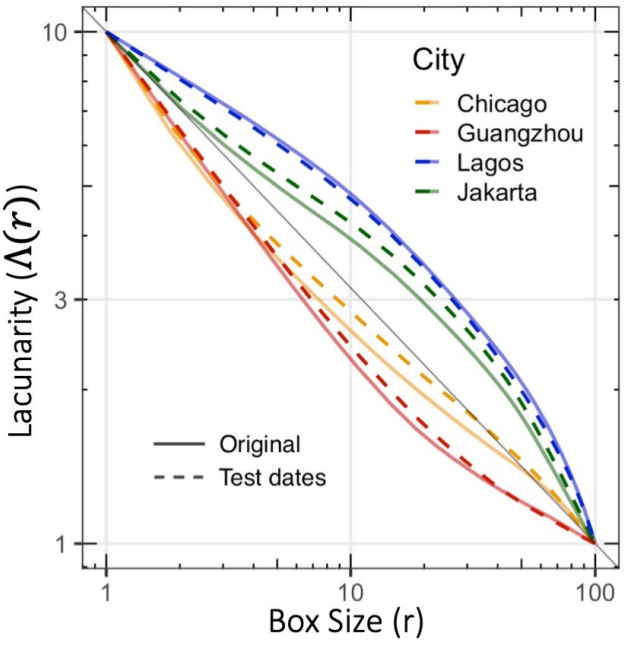

City	Time of acquisition (TOA) of the original image	Original Lacunarity Score	TOA alternate image	New Lacunarity Score
Lagos	(2013-12-18 10:04:25)	0.579	(2016-02-10 10:02:55)	0.684
Jakarta	(2018-07-06 02:59:11)	0.317	(2014-09-13 03:00:14)	0.524
Chicago	(2014-09-23 16:35:10)	-0.313	(2016-05-23 16:34:42)	-0.209
Guangzhou	(2016-02-07 02:52:07)	-0.873	(2017-10-23 02:52:25)	-0.591

Figure 4.1. Lacunarity analysis for two separate Landsat derived LSTs of the four archetype cities is conducted. Lacunarity Score (Λ_{score}) obtained for both dates are presented in the table below. Note that while there is a slight difference in the actual Λ_{score}, the curves still serve to illustrate a consistent pattern of spatial organization.

Here, I focus on the impact of spatial distribution of the heat islets on the local and city-scale heat island. I use the metric of Lacunarity to quantify the degree of sprawl and compactness of heat islets. Note that the terms "sprawl" or "compactness" in this context do not refer to the spatial organization of urban assets such as buildings or impervious areas. Instead, they refer to *the overall organization of heat islets across the city*. Recall that negative Λ_{score} correspond to small and dispersed (in other words, sprawling) heat islets, and positive Λ_{score} corresponds to large and contiguous (compact) heat islets. One caveat here is that as temperatures are temporally variable itself, the spatial organization of heat islets may change significantly as well. However, in figure 4.1, I show that while there is some change in the Lacunarity Score (Λ_{score}) corresponding the change in LST values (obtained using two separate Landsat images), the indicator still reveals the underlying organization (compact vs. sprawling) that stays consistent. Therefore, Lacunarity should be interpreted as a multi-scale organization indicator, wherein, the value of the index lies in its slope with respect to the spatial scale (box size, r), and therefore, the exact Λ_{score} should not be taken too literally. In particular, the impact on two key properties: islet size and intensity distribution is discussed in the following sections (sections 4.1.1 and 4.1.2, respectively).

4.1.1 Lacunarity vs Size distribution

Dense urban growth occurs when there is increased in-fill construction within the existing high-density built-up area. Such a process is often driven by economic and socio-political factors that lead to the settlement of new urban regions close to the city center [81]. This is akin to the preferential attachment phenomenon observed in complex networks where a new node is more likely to agglomerate at the "hub nodes" with the highest density of edges [82]. Densification within urban areas would result in hot regions getting hotter and larger, thereby resulting in power law size distributions of heat islets [54]. Urban expansion in the form of sprawl, on the other hand, occurs at

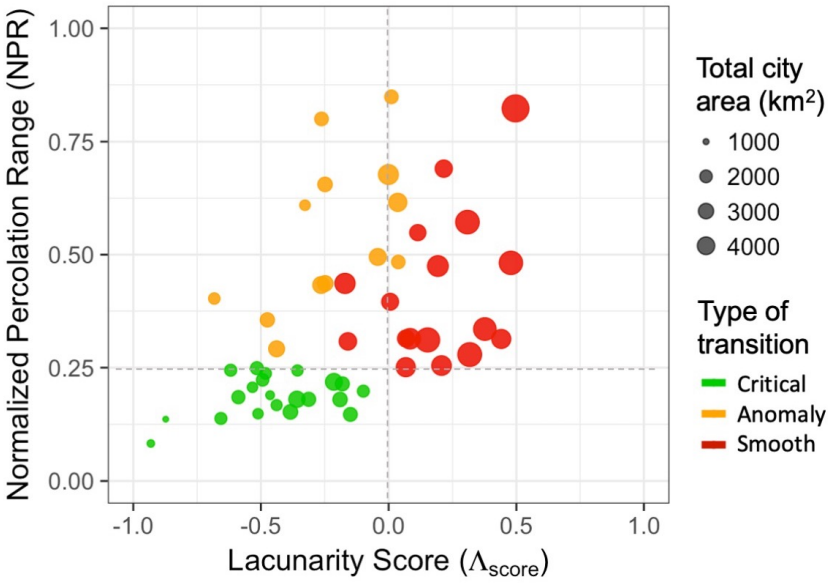

Figure 4.2. Scatter plot of Normalized Percolation Range (NPR) and Lacunarity score (Λ_{score}). This figure illustrates the classification of cities into the 2 classes based on Lacunarity Score and the type of transition (Critical vs. smooth) associated with each.

the periphery of urban areas in the form of growing suburban regions. This, in turn, would lead to the emergence of heat islets that are spread more evenly throughout the city, often interspersed with local heat sinks. In the size distribution, this should manifest as a fast decaying tail in the form of an exponential tempering [83]. As a result, the two classes of size distributions discussed in section 3.3.2, must correspond to sprawling and compact heat islet organization. Similar effects of urban form are observed on the power law distributions of several other urban infrastructure systems such as roads and sewage networks [25, 55, 84].

To test this hypothesis, we compare the relationship between Λ_{score} and the Normalized Percolation Range (NPR; figure 3.10), and by extension, probability of exponential tempering at higher thresholds. We find that the dense cities associated with an aggregated heat islet structure (positive Λ_{score}) display a larger NPR, referred to as a smooth transition (≥ 0.25; Figure 4.2). Whereas, sprawling and disaggregated

cities (negative Λ_{score}) have a smaller NPR, referred to as a critical transition (< 0.25; Figure 4.2) and consequently an exponential tempering of the power law tail (Figure 4.2). An exception to this pattern are cities that show a negative Λ_{score} despite corresponding to an NPR ≥ 0.25 (shown in yellow in Figure 4.2). Upon examination, we found these to have a significant river flowing right through them. Under such a scenario, the percolating heat cluster is divided structurally into two halves by a heat

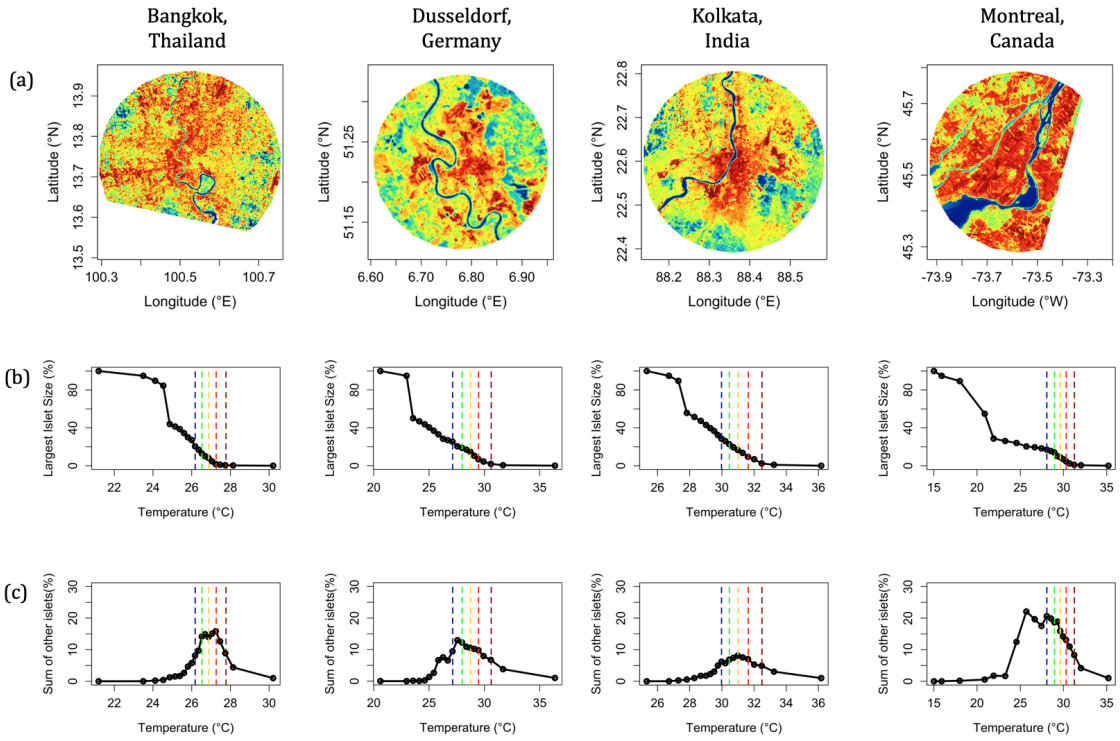

Figure 4.3. Some examples of anomalous cities with a river flowing between them, resulting in a negative Λ_{score} and large Normalized Percolation Range (Figure 3b) are shown here. (a) Land Surface Temperature maps for Bangkok, Dusseldorf, Kolkata, and Montreal. (b) Largest cluster size (A_L) as a function of thermal threshold shows the sharp decrease in cluster size at lower thresholds which is **not** corresponding to a rise in the size of other clusters. This is because the largest cluster merely breaks into two in these cases due to a central river (at low temperature. As a result, these are not classified as a critical transition as per percolation theory.

sink (the river), irrespective of the threshold (Figure 4.3). This results in a negative Λ_{score} due to the spacing introduced by the river despite an aggregation of heat islets on either side of the river. Thus, Figure 4.2 serves to quantitatively affirm the correlation between the spatial configuration of cities (dense versus sprawling) and the two classes of size distributions of the heat islets. From an urban planning perspective, this indicates a significantly reduced probability of encountering large heat islets for sprawling cities.

4.1.2 Lacunarity vs islet intensity distribution

I now focus on the heterogeneity of heat contained within the heat islets. To address this, we first use the well-known indicator of excess heat in urban areas, the SUHI Intensity in the traditional sense, i.e., the difference between the mean urban and rural temperatures [85] to evaluate the average excess heat within cities. We find that larger Λ_{score} values (representative of aggregated heat islets) tend to be associated with higher SUHI Intensity (Figure 4.4). This suggests that sprawling cities, with a larger number of heat sinks to match the heat sources, are a better configuration for reducing the *overall* SUHI Intensity. This outcome is also in agreement with our conclusions based on the size distribution of extreme heat islets as well as prior research based on the discontiguity of urban patches derived from the National Land Cover Dataset (NLCD) for US cities [14].

For a more comprehensive assessment of the thermal variability within cities, however, we compute the *Heat Islet Intensity* distribution of the excess heat (ΔT) within each islet. Recall that lower values of λ correspond to an increased probability of higher temperatures within the islets. By extension, $1/\lambda$, which is the mean islet intensity, is directly proportional to ΔT variability across islets. $1/\lambda$ is represented as the color bar in Figure 4.4. From heat islet analysis, we find that while cities with a higher degree of sprawl have a lower mean temperature, for the same SUHI (Y-axis in Figure 4.4), cities with lower Λ_{score} also experience a higher likelihood of

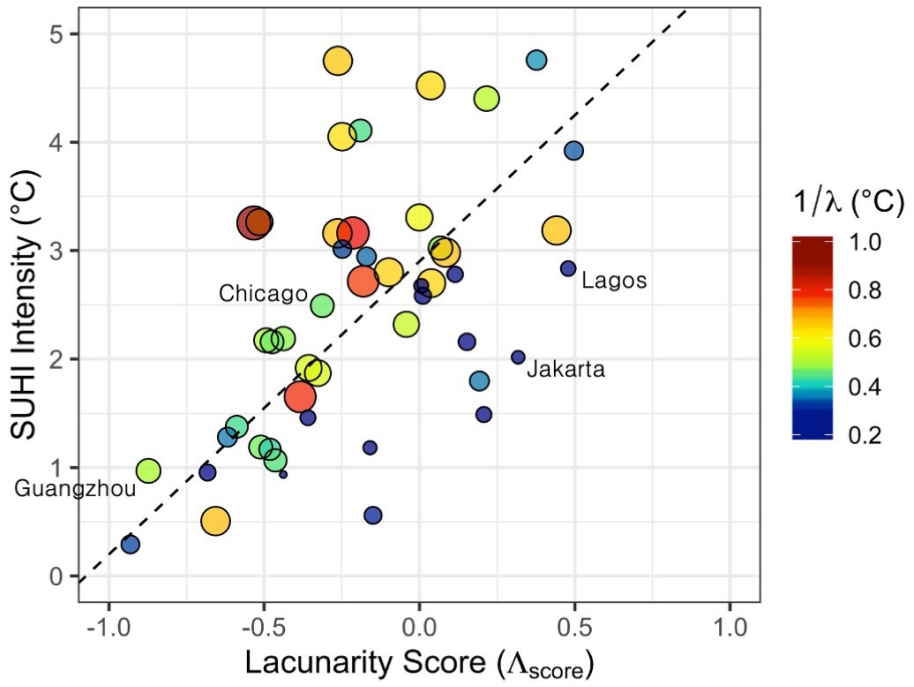

Figure 4.4. A scatter plot of mean SUHI Intensity, defined as the difference between mean urban and rural temperatures versus Lacunarity Score (Λ_{score}), is shown. A weak positive correlation ($R^2 = 0.344$) is detected shown as dashed regression line. The color, as well as the size of the marker, indicates the inverse of rate parameter (λ) from Equation 3.6, which is equal to the mean Heat Islet Intensity for each distribution. Increasing size indicates a likelihood of higher temperatures within the heat islets.

encountering thermal extremes. For example, dense cities such as Lagos and Jakarta have a steeper exponential decaying rate than Chicago and Guangzhou, which drastically reduces the probability of local thermal extremes within their heat islets. As the larger heat islets are often associated with the highest islet intensity as well, this can result in significantly large areas of extreme heat, especially for megacities like Guangzhou and Chicago. Such a finding reveals that while mean SUHI Intensity decreases with sprawling cities, for the same mean, they also experience higher local thermal extremes. As a result, in addition to the mean SUHI Intensity, it is essential

to characterize the thermal heterogeneity within the cities, and the islet intensity distribution can be adopted as a complementary metric.

4.1.3 Size vs Spacing: Intra-urban differences

In this section, I take a detour to explore the various combinations of size and spacings that yield diverse heat islet configurations. Heat islet maps for all cities are obtained at a 90th percentile threshold to focus on the spatial structure of hottest 10% of each city for this experiment. Two scale scale-independent metrics to characterize size: Mean (A_M), and Largest (A_L) Relative Heat Islet Sizes calculated as a percentage of the total city area and a more intuitive indicator of islet sizes than β.

First, we observe that there is a weak positive correlation ($R^2 = 0.4$) between A_M and spacing of the heat-islets (Figure 4.5a). This is expected because a positive Λ_{score} as well as a high A_M corresponds to dense cities, and a negative Λ_{score} and low A_M corresponds to sprawling cities. More noteworthy is the horizontal spread about the diagonal, which represents different spatial configurations (characterized by Λ_{score}) that are possible for the same A_M. This spread may be explained by A_L, which increases with Λ_{score} (illustrated using marker size in Figure 3.11d; Supplementary Figure 5). In the bottom-left, both A_M and A_L are small. This is because negative Λ_{score} corresponds to sprawling cities where large clusters were absent in the islet-size distribution (as inferred from the exponential tempering of power law). In the bottom-right, however, the dominance of the largest aggregated islet results in a positive Λ_{score} despite a low A_M value. This kind of a phase space plot for size and spacing may be useful to gauge the current spatial structure of a given thermal landscape and to determine mitigation strategies towards a more desirable state.

The size vs. spacing phase plot can also be used to explore local differences within a city's boundaries. Here, I start with the four archetype cities and crop concentric circular subsets with an increasing radius starting from the geographical center of each city. Analyzing where each subset lies on the phase space plot as a function of

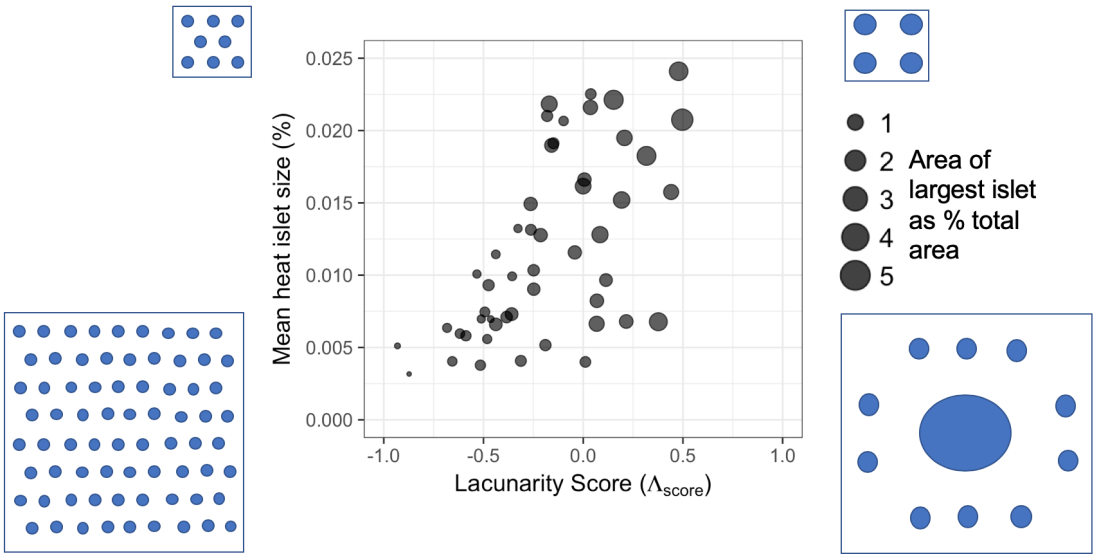

Figure 4.5. Scatter plot of Mean Relative Heat Islet Size (A_M) versus Λ_{score}. Additionally, the largest islet size (A_L, as a percentage of the total city area) is indicated using the marker size. These two metrics indicate the size distribution of the hottest islets occupying the hottest ten percent of the city area. On the sides, corresponding to each quadrant of the phase space, schematic diagrams of the spatial structure of heat islets are shown to exemplify the various spatial configurations that are possible for cities. Since A_M scales inversely with the total city area, the top two schematics are drawn to represent smaller cities.

the cropping radius can reveal interesting patterns of sprawl vs. compactness within radial zones of a city.

First, the scatter plot of total area under consideration is plotted against Λ_{score} in figure 4.6a for all cities (in grey), as well as the circular subsets of the four archetype cities (in colour). We note that both types of cities start with a positive Λ_{score} which indicates compact structure of heat islets. As the cropping radius increases, more heat islets are captured across the region and the points move towards the left side, indicating sprawl. In case of Guangzhou (in red), this trend continues as more and more heat islets are encountered even at the peripheries resulting in a gradual shift to negative Λ_{score}. The shift towards sprawl appears to be balanced for Chicago (in

orange) where above a certain cropping radius, the Λ_{score} doesn't change. This could indicate expansion and densification in equal parts. On the other hand, for compact cities (Jakarta in green and Lagos in blue) an inflection point occurs after which the trajectory sharply turn towards a more positive Λ_{score}. This is because the contiguous heat islets are aggregated towards the city center and increase in radius only adds to more spacing, thereby increasing Lacunarity.

These trajectories are then studied in the context of the phase space plot (Figure 4.6b). We first note that all the cities start in the same region, but as the urban area increases, the influences of densification and expansion becomes increasingly evident. The marker size in Figure 4.6b represents the total area in consideration. As A_M is inversely proportional to total city size, the trajectories are flipped between the two plots. Consistent with the previous plot, the sprawling cities move along the diagonal, whereas, the dense cities show a sharp increase in Λ_{score} beyond certain cropping radii. Thus, in the phase plot, the movement along the diagonal from top-

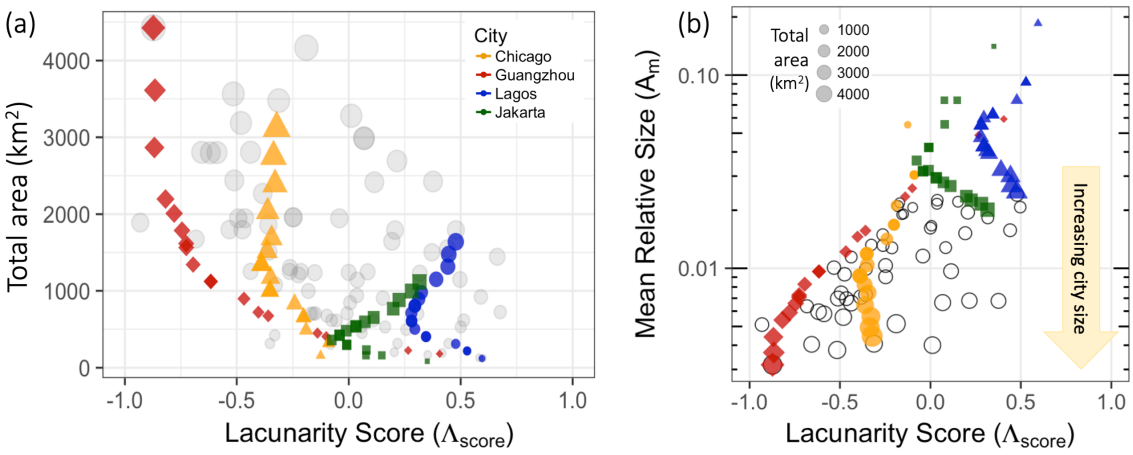

Figure 4.6. Scatter plot of Area Size vs. Spacing for all cities (gray circles) with subsets of the four megalopolises - Lagos (Blue triangles), Jakarta (Green squares), Chicago (Orange circles), and Guangzhou (Red diamonds). For each of these, the city area is cropped at the center for different radii. The marker sizes represent the total area under consideration for each subset.

right to bottom-left may be interpreted as continued expansion, while the shift of the diagonal represents the development of multiple hubs or polycentric structures perpendicularly away from the diagonal may be interpreted as densification.

Even though megacities converge to a similar spatial pattern as a whole [86], the neighborhoods that agglomerate to form the megacity still display the variability consistent with that observed in smaller cities. Thus, larger cities can be conceptualized as a collection of heterogeneous neighborhoods, but local-scale variations are overwhelmed by larger-scale patterns. These results are in accordance with topological analyses of urban drainage and water supply infrastructure networks in diverse cities [25, 55]. Thus, the phase plot of A_M and Λ_{score} may be used as a useful metric for city planners to gauge the current extent of expansion and/or densification and to determine mitigation strategies for future trajectory from the current state.

4.2 Impact of a heatwave

Heatwaves (HW) are usually defined as anomalously hot periods that last several consecutive days, resulting in higher levels of heat-related discomfort, diseases, and unusually higher death toll [87]. Despite being a slow and silent killer, HWs claim more lives every year than all the other meteorological hazards combined[2]. Some of the deadliest and most well-documented examples in the last few decades have been the 2003 European HW and the 2015 Indian HW, which claimed thousands of lives. Such cases are on the rise as HWs get more intense, more frequent, and longer-lasting under the changing climate [1, 88].

Moreover, a disaster like a HW has vastly different impacts on different socio-economic population groups. As an individual's problem, extreme heat can be combated rather easily with excessive air-conditioning. While the rampant use of air-conditioning in the affluent parts of the cities cool down the buildings internally, it leads to an excess emission of anthropogenic heat flux outside, further increasing the

[2]Source: `https://www.weather.gov/hazstat/`

ambient temperatures for those who are exposed and vulnerable to it. Thus, the consequences of heat stress are borne disproportionately by the urban poor. Apart from the loss of human life, as power consumption surges, power grids become prone to cascading failures during HW episodes, thereby increasing the probability of blackouts [89]. In the 2003 HW over New York City (NYC), for instance, the mortality rate increased by 25% as a result of the subsequent blackout [90]. On a larger spatio-temporal scale, HWs cause damage to vast expanses of forests, croplands, water resources, and hydro-climatic balance. This puts further pressure on urban systems by rapidly depleting ecosystem resources in the short term as well as causing the uprooted rural populations to migrate into cities as climate refugees in the long term [91].

There are some consistent meteorological features that characterize HW events. They are generally the result of trapped air when anti-cyclonic circulation patterns result in a high-pressure system on top of a region (often thousands of Kms in size) and prevents effective circulation of air and dissipation of trapped heat [92]. However, there is no precise threshold that defines it. Some descriptions intrinsically include the human health aspect as they are defined as extreme hot periods, which results in higher human mortality. However, people in different climatic background get acclimatized to their local thermal extremes, either by natural conditioning or by artificial measures of insulation such as building heating and air-conditioning. For instance, the National Oceanic and Atmospheric Administration (NOAA) issues a heat stress warning above 33°C for some regions in the US, whereas in the tropical regions of India, up to 40°C does not warrant a warning[3]. In the absence of a standard definition, the use of percentile-based thermal thresholds based on local historical records of nighttime minima or daytime maxima has been recommended [87].

The interaction between these two extreme heat phenomena: HWs and UHIs, has attracted a lot of scientific interest over the last couple of years [68]. A key driving question has been: *"how does a HW modify the UHI Intensity"*? Prior research has shown that it results in a synergistic union where the sum is greater than the

[3]Source: `https://www.weather.gov/safety/heat-index`

parts, and higher amplitude of UHI Intensity is observed during a HW period [69,93]. However, the contrary is also observed in some cases where the UHI Intensity had reduced [94,95]. Here as well, we focus on the interaction between the two processes, which a specific focus on the spatio-temporal heterogeneity of urban thermal extremes. I use the Weather Research Forecast (WRF) model to simulate the 2018 European HW focused on the city of Paris because WRF simulates the spatio-temporal scales of both HW and UHI. Details of the case study selection are given in section 4.2.1, and the WRF model specifications are given in Appendix E. I then examine three key properties: (i) the UHI intensity (surface and air temperature-based, Section 4.2.2) (ii) the variance of intra-urban temperatures and (iii) the 2-D power spectral density of the thermal map is evaluated, which serves as an indicator of *spatial organization*. (Section 4.2.4). Note that due to the lower resolution outputs obtained from WRF ($\sim$ 1 km compared to 90 m from Landsat), we can no longer apply the framework of thermal thresholding to obtain sets of heat islets. As an alternative, the 2-D power spectral density of the thermal map is evaluated, which serves as an indicator of *spatial organization*.

4.2.1 Data: WRF simulation of the European HW 2018

Europe has been experiencing record-breaking summers of high heat every year and the summer of 2018 experienced a series of HWs over various regions. Here, I focus on the metropolitan region of Paris to study the impact of HW on its UHI. For this investigation, the air temperatures obtained from the Reanalysis dataset for 2018 are compared against the expected average temperature for the day based on the reanalysis dataset of air temperature over the last decade to highlight the anomalously hot periods. The 'expected temperature' for each day during the period of interest was calculated by averaging the air temperature values from 2006 to 2016 for that day and then applying a 7-day smoothing (Figure 4.7). Based on this, a sample set of 11 days corresponding to two distinct HW episodes from July 23$^{\text{rd}}$ to July 27$^{\text{th}}$ and

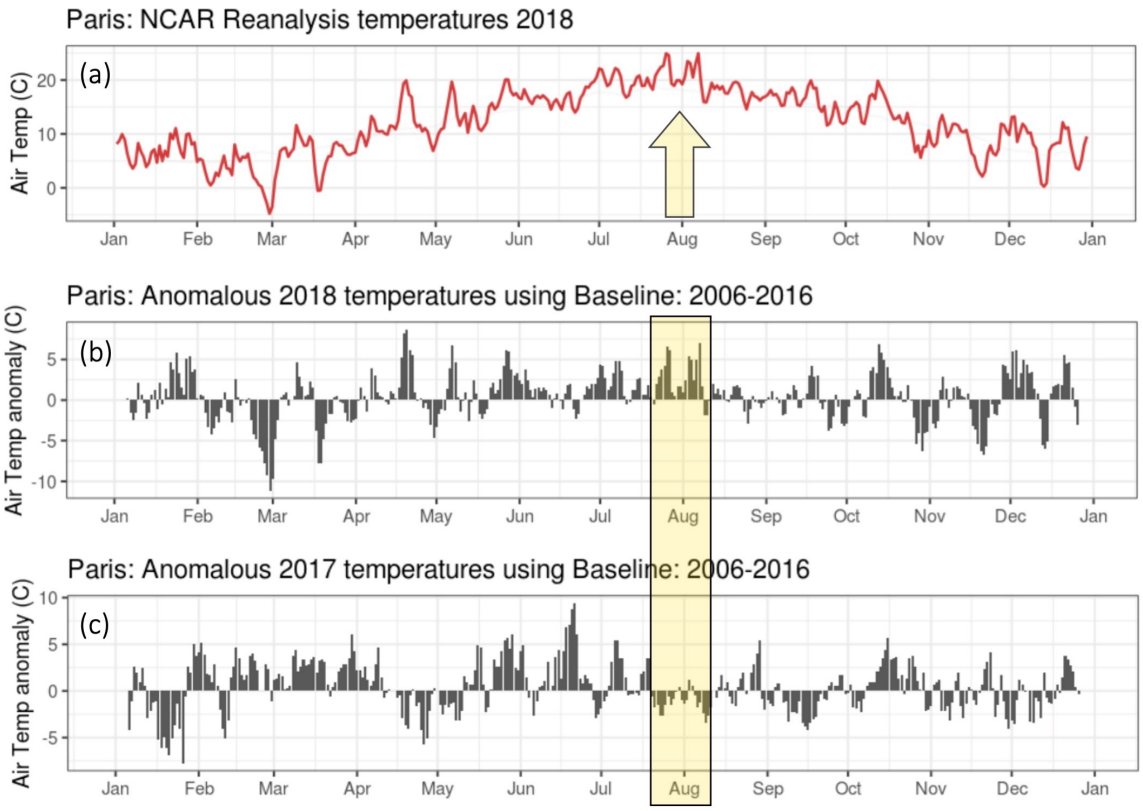

Figure 4.7. (a) Time series of Air temperatures in the Paris metropolitan region during the year of 2018. The air temperature dataset was obtained from NCAR's Reanalysis data. The hottest periods of the year corresponding to July 25th - August 5th are selected here as a HW event. (b) Thermal anomaly experienced in 2018 calculated as the difference between 2018's reanalysis air temperature and the baseline temperature, which was calculated as the average temperature by day over the reanalysis dataset over Paris from 2006 to 2016 and then applying a 7-day smoothing. (c) The same time period in 2017 is simulated as well as a representative of non-HW conditions.

then from August 3rd to August 7th (Figures 4.9 and 4.10) are identified as HW days. The days after the two episodes were not used as a representative of non-HW days to avoid any effect of the residual heat. Instead, the same time period corresponding to the HW days but from the previous year, 2017, was used as a representative baseline of no HW event.

Paris was chosen because it is a large city with conspicuous intra-urban variability, and the UHI effect is captured in the WRF environment (resolution $\sim$ 1 km) as well as its distance from the coast that minimizes the effect of coastal winds in the said interaction [89]. A triply nested domain structure is designed such that the smallest domain (resolution = 1 km) is centered on the city of Paris, mid-sized domain (resolution = 3 km) covers several other European cities such as London, Frankfurt, Amsterdam, etc., and the largest domain (resolution = 9 km) encompasses western Europe (Figure 4.8a). The simulations are driven by ERA-interim reanalysis data provided by European Centre for Medium-Range Weather Forecasts (ECMWF)[4] at 6-hour intervals as atmospheric boundary conditions and the surface boundary con-

[4]Source: `https://rda.ucar.edu/datasets/ds627.0/`

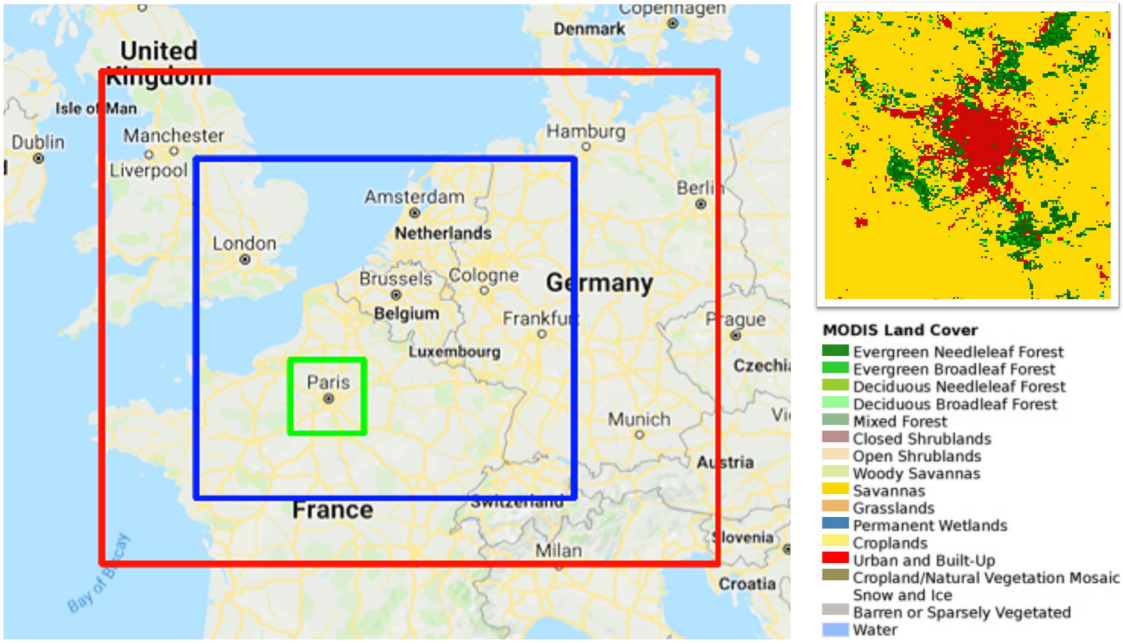

Figure 4.8. The three nested domains used in WRF simulation. The domains' horizontal resolutions are 9, 3, and 1 km (from largest to smallest), respectively. Domain 3, centered over Paris, has 163 163 horizontal grid points. (b) Land Use Land Cover map of Domain 3. The urban area of Paris is shown in red.

ditions are derived from MODIS (Figure 4.8b). The resultant output has a temporal resolution of 3 hours for domain 1, and 1 hour for domains 2 and 3. The simulation was run from July 20, 00 GMT, to August 9, 00 GMT, and a 24-h model spin-up period was allowed before the data was collected for analysis. For other details about the WRF simulation, please refer to Appendix E.

4.2.2 Urban Heat Island Intensity

The spatio-temporal dynamics of air temperature (estimated at the height of 2 meters above the street level and referred to as T2 in WRF) as well as surface temperature (estimated a representative skin temperature for all urban surfaces within a grid cell, LST) is discussed here. While the two fields are correlated, they show different diurnal patterns (Figures 4.9 and 4.10). During the daytime, Surface Temperature is higher than air temperature due to incoming solar radiation, whereas the air temperature is higher during nighttime due to the delayed outgoing longwave as well as anthropogenic heat fluxes. This is illustrated as a scatter plot between the two variables, where each point represents an individual grid cell in domain 3 (Figure 4.11). During the night time (e.g., 11 pm, 2 am, and 5 am), the points lie above the dashed 1:1 line indicating that $T2 > LST$, whereas during the daytime (e.g., 11 am, 2 pm, and 5 pm), the points shift significantly below the 1:1 line indicating that $LST > T2$. Moreover, a wider horizontal spread shows higher heterogeneity in LST during day time with a distinct cluster of points emerging on the right that corresponds to urban areas. This can also be seen as the distinctly hotter urban region that appears during daytime in the LST plots (Figure 4.10), and during nighttime in the T2 plots (Figure 4.9).

Figures 4.12a and 4.12b served to illustrate the time series of averaged LST and T2 over domain 3, as well as UHI Intensity calculated as the difference between mean urban temperature (corresponding to all urban classes) and rural temperature (estimated as an average over all other types of surfaces except water). First, we

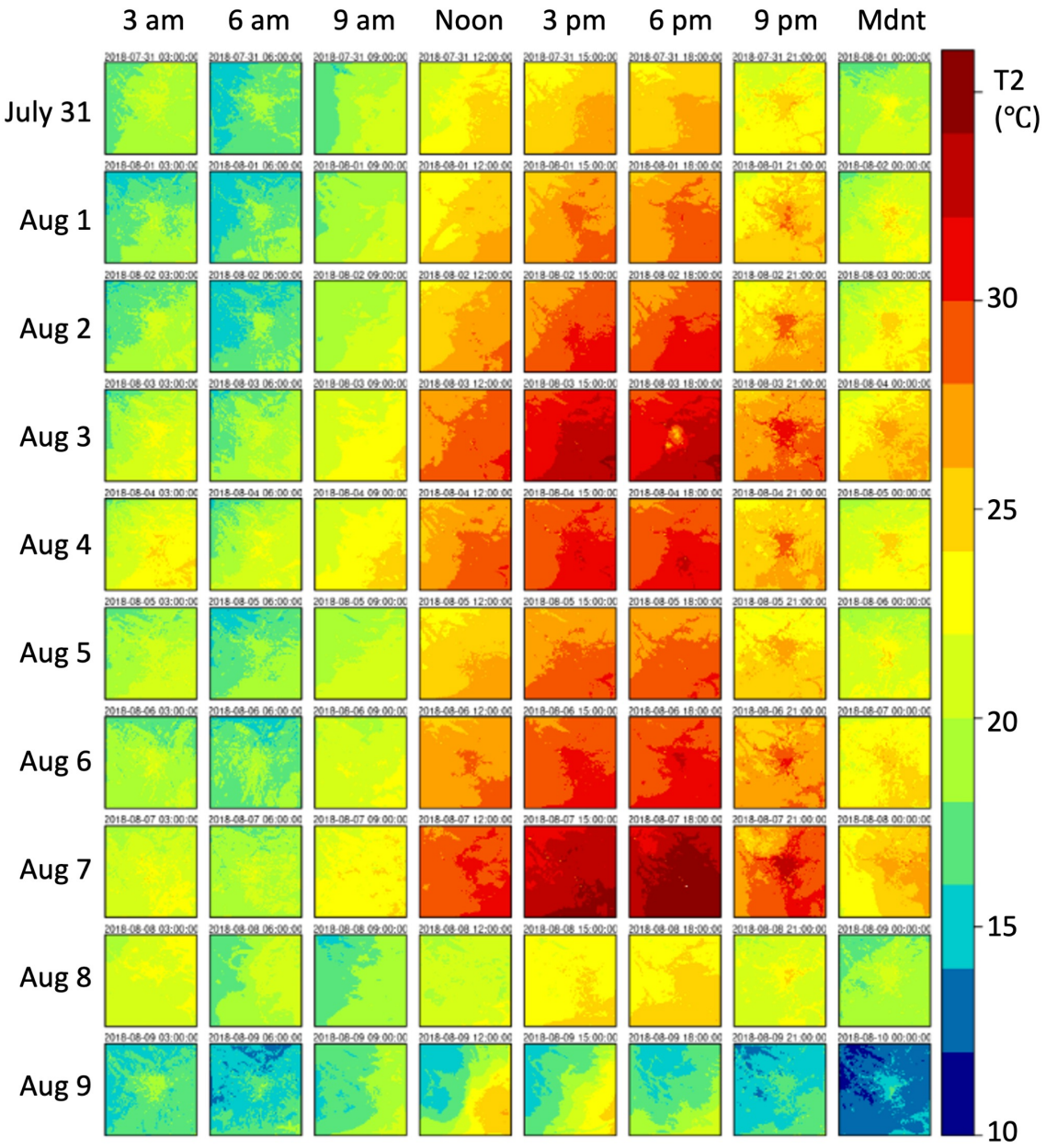

Figure 4.9. Example of spatio-temporal pattern of air temperatures (T2) over domain 3 shown at three-hourly intervals for ten days. The HW period is corresponding to higher daytime temperatures from August 3rd to August 7th. Note that the city in the center of domain becomes visible during the nighttime as T2-based UHI Intensity is the strongest during nighttime.

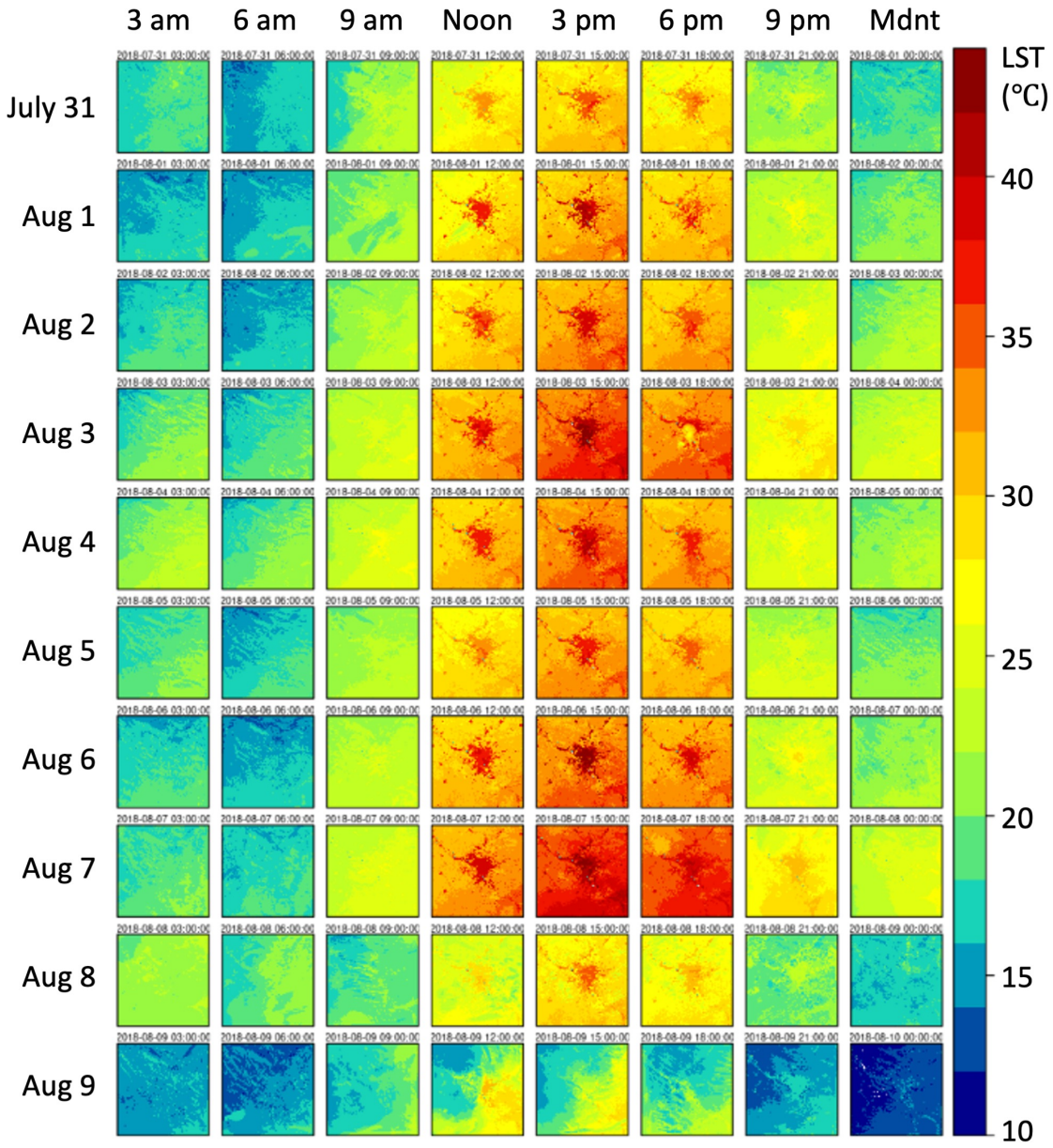

Figure 4.10. Example of spatio-temporal pattern of surface temperatures (LST) over domain 3 shown at three-hourly intervals for ten days. The HW period is corresponding to higher daytime temperatures from August 3rd to August 7th. Note that the city in the center of domain becomes strongly detectable during the daytime as LST-based SUHI Intensity is the strongest during the daytime.

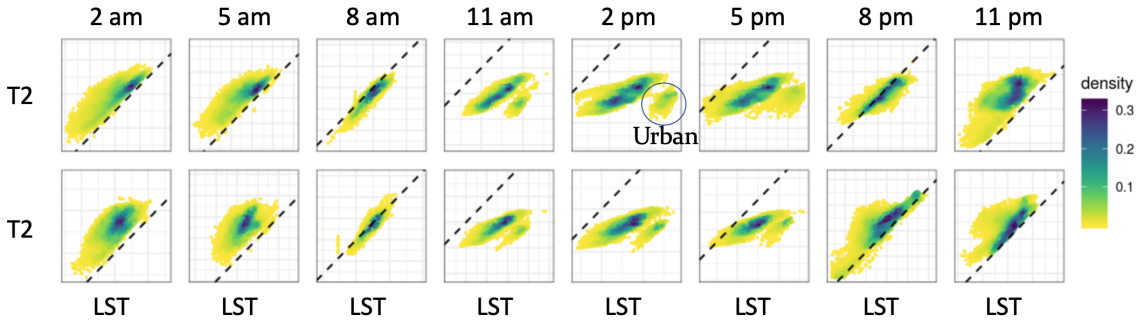

Figure 4.11. Scatter plot of air vs surface temperatures within Domain 3 is shown at a three-hour interval for 2 days. Here, a range of 12°C is maintained on both axes and the dashed diagonal line indicates 1:1 correlation line. The colorbar corresponds to the density of points in a region.

observe the UHI Intensity to be the strongest during night time with an inversion effect (negative UHI Intensity) during the daytime. Whereas, SUHI Intensity is also present during the nighttime and intensifies further during the day. The impact of HWs on both of these metrics can be most strongly and consistently observed during the nighttime. To illustrate that, the UHI Intensities are averaged by *each hour* across the five days, to generate the hour-specific average UHI Intensities (Figures 4.12c and 4.12d). Such a representation helps in ironing out the anomalies and focusing on the consistent diurnal trend alone. We observe that the UHI Intensities for both fields **decrease** in the HW scenario by almost 1°C on average during the night time. Thus, these findings in contradiction with the reported synergistic union between HWs and UHIs in some cases. The surface energy budget and soil moisture availability are explored in section 4.2.3 to explain the lack of synergy.

4.2.3 Surface energy budget analysis

Prior work on UHI-HW interaction has identified the difference in storage heat flux and moisture availability during a HW as a main driver of the synergistic outcome

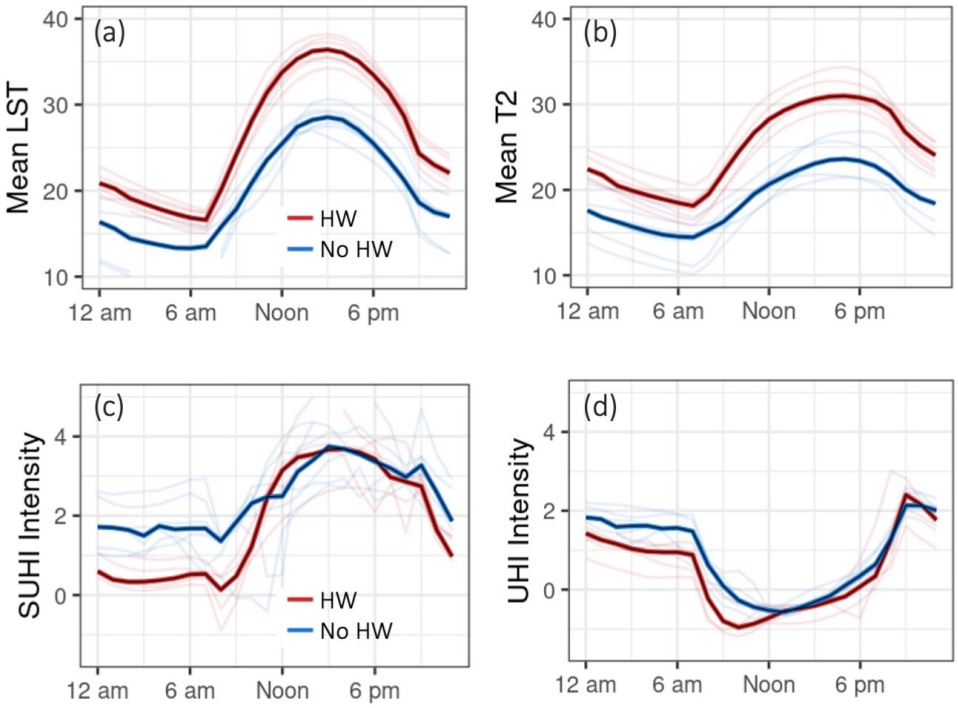

Figure 4.12. (a,b) Domain averaged LST and T2 over the five days (August 3rd, local midnight to August 8th) are shown as light-colored lines in the background. Hour-specific average mean LST and T2 are overlaid on the respective plots as dark solid lines. Red lines corresponds to HW (2018) and blue corresponds to non-HW scenario (2017). (c,d) SUHI and UHI Intensities, calculated as the difference between mean urban and rural temperatures are shown in the same format.

[70, 89]. Here, I study the surface energy budget between urban and rural areas and the moisture availability in and around Paris during the HW event. The surface energy budget of the urban canyon in the absence of significant windy conditions can be expressed as the following equation.

$$-Q^*\,(=-SW\downarrow -LW\downarrow +SW\uparrow +LW\uparrow) = Q_H + Q_E - Q_G + \Delta Q_S \qquad (4.1)$$

Here, Q^* is the sum of all four radiative components, i.e. incoming ($\downarrow$) and outgoing ($\uparrow$) shortwave (SW) and longwave (LW) radiations respectively (Figure 4.13).

SW↓, LW↓, Q_H, and Q_E are estimated within the model and provided as a WRF output variables, whereas SW↑ and LW↑ are calculated using the LULC properties such as albedo and emissivity. Q_H and Q_E are the sensible and latent heat fluxes respectively which are also given as a WRF output. Lastly, Q_G is the heat flux going downwards into the ground, and ΔQ_S denotes stored energy within the urban canopy layer. However, these two terms are not distinguished within the WRF environment and the combined term is referred to as either storage or ground heat flux term in the literature. Here, I refer to it as storage flux (denoted as Q_S) and calculate it as the Residual term in the energy budget. The negative sign in this equation indicates downward direction. The hour-specific average of each energy flux term is calculated for urban and rural areas within HW and Non-HW periods of interest and are shown in figure 4.14.

The incoming SW↓ term is modeled in WRF as a function of latitude and longitude of the location and the time of year. As a result, SW↓ is exactly the same for all four cases. The outgoing SW↑ term is calculated as *albedo*× SW↓. As urban areas are darker (albedo = 0.15) than the rural surroundings (albedo = 0.20), they

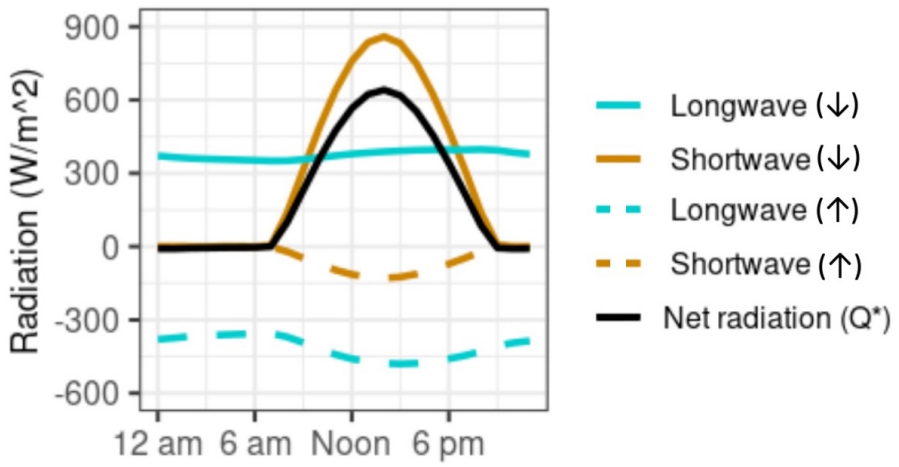

Figure 4.13. The diurnal trend of radiative components and the net radiation (Q*) are shown for an urban area as an example. The data is obtained by hour-specific averaging over the HW days.

reflect less SW↑. The LW↓ as well was observed to be the same for urban and rural areas, however, there was a significant increase ($\sim$ 40 W/m^2) for both urban and rural areas in a HW scenario. LW↑ is calculated as per the radiation equation, $\sigma \times emissivity \times LST^4$, where σ is the Stefan-Boltzmann constant ($= 5.67 \times 10^{-8}$ W/m^2 K^4). LW↑ for rural areas is found to be higher than the urban area by $\sim$ 20 W/m^2 in both HW and non-HW scenario. Although the urban LST values are higher than the rural LSTs especially during daytime (Figure 4.12), a higher emissivity of rural areas ($\sim$ 0.98) compared to that of urban areas ($\sim$ 0.88) results in higher LW↑ radiations. These terms are added to obtain the net radiation, Q^* (Figure 4.13). Net Q^* over urban areas is higher than rural areas by $\sim$ 40 W/m^2.

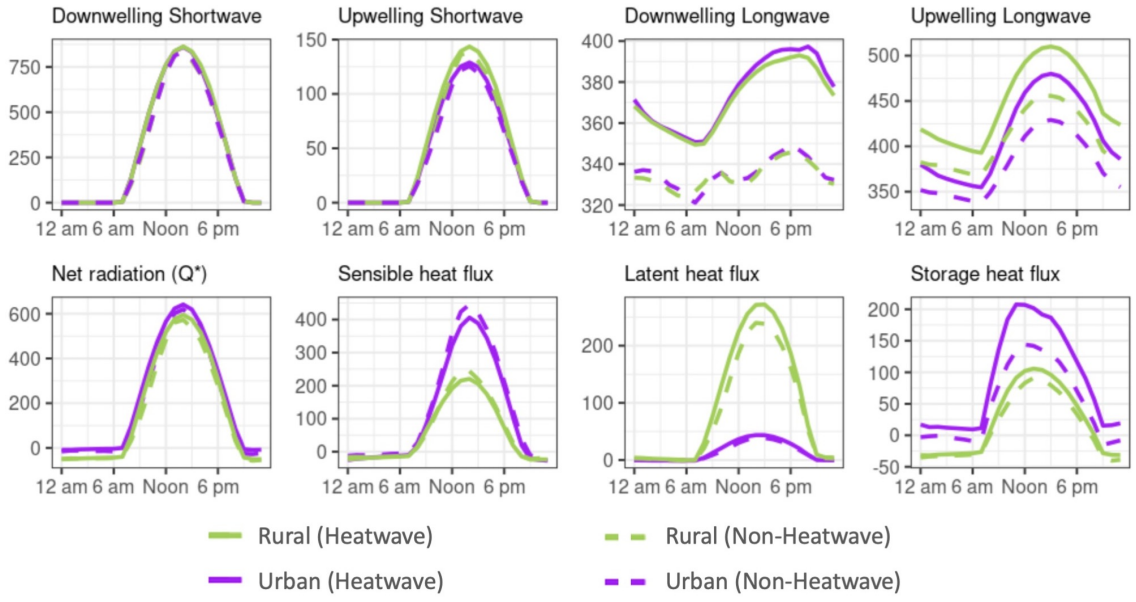

Figure 4.14. Diurnal trends for all the components of the surface energy budget are shown for urban and rural areas (shown in purple and green respectively). Solid lines indicate HW scenario, and dashed lines correspond to non-HW scenario. The y-axis for each subplot corresponds to energy flux and has the units of W/m^2. Please note that the y-axis for each variable is scaled differently according to its own maxima and minima. Note that the direction of each flux term is indicated in equation 4.1 are only the magnitude is shown here.

In another study, an urban site in Beijing and a nearby rural location for a HW event, in-situ observation towers were used to measure the radiative fluxes [70]. The results indicate that both the sites received more SW↓ ($\sim$ 150 W/m^2) during the HW event, and the urban site received more LW↓ ($\sim$ 20 W/m^2) than the rural site, resulting in a larger radiative energy input into the urban surface energy budget. The study also reported an increase in UHI Intensity during the HW, which was attributed to this additional energy input. However, this phenomenon was not captured in this WRF simulation.

The net radiation is then partitioned into three terms: Sensible (Q_H), Latent (Q_E), and Storage (Q_S) heat fluxes. Urban areas usually have a higher sensible heat flux due to reduction in moisture availability, whereas rural areas have a nearly equal split between sensible and latent heat flux. The partitioning is best captured using

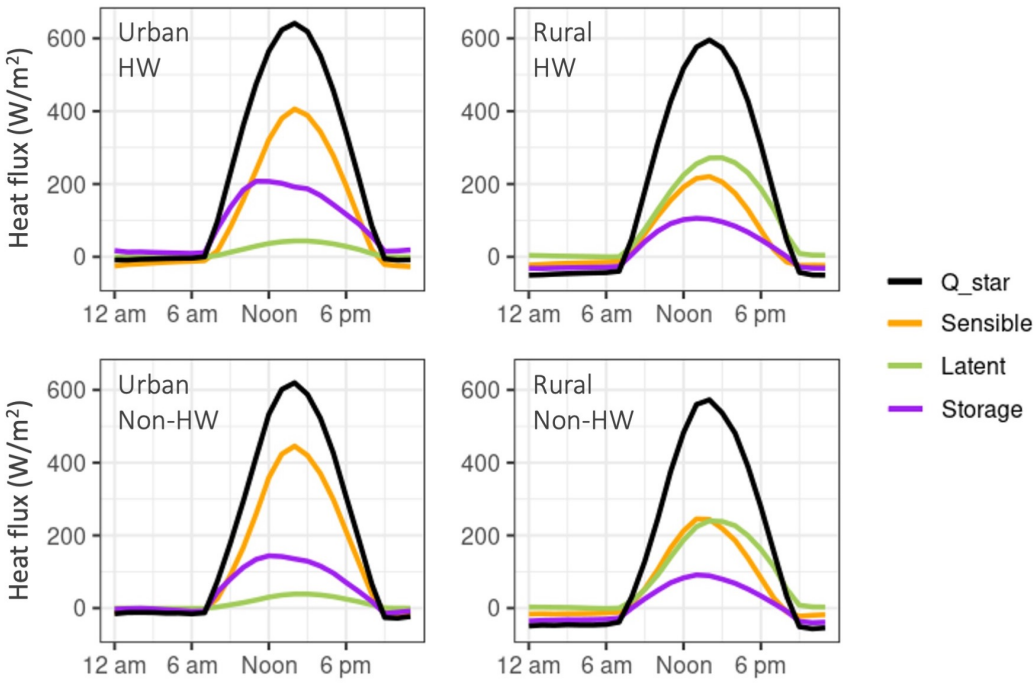

Figure 4.15. Energy partitioning of the net radiation (black) into sensible (orange), latent (green), and storage (purple) heat fluxes in W/m^2 for each case as labeled on the plot.

the metric of Bowen Ratio (defined as Q_S/Q_E). Bowen ratio for rural area changes from a median value of 1.1 to 0.9 under a heatwave scenario which is due to an increase in Q_E and a decrease in Q_S (Figures 4.14f and 4.14g). The same trend is observed in urban area as well where the Bowen ratio decreases from a median value of 10 to 8 due to the heat wave. The storage heat flux is larger for urban areas (by $\sim$ 40 W/m^2). It increases even further under HW by upto $\sim$ 50 W/m^2 during midday. While figure 4.14 serves to illustrate the difference between urban/rural and HW/non-HW scenario for each heat flux, figure 4.16 is also presented to demonstrate the partitioning of net radiation into Q_H, Q_E, and Q_S more clearly. These results are consistent with the results reported from the observations towers employed in the Beijing study [70]. The storage flux is associated with SUHI Intensity [89], and the synergistic effect of HWs is attributed to an increase in storage heat flux [69, 89], however, the same was not observed here.

In cases where synergy was not observed as well, lack of moisture in the rural areas is identified as an amplifier of rural temperatures thereby reducing UHI Intensity in HW scenarios [94, 95]. Here as well, the soil moisture in rural areas was the same as that in cities.

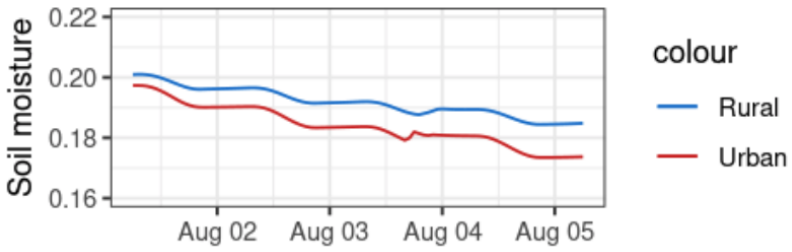

Figure 4.16. Mean soil moisture (m^3/m^3) over urban and rural areas shown for the duration of HW event.

4.2.4 Spatial organization of heat islets

Islet characteristics such as size and intensity distributions, while applicable to any spatial scale of intra-urban heat islets, were not statistically feasible to measure at the resolution of 1 km. As an alternative, the *variance* and 2-D power spectral density of the LST and T2 within domain 3 is evaluated as an indicator of *spatial organization*.

First, the $Var(LST)$ and $Var(T2)$ is calculated for the regions corresponding to urban areas only, where the temperature fields follow a nearly Gaussian distribution. Then, similar to UHI Intensity, the hour-specific variances and the coeffecient of variation (c.o.v., calculated as $Var/Mean$) are estimated, as shown in figure 4.17.

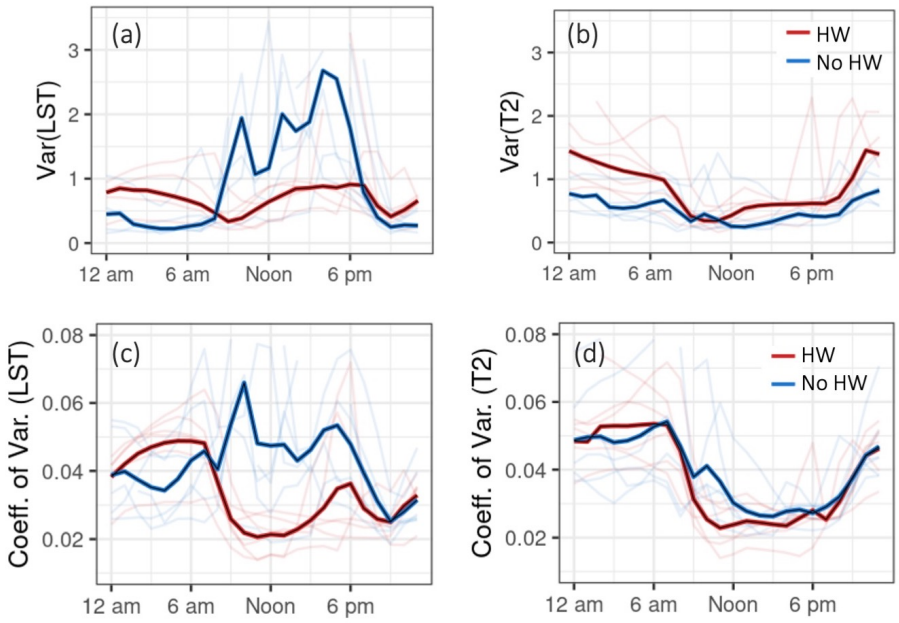

Figure 4.17. Time series of variance of (a) LST and (b) T2 within the urban areas over the period of interest are shown as light-colored lines in the background. Hour-specific averaged LST and T2 variances are overlaid on the respective plots as dark solid lines. Red lines corresponds to HW (2018) and blue corresponds to non-HW scenario (2017). (c,d) Coefficient of variations, calculated as Variance/Mean for LST and T2 respectively are shown in the same format.

First, we find that the variance $Var(LST)$ is higher during the daytime (same as SUHI Intensity) under normal conditions, but it decreases significantly under HW. The same is not observed in $Var(T2)$ plots where the no change in variance is observed. This is particularly evident in the c.o.v. plots as well (Figure 4.17d), where the c.o.v. values show no significant impact of a HW on the net variability of T2. Variance, however, does not offer any information about the size and spacings of the heat islets. For that, I use 2D Power Spectral Density that extracts the information on variance contributed by each of the constituent spatial scales.

Power Spectra analysis

In this section, the 2-D Fast Fourier Transform is used to decomposes the LST and T2 fields (domain 3) into contributions of variance from different spatial wavelengths. The PSD is computed using standard 2D FFT algorithms [96,97]. The resultant PSD is then averaged radially about the center (Figure 4.18a) to yield the 1-D isotropic PSD spectrum, which is plotted on a log-log graph in figure 4.18b. The term isotropic energy x-y spectrum is not to suggest that the field is isotropic but rather that the angular averaging about the center integrates the anisotropy (if any). However, in the PSD of thermal maps, the effect of anisotropy was not significant. The PSD of a fractal surface has a power-law dependence on the spatial frequency of roughness. As a result, the PSD provides utility in that it contains a statistical description of the spatial variabilities, which is largely unaffected by choice of a particular islet size or pixel resolution.

An implementation of the PSD algorithm for fractal surfaces is shown in figure 4.18. Three fractal surfaces representing synthetic temperature maps were generated using three Hurst exponent (H). Originally defined for a time series, H is a measure of long-term auto-correlations within a signal. In the 2-D context, it leverages the autocorrelation function to measure the smoothness of surfaces. As H increases, the spatial scale of variability increases as well (Figure 4.18c). In the context of

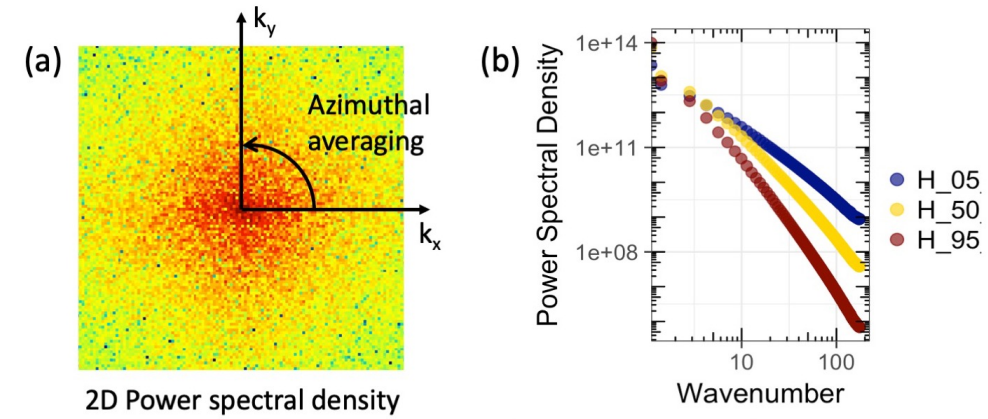

(c)

Fractal Landscape

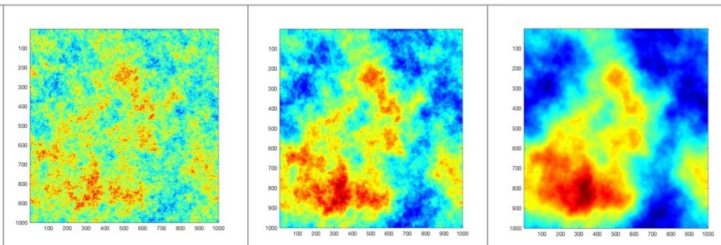

Hurst Exponent	0.05	0.50	0.95
Expected S = -2(H+1)	-2.1	-3	-3.9
Slope from PSD plot	-2.12	-2.99	-3.86

Figure 4.18. (a) 2D PSD map as obtained from the fft algorithm. This values are then radially averaged to obtain a single value corresponding to each wavenumber (b) The radially averaged PSD as a function of wavenumber is illustrated for three different fractal landscapes with different Hurst exponents. (c) Map of the three fractal surfaces, with Hurst exponents 0.05, 0.50, and 0.95 respectively. These were used to validate the PSD algorithm and slope estimation. The table summarizes the validation results.

thermal maps, if high temperatures are aggregated together, it will manifest as a larger wavelength. Alternatively, if high temperatures are dispersed in space, it will manifest as more power in the smaller wavelengths. For each of the three surfaces, the 2-D PSD was calculated and then radially averaged to obtain the 1-D isotropic PSD spectrum (shown in figure 4.18b). We observe that as H increases, the slope of PSD increases as well. The expected slope using the relation: $Slope = -2(H + 1)$, was found to be consistent with the slope measured from PSD plots (4.18c) thereby validating the

algorithm and illustrating the application of PSD slopes as a comprehensive indicator of multi-scale spatial variability.

The radially averaged PSD algorithm is applied to the LST map obtained at every time step (1 hourly) of domain 3, and the diurnal evolution for a single day is shown in figures 4.19a and 4.19b We find that the most notable impact of the HW manifests as an increased variance within the larger wavelengths (corresponding to 32-163 km). The diurnal variability in these spatial scales, which are evident in figure 4.19a, are absent under a HW scenario, indicating large-sized heat islet structure through day and night. On the other hand, the tail of power spectra (corresponding to 1-5 km in figure 4.19b) indicates a systematic diurnal variability, which is similar to its counterpart in 4.19b. These smaller spatial scales correspond to smaller heat islets, which increase during the day time.

This observation was consistent for other HW days as well. A representative PSD plot is shown in figures 4.19c and 4.19d, for nighttime and daytime respectively. For examining the impact during nighttime, the time steps between 9 pm and 7 am for the five days are selected, and the variance corresponding to each wavelength is averaged. The same is repeated for all other time steps corresponding to daytime. We find that the most notable difference manifests in the larger wavelength during the night time, which indicates larger contiguous patches of heat. These spatial scales (54 - 160 km) correspond to the entire width of the city and are therefore corresponding to the SUHI, which would indicate that the SUHI is persistent during nighttime as well during the HW. However, we know from figure 4.12 that this is not the case. Therefore, it shows that the large contiguous patches of heat are not corresponding to the urban vs. rural boundaries. During the daytime, however, the PSD corresponding to city-scale wavelength does not vary due to the HW. This is because the SUHI is significantly dominant during the daytime irrespective of the HW. This finding is also consistent with the SUHI Intensity analysis wherein the impact of HWs was negligible during the daytime (Figure 4.12).

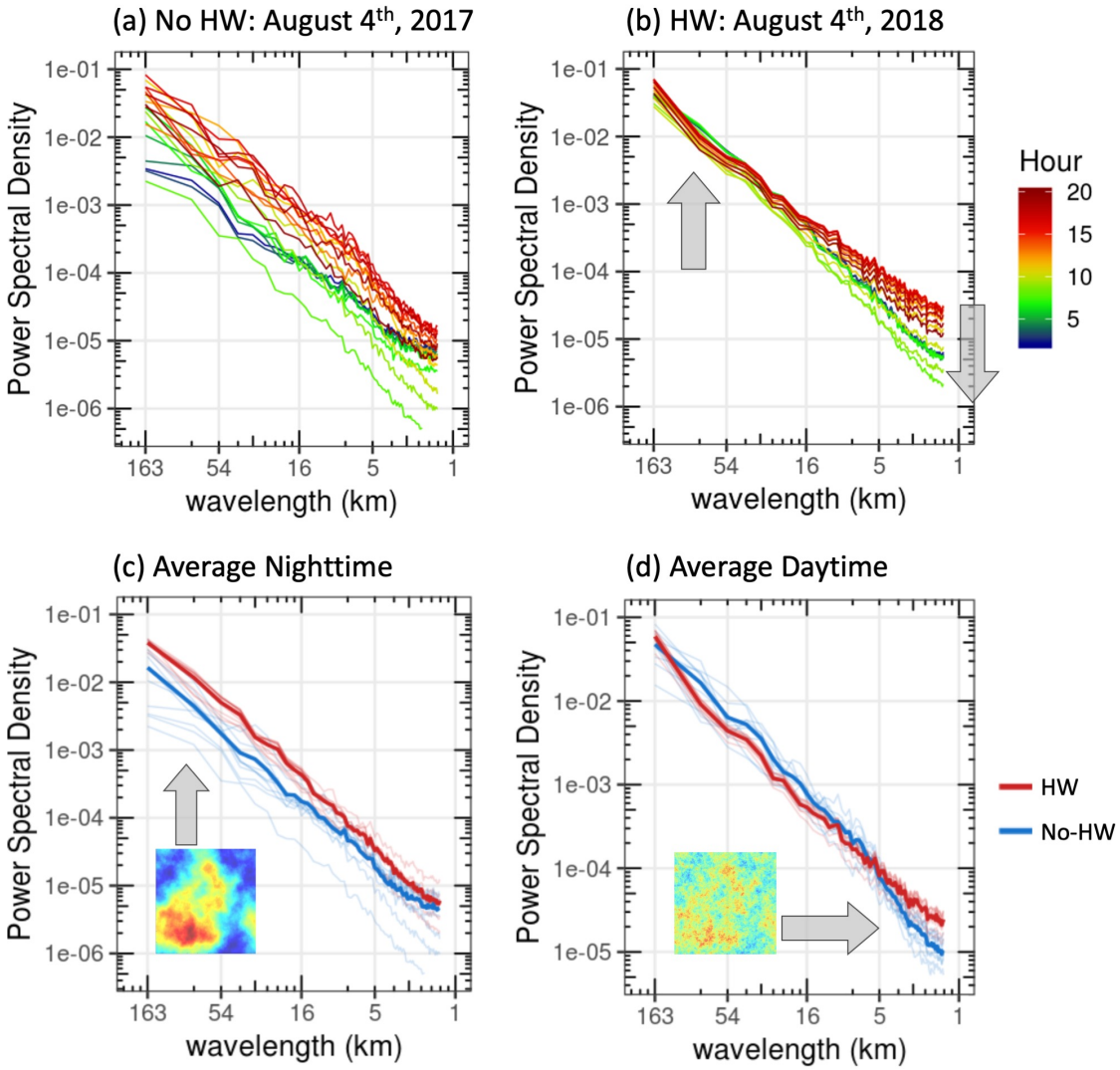

Figure 4.19. Radially averaged 2-D Power Spectral Densities (PSD) of LST fields are shown. PSD for every hour of a single day, August 4th, is shown for (a) non-HW scenario, and (b) a HW scenario. Here, the color bar represents the hour of the day with 0 starting midnight. The PSD value obtained for (c) night time (from 9 pm to 7 am), and (d) daytime (from 8 am to 8 pm) within the period of interest are then averaged by wavelength to obtain the average PSD values for HW (in red) and non-HW (in blue) scenario. The period of interest is shown in figure 4.10

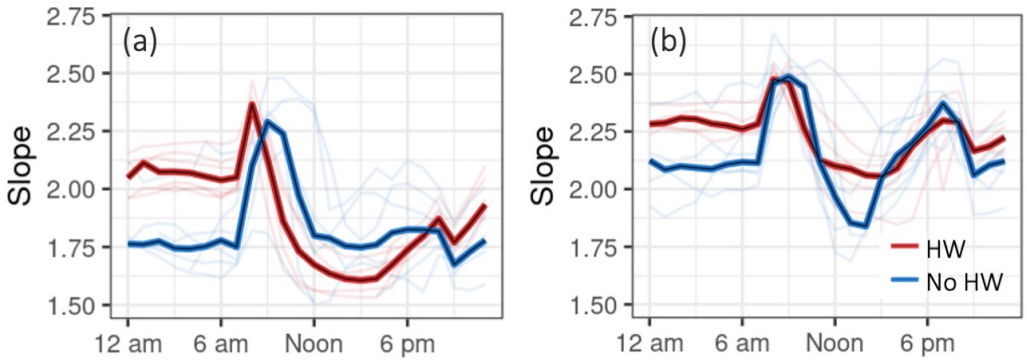

Figure 4.20. PSD slopes of (a) LST and (b) T2 as a function of hour of the day is shown in the light-colored lines for HW (in red) and non-HW (in blue) scenario. Hour-specific average slopes for each time of day overlaid in dark lines.

The PSD analysis of air temperatures revealed higher slopes (ranging from 1.75 to 2.75) than LST (ranging from 1.5 to 2.5), indicating less variance in smaller-scale features. This is because air temperatures tend to be more homogeneous and have smoother gradients due to turbulent mixing, whereas LST can have sharp thermal changes due to sharp changes in LULC and associated emissivity. The diurnal trend, however, is consistent with that of LSTs, where the most dominant impact of HWs is the persistence of large contiguous patches of heat during nighttime. Persistence of contiguous regions of high heat would impede effective thermal dissipation due to increased distance from nearby heat sinks. This could result in an homogeneous expanse of persistent high temperatures, which was observed in the low values of $Var(LST)$ observed during daytime HWs (Figure 4.17).

Lastly, a strong relationship between the PSD slope, SUHI Intensity, and the mean LST (averaged over domain 3) emerges under HW, which is otherwise weaker (Figure 4.21). As mean temperatures increase during the daytime (shown as the color of points), SUHI Intensity increases as well. A negative correlation between PSD slope and SUHI Intensity indicates a shift of variance from larger scales to small scales as the heat island gets more intense.

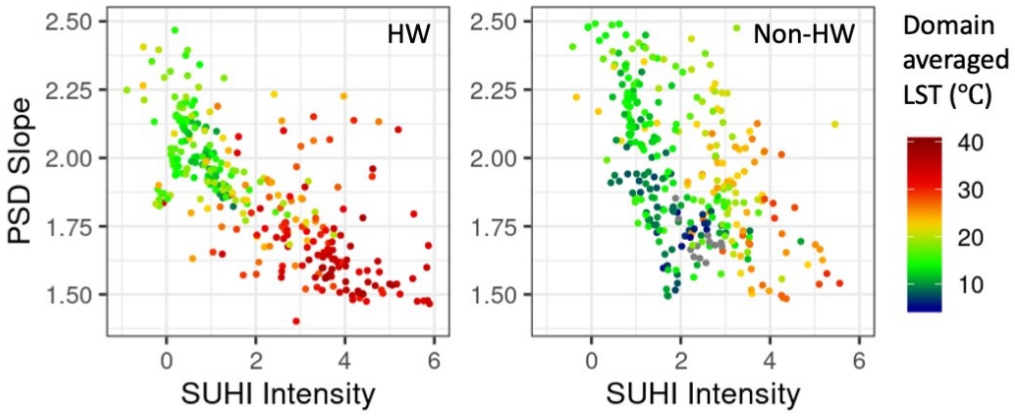

Figure 4.21. Scatter plot betwen the PSD slope and SUHI Intensity is shown for all hours within the HW and non-HW periods of interest respectively. The color indicates mean LST over domain 3.

4.2.5 Diurnal trajectory analysis of UHI metrics

To better understand the correlations between the aforementioned UHI metrics, in this section, I examine their relationship with a focus on their trajectory in time (Figure 4.21). First, I discuss the results based on air temperature under non-HW conditions. The variables' hourly-averaged time series (as shown in figures 4.12, 4.17, and 4.20), is re-illustrated here with a focus on non-HW days. Five key time steps (roughly corresponding to midnight, midday, dawn, and dusk), where a notable change in any of the variable was observed are marked as vertical dashed lines (Figure 4.22). The T2 maps corresponding to the time steps are shown as well. In these plots, a normalized color scheme is chosen such that it varies from $Mean(T2) - 4$ to $Mean(T2) + 4$ for each time step.

In figure 4.22d, the diurnal trajectory of UHI Intensity as a function of mean air temperature is evaluated. First, the scatter plot of UHI Intensity and mean T2 is plotted with the color corresponding to hour of day. Then, for each hour, the average of UHI Intensity and T2 is estimated and the trajectory is shown as an overlaid solid line (Figure 4.22d). During early morning hours, as the sun rises, the rural air

temperatures start rising faster than that of the urban areas. So, although the mean temperature increases, UHI Intensity decreases till it reaches its minima at 1 pm (T2 map shown in figure 4.22g). In the afternoon hours, once the urban air start heating up due to the longwave radiations given off of urban surfaces, the UHI Intensity starts increasing steadily. In the meantime, T2 reaches its peak at about 4 pm and starts declining. As urban and rural T2 continues to decrease through the night, the difference between the two remains large during the night because of the release of urban storage heat flux. Thus, the difference in heat capacity between the urban and rural regions leads to a hysteresis in the response of urban T2, which manifests as an anticlockwise circular trajectory of UHI Intensity as a function of mean T2.

The trajectory of slope as a function of mean T2 has two troughs and crests over the course of the day. Higher values of slope are observed during dawn and dusk and the minima occurs during the midday and midnight. Importantly, there is no monotonic correlation between T2 and slope. For instance, from 1 pm to 7 pm, the change in T2 is negligible compared to the near vertical rise in slope. This rapid increase is akin to the increase in UHI over the same period (cf. Figure 4.22d). Therefore, the slope is more closely related to the change in UHI intensity rather than the absolute value of temperature. Figure 4.22f shows the trajectory of slope as a function of UHI intensity. The slope decreases as the absolute value of UHI intensity increases (either positive or negative). When the UHI is near zero, it implies that the temperatures are homogeneous across the rural-urban boundaries. This manifests as the reduction of small-scale variabilities, in other words, steeper PSD slope. When the urban temperatures deviate from that of the surroundings, the variances manifest at every scale resulting in a decrease of slope. Note that the first crest at dawn corresponds to zero UHI; however, the second crest that occurs at dusk shows a hysteresis and corresponds to a positive UHI value. This reveals a quadratic nature of the relationship between the UHI intensity and the slope. Further research on the consistency of such a pattern for other environmental conditions, and other cities is needed to study the precise relationship.

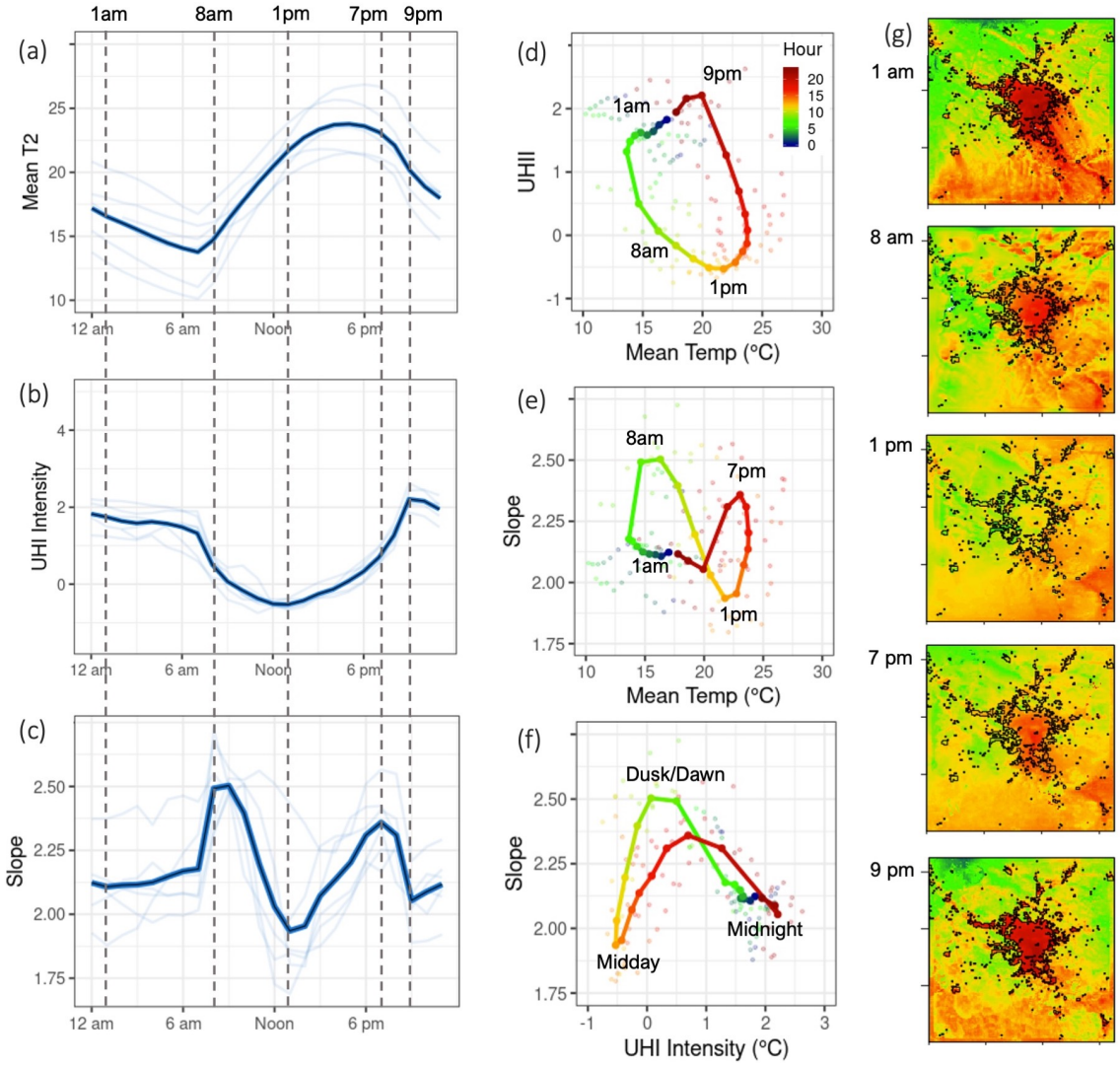

Figure 4.22. (a-c) Hour-specific averaged time series of domain-averaged T2, UHI Intensity, and T2-based PSD slope is shown for the non-HW scenario. Vertical lines corresponding to five times of interest are marked as dashed lines. (d-f) Scatterplot of pairs of metrics (as labelled) are shown for the five non-HW day period (August 3rd, local midnight to August 8th, 2017) as lightly colored dots in the background. The color corresponds to the time of day. Overlaid on top for each is the hour-averaged diurnal trajectory in the phase space of the labelled variables respectively. (g) The T2 map for each of the five times of interest are shown on the right side. The colorscale for each map is adjusted such that a range of $Mean(T2) \pm 4°C$ is maintained for each map.

I now examine the influence of HW on the diurnal trajectory of UHI Intensity, Variance, and slope. In figures 4.23a-f, the diurnal trajectory of the variables under non-HW conditions are shown in a light colors with cross-shaped markers indicating each hour. The same for HW conditions are shown in dark colors with circular markers for each hour. While the anti-clockwise trajectory of UHI Intensity is consistent under a HW, the increased range of T2 results in a larger range of UHI intensity as well. This results in lower UHI Intensity during the night and early morning hours (figure 4.23a). Similarly, the variance of urban air temperatures, $Var(T2)$, also follows a near circular trajectory which expands in range under the HW. However, in this case, the trajectory shifts upwards, yielding higher values during nighttime (figure 4.23b) and nearly the same values during the daytime. Lastly, the double-peaked slope trajectory of slope is not increased by the HW. Only the nighttime hours experience a higher value of slope (figure 4.23c).

The trajectory of SUHI Intensity as well maintains the same diurnal pattern, but increases in range due to lower night time temperatures (figure 4.23d). $Var(LST)$ shows an overall positive correlation with mean LST with a slight hysteresis as the temperatures decrease through the late afternoon and night. The the afternoon temperatures are higher, the $Var(LST)$ flattens and the peak $Var(LST)$ reduces (figure 4.23e). In case of slope trajectory, the range increases and the otherwise circular trajectory becomes more elongated with a strong negative correlation (figure 4.23f). The diurnal behavior of LST-based metrics is discussed in details with the help of figure 4.24.

Consistent with the template of figure 4.22, the time series and diurnal trajectories of SUHI Intensity, Var(LST), and LST-based PSD-slope are presented along with a panel of LST maps corresponding to each hour of interest (Figure 4.24). To enable a visual comparison of LST across different timesteps, a normalized color scheme is chosen such that it varies from $Mean(T2) - 8$ to $Mean(T2) + 8$ for each time step (Figure 4.24g). Unlike UHI, the SUHI does not have a delayed response to solar radiation (Figure 4.11). As a result, SUHI Intensity is more positively correlated

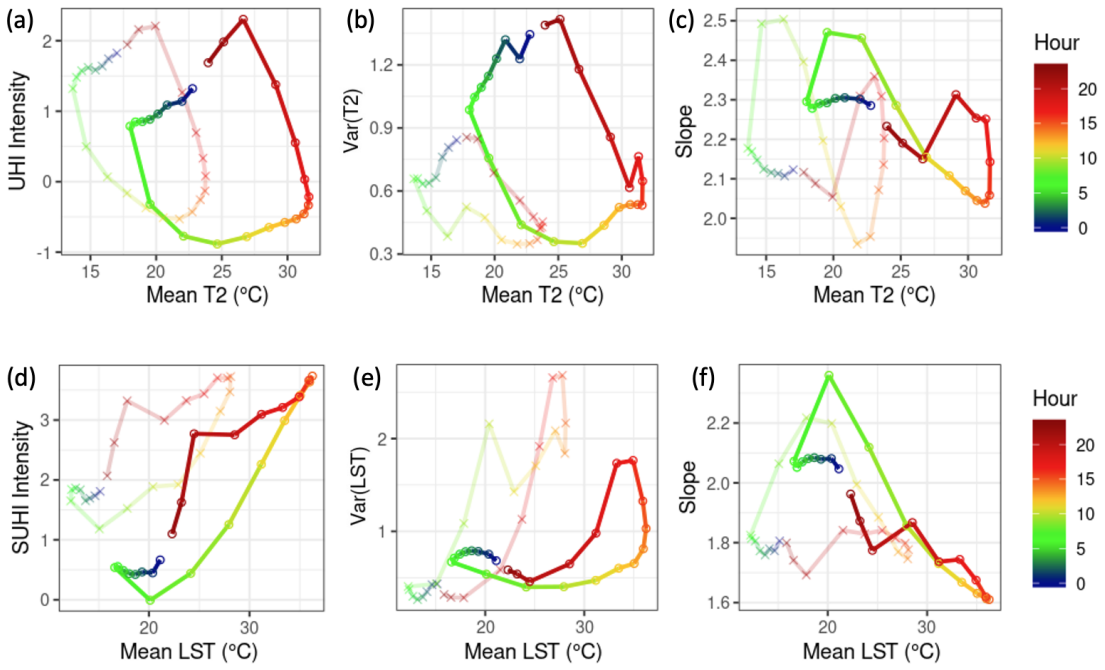

Figure 4.23. The hourly-specific diurnal trajectory is shown within the phase space of (a) UHI Intensity, (b) Var(T2), and (c) T2-based PSD slope as a function of mean rural T2, as well as (d) SUHI Intensity, (e) Var(LST), (f) LST-based PSD slope as a function of mean rural LST. A typical non-HW day is shown in light-colored lines with cross-markers, and a HW day is shown in darkly colored lined with circle markers. The colors correspond to the hour of day.

with mean LST (Figure 4.24d). As the sun rises, mean LST immediately increases steeply; however, the SUHI intensity first decreases for about an hour before rising later. This subtle offset in behavior between the urban and rural areas result in a similar anti-clockwise trajectory despite the notable positive correlation.

The trajectory of PSD-slope as a function of LST shows a consistent negative correlation, with the minima of slope corresponding to the late afternoon hours when the mean LST is highest (Figure 4.24e). In the case of LST as well, the diurnal pattern of slope is more closely linked to the SUHI Intensity than the mean LST, as is highlighted the sharp peak in slope occurring at 8 am corresponding to the

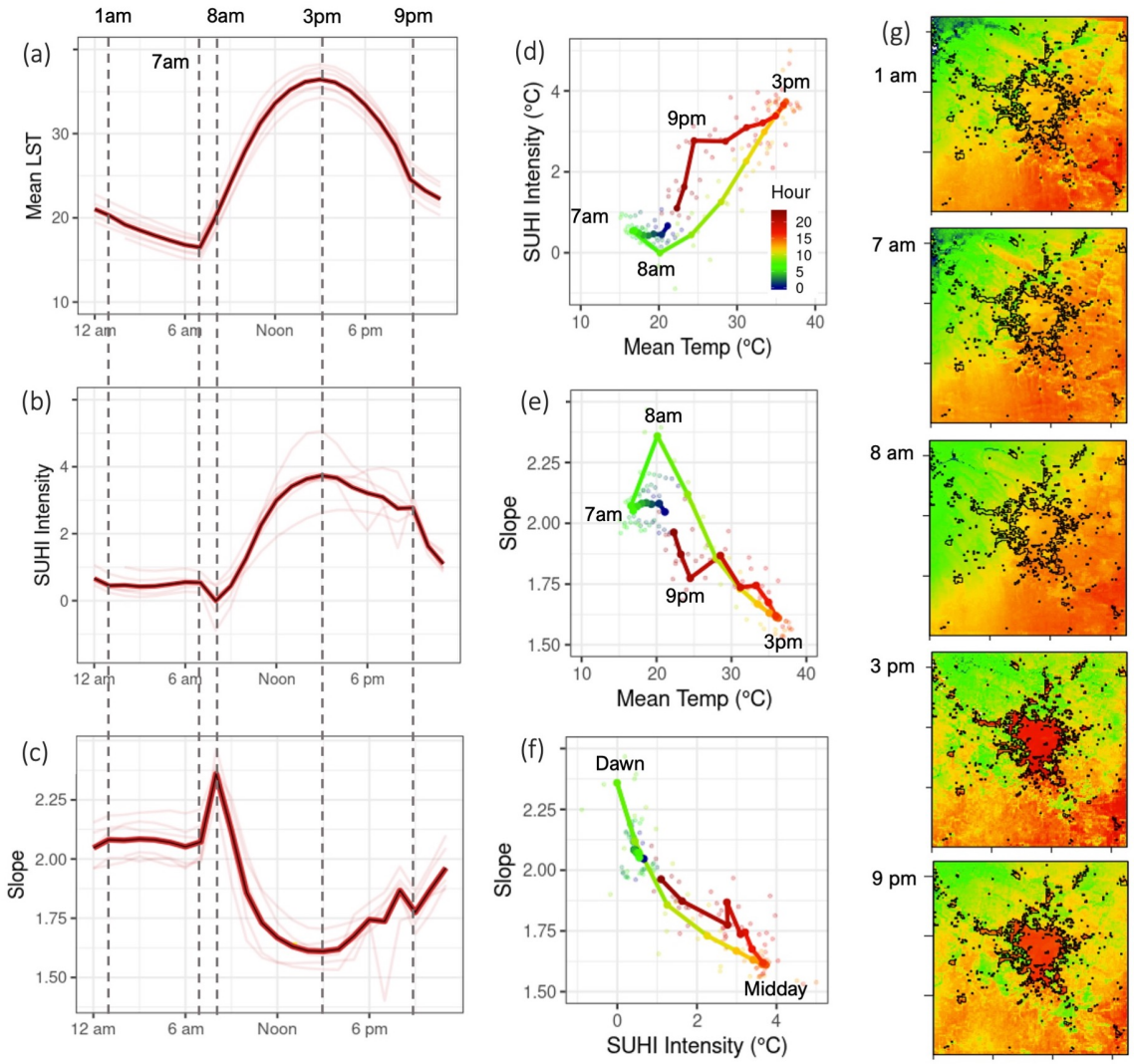

Figure 4.24. (a-c) Hour-specific averaged time series of domain-averaged LST, SUHI Intensity, and LST-based PSD slope is shown for the HW scenario. Vertical lines corresponding to five times of interest are marked as dashed lines. (d-f) Scatterplot of pairs of metrics (as labelled) are shown for the five HW day period (August 3rd, local midnight to August 8th, 2018) as lightly colored dots in the background. The color corresponds to the time of day. Overlaid on top for each is the hour-specific trajectory of a typical day in the phase space of these variables. (g) The LST map for each of the five times of interest are shown on the right side. The color-scale for each map is adjusted such that a range of $Mean(LST) \pm 8°C$ is maintained for each map.

minima in SUHI Intensity. As a result, the more interesting pattern emerges from the analysis of slope vs SUHI Intensity (Figure 4.24f). Consistent with the pattern in figure 4.22f, the minima of slope occurs when the absolute value of SUHI Intensity is the largest. Since, there are no negative values of SUHI Intensity, this manifests as a monotonous negative correlation, wherein the maximum slope value occurs near zero SUHI Intensity. This is again because near zero values of SUHI Intensity implies that the temperatures are homogeneous across the rural-urban boundaries. This reduction of small-scale variabilities manifests as a steeper PSD slope. As SUHI Intensity increases, the variances show up at every scale thereby lowering the PSD slope. Thus, the hourly trajectory plots for pairs of these three variables present a novel perspective that complements the time series analysis.

4.2.6 Comparison with other cities

The 2018 heatwave impacted several other European cities as well (Figure 4.25). The data from domain 2 is used to compare the response of diverse cities to the same heatwave. Six of the largest urban agglomeration, including Paris, are selected for further analysis. The spatial resolution of LST and T2 maps is 3 km (Domain 2), which did not leave adequate spatial data for computing the Power Spectral Density. Therefore, only mean UHI Intensity and the intra-urban variance for both LST and T2 are computed. To maintain consistency across the cities, the aforementioned metrics are recalculated for Paris at a 3 km resolution as well. Due to the coarser resolution, some inconsistencies are observed between the results obtained from Domain 3 dataset and the results shown here.

The six urban regions were obtained by identifying all contiguous urban patches that are above 100 pixels ($\sim 900km^2$) using the MODIS land use map (Figure 4.25a). As a result, other than the two mega-cities of Paris and London, agglomerations of nearby smaller cities were identified. For example, all the urban settlements in and around Rotterdam and The Hague were grouped into a single urban polygon.

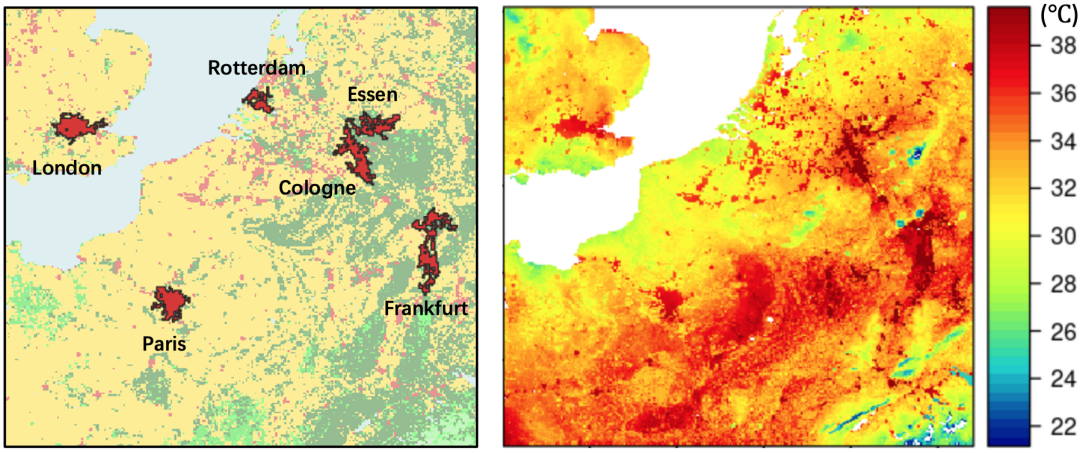

Figure 4.25. (a) Land Use Land Cover map of Europe (Extent: Domain 2). Six contiguous urban regions (area > 900 km^2) are identified and shown in red. Each urban agglomeration includes a main city and its neighboring towns. (b) LST map of the same as on August 4^{th}, 2018 afternoon.

Similarly, three distinct agglomerations of German cities were identified as well which are named after their largest city. For each of the cities, the surrounding of the urban polygon excluding water bodies was taken to estimate the rural background temperature.

The analysis of UHI Intensities and intra-urban variance for other urban areas shows results consistent with that of Paris (Figure 4.26). Both UHI and SUHI Intensities were mostly unaltered by the HW during the daytime. The SUHI Intensity for the coastal cities, Rotterdam and London, were an exception to this trend. Unlike the inland cities, the diurnal pattern of SUHI Intensity under non-heat wave scenario (shown in blue in Figures 4.26d and 4.26f) for these coastal cities do not conform to a range of 4°C. This could be an impact of proximity to the oceans. However, the same impact of sea breeze in not evident in UHI Intensities (Figures 4.26i and 4.26l). During nighttime, a reduction of nearly 1°C was observed for all cases except London. This serves to show that despite the difference in rural backgrounds of Paris (which

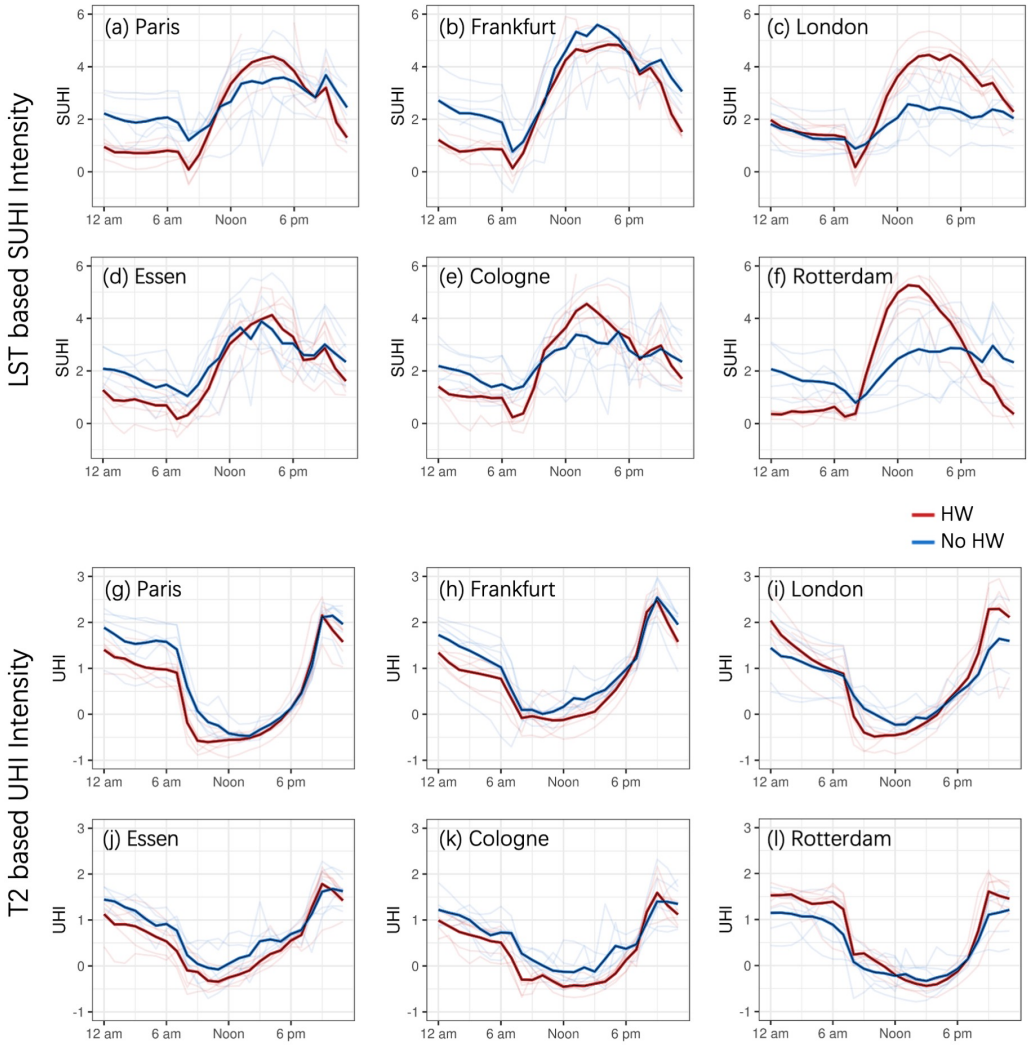

Figure 4.26. Time series of (a-f) SUHI Intensity and (g-l) UHI Intensity is shown for six urban agglomerations. The data for individual days is shown as lightly colored lines in the background and hour-specific averaged SUHI and UHI Intensities are overlaid on the respective plots as dark solid lines. Red lines corresponds to HW (2018) and blue corresponds to non-HW scenario (2017). The LST and T2 datasets are obtained from Domain 2 of the WRF simulation at a resolution of 3 km.

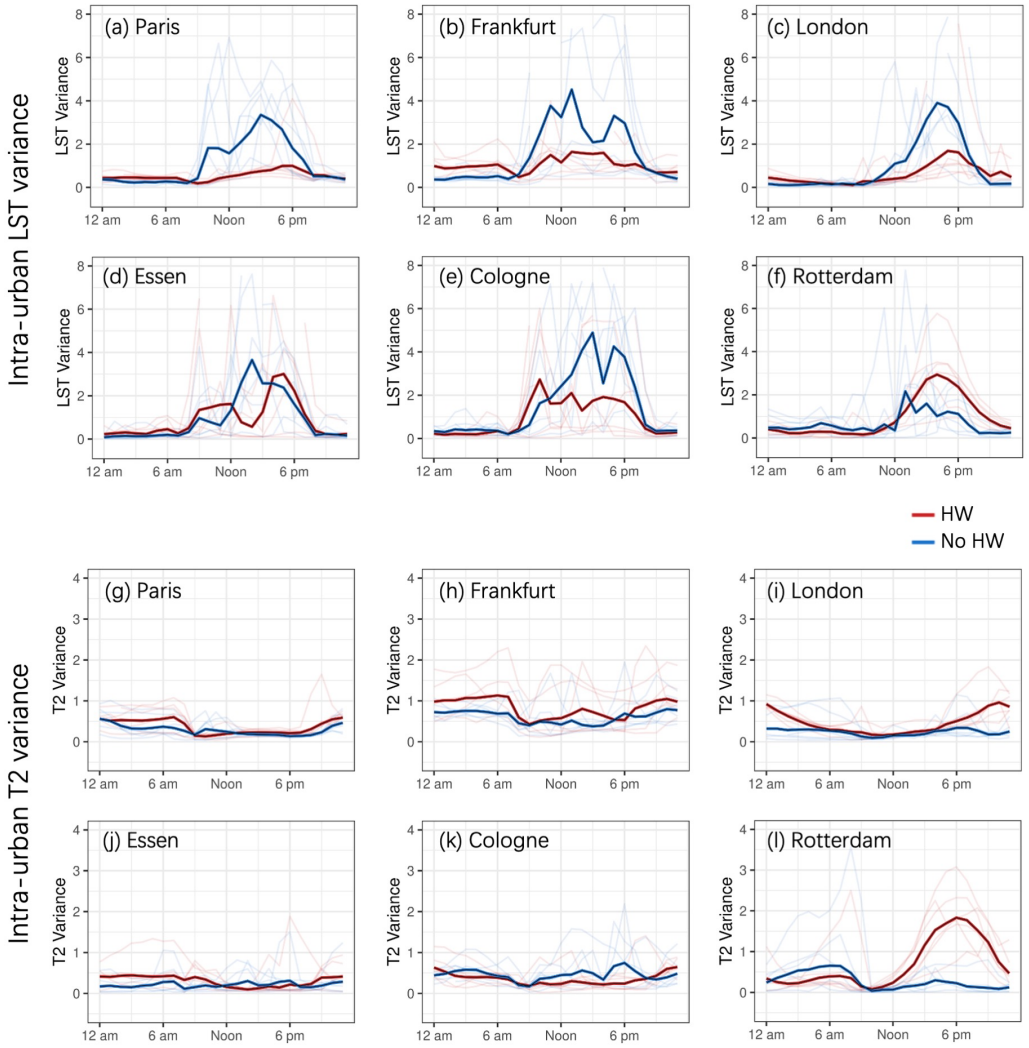

Figure 4.27. Time series of variance of (a) LST and (b) T2 within each of the urban agglomerations as labelled are shown as light-colored lines in the background. Hour-specific averaged LST and T2 variances are overlaid on the respective plots as dark solid lines. Red lines corresponds to HW (2018) and blue corresponds to non-HW scenario (2017). The LST and T2 datasets are obtained from Domain 2 of the WRF simulation at a resolution of 3 km.

is 90% croplands) and the German cities (which are closer to forests), no synergistic influence of HW was observed.

The intra-urban variance analysis shows that the heatwave reduced $Var(LST)$ and homogenized the urban surface temperatures for all cities, except Rotterdam (Figure 4.27a-f). This is because the Rotterdam-Hague urban agglomeration has a considerable portion of urban regions sharing the perimeter with the ocean. The lower coastal temperatures contribute greatly to both $Var(LST)$ and $Var(T2)$ (Figures 4.27d and 4.27f). For other cities, $Var(T2)$ is unaltered by the HW and any difference in $Var(T2)$ is lower than the standard deviation of normal $Var(T2)$ values by the hour. Note that $Var(T2)$ plot of Paris is different than the same estimated from domain 3 (figure 4.17) because of the coarser resolution of domain 2. This limitation should be kept in mind while analyzing the results of other cities as well.

4.3 Summary

The UHI is driven by two main types of drivers, those pertaining to urban form and those that describe synoptic atmospheric conditions. In this chapter, I focus on their impact on the intra-urban heat islets. As a proxy for urban form, the spatial organization of heat islets, characterized by Λ_{score}, was used. Analysis of heat islet size distributions (Figure 4.2) demonstrate the emergence of two classes where the compact configurations result in a power law distribution, and the sprawling cities show an exponential tempering of power law tail. In contrast, the analysis of heat islet intensity distributions (Figure 4.4) indicates that while a sprawling configuration is favorable for reducing the mean SUHI Intensity of a city, for the same mean, it also results in higher local thermal extremes. This poses as a trade-off for urban designers in adopting expansion or densification as a growth trajectory to mitigate urban heat at both the neighborhood and the city scale.

As an external forcing to the heat islet system, the impact of HW were studied. The results show that the mean SUHI (and UHI) Intensity reduced by nearly 1°C

under the HW during nighttime and remained unchanged during daytime. The analysis of variance within heat islets using PSD indicated that large contiguous heat islets (city-scale) persist throughout the day during a HW, which would disappear during nighttime under normal conditions. On the other hand, the smaller islets (neighborhood-scale) display the same diurnal patterns as the non-HW conditions wherein they arise during daytime and dissipate during nighttime. Lastly, correlation between SUHI Intensity and PSD slope highlight that the variances at every scale contribute to the overall difference between urban and rural temperatures. From a mitigation point of view, this presents as a wicked problem analogous to the paradox of adopting either expansion or densification. It is not within the scope of this thesis to offer an immediate solution to the urban planners on what is the best pathway to mitigate multi-scale UHI or the exacerbated impact of HW on them. Rather, this serves as a template to quantify and assess the heterogeneity of urban heat and evaluate the trade-offs between alleviating local vs. city-wide thermal extremes.

5. CONCLUDING REMARKS

"Since all models are wrong, the scientist must be alert to what is importantly wrong. It is inappropriate to be concerned about mice when there are tigers abroad."

– George E. P. Box

Cities are the apex examples of a complex, coupled, socio-technological systems, which present multiple challenges as urbanization rapidly intensifies across the world [98]. The UHI is one such problem. The view of UHI as a fractal system is novel in that clusters of high temperatures are shown to be statistically self-similar for the first time. However, within the field of quantitative geography, cities and several of their properties are already known to be fractal [73].

Fractals are the most energy-efficient organizations for several applications. For example, river networks are fractal because it is the best pathway to optimize energy while flowing towards lower potential energy. In the same way, engineered transportation networks such as sewage and road networks also evolve over time to become fractals when they are optimized for efficiency [25, 55]. In their book chapter 'form follows function' in Fractal Cities, Batty and Longley explain that urban *functions* grow in time while constantly optimizing the *form* to result in a fractal [22]. Examples include metabolic functions of cities, such as population distribution, traffic flow, human mobility, and energy use [27–29]. As UHI is a by-product of urban form and functions, they follow similar spatial patterns as well [86]. However, an important distinction is that the city does *not* grow to optimize 'urban heat' per se. Therefore, a fractal UHI structure is not necessarily the optimal design to minimize urban heat. More importantly, the same fractal generative mechanism can yield a diverse spatial organization of heat islets. This was shown by a range of different Lacunarity val-

ues attained by heat islet systems with the same aggregated area-perimeter fractal dimension ($D \sim 4/3$). In a quest to find the most optimal spatial structure of UHI, we defined heat islet size and intensity distribution as an indicator and found that sprawling spatial organizations had its merits in that they reduce the sizes of heat islets, but at the same time, these islets tend to attain higher than mean temperatures. Therefore, a balance needs to be kept between the expansion and densification of cities to counter extreme heat.

The framework of using incremental thresholds to identify connected clusters and study their dynamics as a function of the threshold was adapted from percolation theory [37] and can be used to describe any fractal landscape. This is analogous to using the water levels, flooding a heterogeneous landscape to study the archipelago of islands. Alternatively, we may invert the clustering technique to identify potential lakes and wetlands below the water level. Interestingly, the area-perimeter fractal dimensions for islands [40], lakes [41], wetlands [47], and even clouds [99] are reported as $D \sim 4/3$ as well.

In the context of heat, the work can be extended beyond the city to regional thermal landscapes. As we know that atmospheric thermal patterns, as well as the natural topography, is fractal as well, regional-scale thermal landscapes are also expected to exhibit self-similarity. The scaling laws might differ from the intra-urban heat islets, given the higher heterogeneity of the urban areas. However, their comparison can extend this work to larger regional scale domains. A limitation of analyzing thermal maps is that it only represents the instantaneous result of dynamic heat sources and sinks. If we assume homogeneous heat capacities and thermal conductivity, this will correspond to the *structural* heterogeneity of heat sources and sinks, wherein the sizes of heat islets indicate the strength of the sources and the Lacunarity of spacings indicate the sink strengths. Consideration of the *functional* heterogeneity will require that we incorporate the heterogeneity within heat capacity and thermal conductivities as well. For that, instead of LST, a spatial map of heat fluxes can be input as the DEM within this framework.

For exposure assessment of urban communities to heat, however, analysis of surface temperatures itself is not enough. What people living in the cities experience as *heat stress* is computed using a combination of air temperature as well as humidity [63]. Exposure to heat stress can affect an individual's ability to regulate his body temperature, resulting in increased rates of heat stress, heatstroke, and premature death [100]. However, different individuals have different susceptibilities for heat stress, and the characterization of exposure alone is not sufficient. Populations at risk from extreme heat may share several characteristics, called vulnerability factors, such as old age, low educational attainment, high poverty levels, poor health, and lack of air conditioning, which can be unified into a vulnerability index through statistical methods [66, 67]. As a result, vulnerability is a function of both the thermal conditions of a region and the exposure and susceptibility of the individuals who are subjected to it. In order to characterize the spatially variable vulnerability, a joint probability of heat stress, as well as the population's susceptibility, should be considered. Furthermore, similar to the vulnerability of humans, other urban infrastructure systems can be affected by extreme heat as well. For instance, consider the power grid network. When the temperature soars in a city, people respond by maximizing the use of their respective air-conditioning. For critical heat islets, the collective overload on the power grid system can result in a cascading failure. As a result, the design of power supply networks cognizant of the critical regions could help prevent such failures as well as optimizing costs.

Lastly, the limitations of scientific models and observations should be kept in mind. The Land Surface Temperatures viewed by satellites such as Landsat are, after all, an estimate. Satellites preferentially see horizontally unobstructed surfaces (such as roofs, open areas). They also combine substantial surface temperature variability caused by building plan area, building height to width ratio, construction materials and albedos, impervious and vegetated fractions, and moisture status, etc., that play a role in determining the LST distribution within the spatial scale of a pixel ($\sim$ 90 m). While there are correlations between LST and air temperature (Figure 4.11),

the findings based on LST should not directly be extended to the thermal comfort of occupants. For instance, consider a dense layout of high-rise buildings like Manhattan (all with hot roofs) might lead to a hotter remotely sensed LST, but the narrow the street canyons shaded by them might result in a cooler environment for pedestrians. The same caveats apply to WRF models as well, where not only the heterogeneity within a grid cell is lost, but several other approximations and assumptions (Appendix E) could lead to cascading errors. This is especially true for studying intra-urban environments using WRF as the urban LULC characterization often does not reflect the city accurately. Despite these mice and tigers, this work presents a step towards the multi-scale characterization of the complex intra-urban thermal landscape, and I hope that it opens new vistas for future investigations.

A. APPENDIX A: LOCAL CLIMATE ZONES

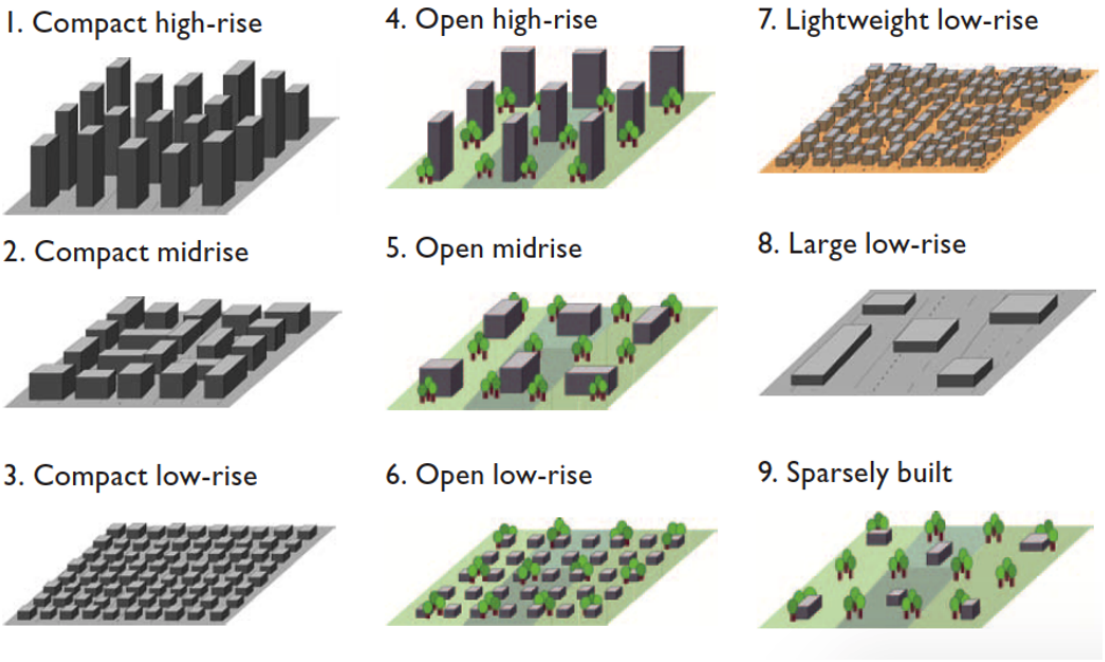

Figure A.1. Schematic diagram for nine diverse types of Local Climate Zones are shown to illustrate the different forms urban neighborhoods can take. Please refer to `http://www.wudapt.org/` for further details. Source: Stewart and oke (2012)

B. APPENDIX B: LIST OF CITIES

Table B.1.: List of cities, their location, climate type, and the Landsat image used

City	Climate	Longitude	Latitude	Landsat image timestamp
Accra	bsh	-0.19	5.60	(2017-04-15 10:15:09)
Adelaide	csa	138.60	-34.93	(2016-12-24 00:33:47)
Amsterdam	cfb	4.90	52.37	(2017-05-27 10:39:11)
Astana	dfb	71.47	51.16	(2015-06-03 06:07:15)
Atlanta	cfa	-84.39	33.75	(2014-05-06 16:12:23)
Austin	cfa	-97.74	30.27	(2016-05-03 17:02:37)
Bangkok	aw	100.50	13.76	(2015-02-05 03:37:41)
Barcelona	csa	2.17	41.39	(2017-06-14 10:30:09)
Basel	cfb	7.59	47.56	(2014-07-17 10:22:33)
Beijing	dfa	116.41	39.90	(2017-05-07 02:52:50)
Berlin	dfb	13.40	52.52	(2017-06-02 10:02:10)
Bern	cfb	7.45	46.95	(2014-07-17 10:22:33)
Birmingham	cfb	-86.80	33.52	(2015-04-09 10:57:56)
Bogota	cfb	-74.07	4.71	(2015-02-21 15:12:33)
Boston	cfa	-71.06	42.36	(2016-04-24 15:26:37)
Brasilia	aw	-47.88	-15.79	(2016-05-02 13:14:21)
Bucharest	cfa	26.10	44.43	(2015-08-03 08:56:34)
BuenosAires	cfa	-58.38	-34.60	(2014-12-19 13:44:45)
Busan	cfa	129.08	35.18	(2016-04-19 01:59:02)
Chengdu	cwa	104.07	30.57	(2017-05-01 03:32:40)
Chennai	aw	80.27	13.08	(2016-04-23 04:58:01)

Chicago	dfa	-87.63	41.88	(2014-09-23 16:35:10)
Colombo	af	79.86	6.93	(2017-01-13 04:54:05)
Copenhagen	cfb	12.57	55.68	(2016-05-12 10:13:38)
Curitiba	cfb	-49.27	-25.42	(2016-06-12 13:11:01)
Delhi	bsh	77.21	28.61	(2017-03-05 05:18:40)
Denver	cfa	-104.99	39.74	(2013-09-26 17:39:09)
Dusseldorf	csb	6.77	51.23	(2013-07-21 10:29:37)
Frankfurt	cfb	8.68	50.11	(2015-04-24 10:15:02)
Guangzhou	cfa	113.26	23.13	(2016-02-07 02:52:07)
Guatemala	cwb	-90.23	15.78	(2016-01-27 16:24:11)
Hanoi	cwa	105.83	21.03	(2017-06-04 03:23:02)
HoChiMinh	aw	106.63	10.82	(2014-09-18 03:14:22)
Houston	cfa	-95.37	29.76	(2017-04-06 16:50:10)
Indianapolis	dfa	-86.16	39.77	(2013-10-08 16:25:01)
Istanbul	csa	28.98	41.01	(2013-07-30 08:47:23)
Jakarta	am	106.87	-6.18	(2014-09-13 03:00:14)
Kiev	dfb	30.52	50.45	(2016-07-13 08:49:07)
Kolkata	aw	88.36	22.57	(2014-04-22 04:30:53)
KualaLumpur	af	101.69	3.14	(2014-04-25 03:28:26)
Lagos	aw	3.38	6.52	(2013-12-18 10:04:25)
Lisbon	csa	-9.14	38.72	(2016-07-14 11:14:27)
London	cfb	-0.13	51.51	(2017-06-10 10:52:04)
LosAngeles	csa	-118.24	34.05	(2014-06-01 18:27:56)
Manila	aw	120.98	14.60	(2016-02-13 02:17:23)
Miami	aw	-80.19	25.76	(2014-10-17 15:50:16)
Milan	cfa	9.19	45.46	(2014-06-10 10:04:37)
Montreal	dfb	-73.57	45.50	(2016-06-16 15:44:09)
Moscow	dfb	37.62	55.76	(2016-07-24 08:29:03)
Nairobi	cfb	36.82	-1.29	(2013-06-08 07:45:12)

Nanjing	cfa	118.80	32.06	(2013-04-07 02:39:14)
NewOrleans	cfa	-90.07	29.95	(2014-04-09 16:32:12)
NewYork	dfa	-74.01	40.71	(2016-04-15 15:33:16)
Orlando	cfa	-81.38	28.54	(2017-04-07 15:54:56)
Osaka	cfa	135.50	34.69	(2016-03-22 01:34:32)
Oslo	dfb	10.75	59.91	(2013-07-12 10:33:27)
Paris	cfb	2.35	48.86	(2017-04-09 10:40:20)
Perth	csa	115.86	-31.95	(2017-04-24 02:04:49)
Philadelphia	dfa	-75.17	39.95	(2017-07-30 15:39:49)
Portland	csb	-122.68	45.52	(2015-06-07 18:55:15)
Prague	cfb	14.44	50.08	(2017-05-19 09:50:28)
RioDeJaneiro	am	-43.17	-22.91	(2015-09-25 12:51:59)
Rotterdam	cfb	4.48	51.92	(2017-04-09 10:39:32)
SanJose	csb	-121.89	37.34	(2013-04-09 18:46:34)
Seattle	csb	-122.33	47.61	(2015-06-23 18:54:58)
Seoul	dfa	126.98	37.57	(2016-05-19 02:10:38)
Shanghai	cfa	121.47	31.23	(2016-02-27 02:24:54)
Stockholm	cfb	18.07	59.33	(2013-07-09 10:02:33)
StPetersburg	dfb	30.34	59.93	(2014-04-24 09:04:48)
Sydney	cfa	151.21	-33.87	(2013-09-18 23:46:03)
Tbilisi	cfa	44.83	41.72	(2017-07-03 07:43:22)
Tokyo	cfa	139.69	35.69	(2013-09-17 01:17:47)
Toulouse	cfb	1.44	43.60	(2016-08-12 10:42:27)
Vancouver	csb	-123.12	49.28	(2017-07-05 19:01:13)
Warsaw	dfb	21.01	52.23	(2015-04-23 09:31:23)
WashingtonDC	cfa	-77.04	38.91	(2016-04-13 15:46:02)
Wuhan	cfa	114.31	30.59	(2015-10-25 02:56:23)

C. APPENDIX C: LAND SURFACE TEMPERATURE ALGORITHM

Until recently, studies of urban effects on meteorology and climate have been conducted for isolated locations and with in-situ measurements. With the advent of high-resolution Earth-monitoring satellites, it has become possible to study these effects both remotely and on continental or global scales [9]. Here, we use LST derived from Landsat thermal bands for the analysis. The algorithm employed for the computation of LST here doesn't account of atmospheric correction. However, a systematic error throughout the Landsat scene is acceptable in this particular study because the absolute temperatures are not of interest, but the relative temperatures matter. The algorithm used as well as the R-code written for LST is outlined below.

Step 1: TOA radiance

$$L_\lambda = M_L \cdot Q_{cal} + A_L \tag{C.1}$$

where,

L_λ = TOA spectral radiance ($W/m^2 * srad * \mu m$)

M_L = Band-specific multiplicative rescaling factor from the metadata (RADIANCE_MULT_BAND_x, where x is the band number)

A_L = Band-specific additive rescaling factor from the metadata (RADIANCE_ADD_BAND_x, where x is the band number)

Q_{cal} = Quantized and calibrated standard product pixel values (DN)

Step 2: TOA Brightness Temperature

$$T = \frac{K_2}{ln(\frac{K_1}{L_\lambda} + 1)} \tag{C.2}$$

where,

T = At-satellite brightness temperature (K)

L_λ = TOA spectral radiance ($W/m^2 * srad * \mu m$)

K_1 = Band-specific thermal conversion constant from the metadata
(K1_CONSTANT_BAND_x, where x is the thermal band number)

K_2 = Band-specific thermal conversion constant from the metadata
(K2_CONSTANT_BAND_x, where x is the thermal band number)

The band specific values were obtained from the metadata file. These equations are used for both band 10 and 11, to obtain the temperatures. However, to obtain the actual ground surface temperature, the emissivity needs to be calculated. The codes implemented in R here were derived and modified from ArcGIS toolbox [52].

Step 3: Proportion of vegetation (P_v) and Emmissivity (e) is estimated from NDVI to estimate actual LST:

$$P_v = \frac{NDVI - NDVI_{min}}{(NDVI_{max} - NDVI_{min})^2} \tag{C.3}$$

$$e = 0.004 * P_v + 0.986 \tag{C.4}$$

$$LST = \frac{T}{1 + w * \frac{T}{\rho} * ln(e)} \tag{C.5}$$

where,

T = At satellite brightness temperature (K) as per equation C.4

w = Wavelength of emitted radiation (11.5 μm)

$\rho = h \times \frac{c}{\sigma} = 14380\, \mu mK$

(σ = Boltzmann constant = $1.38 \times 10^{-23}\, \frac{J}{K}$, h = Planck's constant = $6.626 \times 10^{-34}\, Js$,
c = velocity of light = $2.998 \times 10^8\, \frac{m}{s}$)

e = emissivity as per equation C.4

(Source: `https://landsat.usgs.gov/using-usgs-landsat-8-product`)

D. APPENDIX D: FITTING PROBABILITY DISTRIBUTIONS

For fitting probability distributions to the cluster size distribution, a combination of maximum-likelihood fitting methods with goodness-of-fit tests based on the Kolmogorov-Smirnov (KS) statistic and likelihood ratios were used [53]. A step-by-step methodology as summarized in Box 1 of the paper (as outlined below) was followed with the help of R-code provided by Laurent Dubroca and Cosma Shalizi on Clauset's website [1]. Following their R-code for the analysis of power-law distributions the steps are as follows:

1. Estimate the parameters x_{min} and α of the power-law model.

2. Calculate the goodness-of-fit between the data and the power law. If the resulting $p - value \geq 0.1$, the power law is a plausible hypothesis for the data, otherwise it is rejected.

3. Compare the power law with alternative hypotheses via a likelihood ratio test. For each alternative, if the calculated likelihood ratio is significantly different from zero, then its sign indicates whether or not the alternative is favored over the power-law model.

The data was tested for a power law tail fit and compared against 4 other competing distributions - Exponential, Lognormal, Stretched Exponential (Weibull), and Power law with exponential rate of tempering. The equations are given below (adapted from Clauset, et al. 2009) [53].

The basic idea behind the likelihood ratio test is to compute the likelihood of the data under two competing distributions. The one with the higher likelihood is then

[1] `http://tuvalu.santafe.edu/~aaronc/powerlaws/`

the better fit. Alternatively, one can calculate the ratio of the two likelihoods, or equivalently the logarithm R of the ratio, which is positive or negative depending on which distribution is better, or zero in the event of a tie. Furthermore, the p-value for the Log-likelihood Ratio is checked and an outcome is selected only if the p-value < 0.1 (For a 90% confidence).

The cluster size distributions for all cities were tested at several thermal thresholds based on the following percentiles: 50^{th}, 60^{th}, 70^{th}, 80^{th}, and 90^{th}. All of the distributions were found to qualify as a power law tail (with a p-value of 0.1, i.e. 90% confidence) for lower percentile thresholds. The lower cut-off for power law was found to be under 500 m for most cities (95% CI one-sided), this roughly corresponds to the size of an urban block implying that the scaling doesn't extend to the length scales smaller than an urban block. At 90^{th} percentile threshold, we find that 25 of the 78 cities were described as a power-law with exponential tempering: $P(A > a) \propto a^{1-\beta} e^{-c \cdot a}$. However, none of them have likelihoods suggesting a Weibull, exponential, or lognormal describe the data better. The table with complete results is attached as separate excel sheet.

	Name	Distribution $p(x) = Cf(x)$ $f(x)$	C
Continuous	Power law	$x^{-\alpha}$	$(\alpha-1)x_{\min}^{\alpha-1}$
	Power law with cutoff	$x^{-\alpha}\mathrm{e}^{-\lambda x}$	$\frac{\lambda^{1-\alpha}}{\Gamma(1-\alpha,\lambda x_{\min})}$
	Exponential	$\mathrm{e}^{-\lambda x}$	$\lambda \mathrm{e}^{\lambda x_{\min}}$
	Stretched exponential	$x^{\beta-1}\mathrm{e}^{-\lambda x^{\beta}}$	$\beta\lambda \mathrm{e}^{\lambda x_{\min}^{\beta}}$
	Log-normal	$\frac{1}{x}\exp\left[-\frac{(\ln x-\mu)^2}{2\sigma^2}\right]$	$\sqrt{\frac{2}{\pi\sigma^2}}\left[\operatorname{erfc}\left(\frac{\ln x_{\min}-\mu}{\sqrt{2}\sigma}\right)\right]^{-1}$

E. APPENDIX E: WRF SIMULATION SPECIFICATIONS

WRF preprocessing system (WPS) variables as used in namelist.wps file. For further information, please see `https://anamika255.github.io/portfolio/5-WRF/`

&share

wrf core = 'ARW'

max dom = 3

start date = 2018-07-20_00:00:00

end date = 2018-08-09_00:00:00

interval seconds = 21600

io form geogrid = 2

&geogrid

parent id = 1, 1, 1,

parent grid ratio = 1, 3, 9,

i parent start = 1, 30, 52,

j parent start = 1, 20, 38,

e we = 162, 271, 163,

e sn = 126, 253, 163,

geog data res = '5m','5m','30s',

dx = 9000

dy = 9000

map proj = 'lambert'

ref lat = 50.1516

ref lon = 4.813

truelat1 = 50.1516

truelat2 = 0

stand lon = 4.813

WRF run variables as used in namelist.input file

&time_control

run days = 0,

run hours = 0,

run minutes = 0,

run seconds = 0,

start year = 2018, 2018, 2018,

start month = 07, 07, 07,

start day = 20, 20, 20,

start hour = 00, 00, 00,

end year = 2018, 2018, 2018,

end month = 08, 08, 08,

end day = 09, 09, 09,

end hour = 00, 00, 00,

interval seconds = 21600

input from file = .true.,.true.,.true.,

history interval = 180, 60, 60,

frames per outfile = 1000, 1000, 1000,

restart = .false.,

restart interval = 1440,

io form history = 2

io form restart = 2

io form input = 2

io form boundary = 2

&domains

time step = 36,

time step fract num = 0,

time step fract den = 1,

max dom = 3,

e we = 162, 271, 163,

e sn = 126, 253, 163,

e vert = 60, 60, 60,

p top requested = 5000,

num metgrid levels = 38,

num metgrid soil levels = 4,

dx = 9000, 3000, 1000,

dy = 9000, 3000, 1000,

grid id = 1, 2, 3,

parent id = 1, 1, 1,

i parent start = 1, 30, 52,

j parent start = 1, 20, 38,

parent grid ratio = 1, 3, 9,

parent time step ratio = 1, 3, 9,

feedback = 0,

smooth option = 0,

&physics

mp physics = 8, 8, 8, (New Thompson et al. scheme)

cu physics = 2, 0, 0, (Betts-Miller-Janjic scheme)

ra lw physics = 1, 1, 1, (Rapid Radiative Transfer Model scheme)

ra sw physics = 1, 1, 1, (Dudhia Scheme)

bl pbl physics = 2, 2, 2, (Mellor-Yamada-Janjic scheme)

sf sfclay physics = 2, 2, 2, (Eta similarity)

sf surface physics = 2, 2, 2, (Noah Land Surface Model)

radt = 10, 10, 10,

bldt = 0, 0, 0,

cudt = 0, 0, 0,

icloud = 1,

num land cat = 21, (MODIS Land Cover dataset)

sf urban physics = 2, 2, 2, (Building Environment Parameterization scheme)

surface input source = 1

&dynamics

hybrid opt = 2,

w damping = 0,

diff opt = 1, 1, 1,

km opt = 3, 3, 3, (Smagorinsky 3d deformation)

diff 6th opt = 0, 0, 0,

diff 6th factor = 0.12, 0.12, 0.12,

base temp = 290.

damp opt = 3,

zdamp = 5000., 5000., 5000.,

dampcoef = 0.2, 0.2, 0.2

khdif = 0, 0, 0,

kvdif = 0, 0, 0,

non hydrostatic = .true., .true., .true.,

moist adv opt = 1, 1, 1,

scalar adv opt = 1, 1, 1,

gwd opt = 1,

REFERENCES

[1] Melanie Prudhomme. World urbanization prospects: The 2018 revision. *UN Department of Public Information*, 2018. Available online: https://www.un.org/development/desa/en/news/population/2018-revision-of-world-urbanization-prospects.html.

[2] Timothy R Oke. *Boundary layer climates*. Routledge, 2002.

[3] Ian D Stewart and Tim R Oke. Local climate zones for urban temperature studies. *Bulletin of the American Meteorological Society*, 93(12):1879–1900, 2012.

[4] Timothy R Oke. The energetic basis of the urban heat island. *Quarterly Journal of the Royal Meteorological Society*, 108(455):1–24, 1982.

[5] Timothy R Oke. The distinction between canopy and boundary-layer urban heat islands. *Atmosphere*, 14(4):268–277, 1976.

[6] A John Arnfield. Two decades of urban climate research: a review of turbulence, exchanges of energy and water, and the urban heat island. *International Journal of Climatology*, 23(1):1–26, 2003.

[7] MW Rotach, Roland Vogt, Christian Bernhofer, Ekaterina Batchvarova, Andreas Christen, Alain Clappier, B Feddersen, S-E Gryning, G Martucci, Helmut Mayer, et al. Bubble–an urban boundary layer meteorology project. *Theoretical and Applied Climatology*, 81(3-4):231–261, 2005.

[8] M Roth, TR Oke, and WJ Emery. Satellite-derived urban heat islands from three coastal cities and the utilization of such data in urban climatology. *International Journal of Remote Sensing*, 10(11):1699–1720, 1989.

[9] James A Voogt and Tim R Oke. Thermal remote sensing of urban climates. *Remote Sensing of Environment*, 86(3):370–384, 2003.

[10] Annu Panwar, Axel Kleidon, and Maik Renner. Do surface and air temperatures contain similar imprints of evaporative conditions? *Geophysical Research Letters*, 2019.

[11] Fei Chen, Hiroyuki Kusaka, Robert Bornstein, Jason Ching, CSB Grimmond, Susanne Grossman-Clarke, Thomas Loridan, Kevin W Manning, Alberto Martilli, Shiguang Miao, et al. The integrated wrf/urban modelling system: development, evaluation, and applications to urban environmental problems. *International Journal of Climatology*, 31(2):273–288, 2011.

[12] Alberto Martilli, Alain Clappier, and Mathias W Rotach. An urban surface exchange parameterisation for mesoscale models. *Boundary-layer meteorology*, 104(2):261–304, 2002.

[13] Mattheos Santamouris. Cooling the cities–a review of reflective and green roof mitigation technologies to fight heat island and improve comfort in urban environments. *Solar energy*, 103:682–703, 2014.

[14] Neil Debbage and J Marshall Shepherd. The urban heat island effect and city contiguity. *Computers, Environment and Urban Systems*, 54:181–194, 2015.

[15] Brian Stone Jr and Michael O Rodgers. Urban form and thermal efficiency: how the design of cities influences the urban heat island effect. *American Planning Association. Journal of the American Planning Association*, 67(2):186, 2001.

[16] Benjamin Bechtel, Paul J Alexander, Jürgen Böhner, Jason Ching, Olaf Conrad, Johannes Feddema, Gerald Mills, Linda See, and Iain Stewart. Mapping local climate zones for a worldwide database of the form and function of cities. *ISPRS International Journal of Geo-Information*, 4(1):199–219, 2015.

[17] Jason Ching, G Mills, Benjamin Bechtel, ..., A. Shreevastava, et al. WUDAPT: An urban weather, climate, and environmental modeling infrastructure for the anthropocene. *Bulletin of the American Meteorological Society*, 2018.

[18] Benjamin Bechtel, Matthias Demuzere, Gerald Mills, Wenfeng Zhan, Panagiotis Sismanidis, Christopher Small, and James Voogt. Suhi analysis using local climate zonesa comparison of 50 cities. *Urban Climate*, 28:100451, 2019.

[19] Nina Schwarz and Ameur M Manceur. Analyzing the influence of urban forms on surface urban heat islands in europe. *Journal of Urban Planning and Development*, 141(3):A4014003, 2014.

[20] Karen C Seto and J Marshall Shepherd. Global urban land-use trends and climate impacts. *Current Opinion in Environmental Sustainability*, 1(1):89–95, 2009.

[21] Benoit B Mandelbrot. *The fractal geometry of nature*, volume 2. WH freeman New York, 1982.

[22] Michael Batty and Paul A Longley. *Fractal cities: a geometry of form and function*. Academic press, 1994.

[23] Yanguang Chen. Characterizing growth and form of fractal cities with allometric scaling exponents. *Discrete Dynamics in Nature and Society*, 2010, 2010.

[24] Hernán A Makse, José S Andrade, Michael Batty, Shlomo Havlin, H Eugene Stanley, et al. Modeling urban growth patterns with correlated percolation. *Physical Review E*, 58(6):7054, 1998.

[25] Soohyun Yang, Kyungrock Paik, Gavan S McGrath, Christian Urich, Elisabeth Krueger, Praveen Kumar, and P Suresh C Rao. Functional topology of evolving urban drainage networks. *Water Resources Research*, 53(11):8966–8979, 2017.

[26] Elisabeth Krueger, Christopher Klinkhamer, Christian Urich, Xianyuan Zhan, and P Suresh C Rao. Generic patterns in the evolution of urban water networks: Evidence from a large asian city. *Physical Review E*, 95(3):032312, 2017.

[27] Marta C Gonzalez, Cesar A Hidalgo, and Albert-Laszlo Barabasi. Understanding individual human mobility patterns. *Nature*, 453(7196):779, 2008.

[28] Hernán D Rozenfeld, Diego Rybski, José S Andrade, Michael Batty, H Eugene Stanley, and Hernán A Makse. Laws of population growth. *Proceedings of the National Academy of Sciences*, pages pnas–0807435105, 2008.

[29] Luis Bettencourt and Geoffrey West. A unified theory of urban living. *Nature*, 467(7318):912, 2010.

[30] Alexander Buyantuyev and Jianguo Wu. Urban heat islands and landscape heterogeneity: linking spatiotemporal variations in surface temperatures to land-cover and socioeconomic patterns. *Landscape Ecology*, 25(1):17–33, 2010.

[31] Weiqi Zhou, Ganlin Huang, and Mary L Cadenasso. Does spatial configuration matter? understanding the effects of land cover pattern on land surface temperature in urban landscapes. *Landscape and Urban Planning*, 102(1):54–63, 2011.

[32] Hua Liu and Qihao Weng. Scaling effect on the relationship between landscape pattern and land surface temperature. *Photogrammetric Engineering & Remote Sensing*, 75(3):291–304, 2009.

[33] S Lovejoy and D Schertzer. Scale invariance, symmetries, fractals, and stochastic simulations of atmospheric phenomena. *Bulletin of the American Meteorological Society*, 67(1):21–32, 1986.

[34] Qihao Weng. Fractal analysis of satellite-detected urban heat island effect. *Photogrammetric Engineering & Remote Sensing*, 69(5):555–566, 2003.

[35] Dietrich Stauffer and Ammon Aharony. *Introduction to percolation theory: revised second edition*. CRC press, 2014.

[36] M Sahimi and M Sahimi. *Applications of percolation theory*. CRC Press, 2014.

[37] Michael B Isichenko. Percolation, statistical topography, and transport in random media. *Reviews of Modern Physics*, 64(4):961, 1992.

[38] MB Isichenko and J Kalda. Statistical topography. i. fractal dimension of coastlines and number-area rule for islands. *Journal of Nonlinear Science*, 1(3):255–277, 1991.

[39] Attila R Imre and Josef Novotnỳ. Fractals and the korcak-law: a history and a correction. *The European Physical Journal H*, 41(1):69–91, 2016.

[40] Benoit B Mandelbrot. Stochastic models for the earth's relief, the shape and the fractal dimension of the coastlines, and the number-area rule for islands. *Proceedings of the National Academy of Sciences*, 72(10):3825–3828, 1975.

[41] B Barry Cael and David A Seekell. The size-distribution of earths lakes. *Scientific Reports*, 6:29633, 2016.

[42] Ignacio Rodriguez-Iturbe and Andrea Rinaldo. *Fractal river basins: chance and self-organization*. Cambridge University Press, 2001.

[43] Lionel Roy Taylor. Aggregation, variance and the mean. *Nature*, 189(4766):732–735, 1961.

[44] Zoltán Eisler, Imre Bartos, and János Kertész. Fluctuation scaling in complex systems: Taylor's law and beyond. *Advances in Physics*, 57(1):89–142, 2008.

[45] M Argollo De Menezes and A-L Barabási. Fluctuations in network dynamics. *Physical review letters*, 92(2):028701, 2004.

[46] A. Shreevastava, P.S.C. Rao, and G.S. McGrath. Spatial analysis of the surface urban heat island. *Land Surface and Cryosphere Remote Sensing*, 10777, 2018.

[47] Leonardo E Bertassello, P Suresh C Rao, James W Jawitz, Gianluca Botter, Phong VV Le, Praveen Kumar, and Antoine F Aubeneau. Wetlandscape fractal topography. *Geophysical Research Letters*, 45(14):6983–6991, 2018.

[48] Murray C Peel, Brian L Finlayson, and Thomas A McMahon. Updated world map of the köppen-geiger climate classification. *Hydrology and Earth System Sciences*, 4(2):439–473, 2007.

[49] Michele Lazzarini, Prashanth Reddy Marpu, and Hosni Ghedira. Temperature-land cover interactions: The inversion of urban heat island phenomenon in desert city areas. *Remote Sensing of Environment*, 130:136–152, 2013.

[50] Clémentine Cottineau, Erez Hatna, Elsa Arcaute, and Michael Batty. Diverse cities or the systematic paradox of urban scaling laws. *Computers, environment and urban systems*, 63:80–94, 2017.

[51] Noel Gorelick, Matt Hancher, Mike Dixon, Simon Ilyushchenko, David Thau, and Rebecca Moore. Google earth engine: Planetary-scale geospatial analysis for everyone. *Remote Sensing of Environment*, 202:18–27, 2017.

[52] Jakub P Walawender, Monika J Hajto, and Piotr Iwaniuk. A new arcgis toolset for automated mapping of land surface temperature with the use of landsat satellite data. In *Geoscience and Remote Sensing Symposium (IGARSS), 2012 IEEE International*, pages 4371–4374. IEEE, 2012.

[53] Aaron Clauset, Cosma Rohilla Shalizi, and Mark EJ Newman. Power-law distributions in empirical data. *SIAM Review*, 51(4):661–703, 2009.

[54] Mark EJ Newman. Power laws, pareto distributions and zipf's law. *Contemporary Physics*, 46(5):323–351, 2005.

[55] Christopher Klinkhamer, Elisabeth Krueger, Xianyuan Zhan, Frank Blumensaat, Satish Ukkusuri, and P Suresh C Rao. Functionally fractal urban networks: Geospatial co-location and homogeneity of infrastructure. *arXiv preprint arXiv:1712.03883*, 2017.

[56] Marc Barthelemy. *The structure and dynamics of cities*. Cambridge University Press, 2016.

[57] Michael Batty. The size, scale, and shape of cities. *science*, 319(5864):769–771, 2008.

[58] Till Fluschnik, Steffen Kriewald, Anselmo García Cantú Ros, Bin Zhou, Dominik E Reusser, Jürgen P Kropp, and Diego Rybski. The size distribution, scaling properties and spatial organization of urban clusters: a global and regional percolation perspective. *ISPRS International Journal of Geo-Information*, 5(7):110, 2016.

[59] Kausik Gangopadhyay and B Basu. City size distributions for india and china. *Physica A: Statistical Mechanics and its Applications*, 388(13):2682–2688, 2009.

[60] Roy E Plotnick, Robert H Gardner, William W Hargrove, Karen Prestegaard, and Martin Perlmutter. Lacunarity analysis: a general technique for the analysis of spatial patterns. *Physical review E*, 53(5):5461, 1996.

[61] Roy E Plotnick, Robert H Gardner, and Robert V O'Neill. Lacunarity indices as measures of landscape texture. *Landscape ecology*, 8(3):201–211, 1993.

[62] Tim R Oke. City size and the urban heat island. *Atmospheric Environment (1967)*, 7(8):769–779, 1973.

[63] KW Oleson, A Monaghan, O Wilhelmi, M Barlage, N Brunsell, J Feddema, L Hu, and DF Steinhoff. Interactions between urbanization, heat stress, and climate change. *Climatic Change*, 129(3-4):525–541, 2015.

[64] Nina Schwarz, Uwe Schlink, Ulrich Franck, and Katrin Großmann. Relationship of land surface and air temperatures and its implications for quantifying urban heat island indicatorsan application for the city of leipzig (germany). *Ecological Indicators*, 18:693–704, 2012.

[65] James A Henry, Orjan F Wetterqvist, Stephen J Roguski, and Steven E Dicks. Comparison of satellite, ground-based, and modeling techniques for analyzing the urban heat island. *Photogrammetric Engineering and Remote Sensing*, 55(1):69–76, 1989.

[66] Susan L Cutter, Christopher T Emrich, Jennifer J Webb, and Daniel Morath. Social vulnerability to climate variability hazards: A review of the literature. *Final Report to Oxfam America*, 5:1–44, 2009.

[67] Kathryn Bradford, Leslie Abrahams, Miriam Hegglin, and Kelly Klima. A heat vulnerability index and adaptation solutions for pittsburgh, pennsylvania. *Environmental Science & Technology*, 49(19):11303–11311, 2015.

[68] Lei Zhao, Michael Oppenheimer, Qing Zhu, Jane W Baldwin, Kristie L Ebi, Elie Bou-Zeid, Kaiyu Guan, and Xu Liu. Interactions between urban heat islands and heat waves. *Environmental research letters*, 13(3):034003, 2018.

[69] Dan Li and Elie Bou-Zeid. Synergistic interactions between urban heat islands and heat waves: the impact in cities is larger than the sum of its parts. *Journal of Applied Meteorology and Climatology*, 52(9):2051–2064, 2013.

[70] Dan Li, Ting Sun, Maofeng Liu, Long Yang, Linlin Wang, and Zhiqiu Gao. Contrasting responses of urban and rural surface energy budgets to heat waves explain synergies between urban heat islands and heat waves. *Environmental Research Letters*, 10(5):054009, 2015.

[71] Lei Zhao, Xuhui Lee, Ronald B Smith, and Keith Oleson. Strong contributions of local background climate to urban heat islands. *Nature*, 511(7508):216, 2014.

[72] Gabriele Manoli, Simone Fatichi, Markus Schläpfer, Kailiang Yu, Thomas W Crowther, Naika Meili, Paolo Burlando, Gabriel G Katul, and Elie Bou-Zeid. Magnitude of urban heat islands largely explained by climate and population. *Nature*, 573(7772):55–60, 2019.

[73] Michael Batty. *The new science of cities*. Mit Press, 2013.

[74] Ahmed Mustafa, Alison Heppenstall, Hichem Omrani, Ismail Saadi, Mario Cools, and Jacques Teller. Modelling built-up expansion and densification with multinomial logistic regression, cellular automata and genetic algorithm. *Computers, Environment and Urban Systems*, 67:147–156, 2018.

[75] Elmira Jamei, Priyadarsini Rajagopalan, Mohammadmehdi Seyedmahmoudian, and Yashar Jamei. Review on the impact of urban geometry and pedestrian level greening on outdoor thermal comfort. *Renewable and Sustainable Energy Reviews*, 54:1002–1017, 2016.

[76] Mohammad Taleghani, Laura Kleerekoper, Martin Tenpierik, and Andy van den Dobbelsteen. Outdoor thermal comfort within five different urban forms in the netherlands. *Building and environment*, 83:65–78, 2015.

[77] E Andreou. Thermal comfort in outdoor spaces and urban canyon microclimate. *Renewable Energy*, 55:182–188, 2013.

[78] JM Sobstyl, T Emig, MJ Abdolhosseini Qomi, F-J Ulm, and RJ-M Pellenq. Role of city texture in urban heat islands at nighttime. *Physical review letters*, 120(10):108701, 2018.

[79] Brian Stone, Jeremy J Hess, and Howard Frumkin. Urban form and extreme heat events: are sprawling cities more vulnerable to climate change than compact cities? *Environmental health perspectives*, 118(10):1425, 2010.

[80] Bin Zhou, Diego Rybski, and Jürgen P Kropp. The role of city size and urban form in the surface urban heat island. *Scientific Reports*, 7(1):4791, 2017.

[81] Claes Andersson, Koen Frenken, and Alexander Hellervik. A complex network approach to urban growth. *Environment and Planning A*, 38(10):1941–1964, 2006.

[82] Albert-László Barabási and Réka Albert. Emergence of scaling in random networks. *science*, 286(5439):509–512, 1999.

[83] Luis A Nunes Amaral, Antonio Scala, Marc Barthelemy, and H Eugene Stanley. Classes of small-world networks. *Proceedings of the national academy of sciences*, 97(21):11149–11152, 2000.

[84] Nahid Mohajeri, Agust Gudmundsson, and Jean-Louis Scartezzini. Expansion and densification of cities: linking urban form to ecology. In *Proceedings of International Conference CISBAT 2015 Future Buildings and Districts Sustainability from Nano to Urban Scale*, number CONF, pages 475–480. LESO-PB, EPFL, 2015.

[85] Nina Schwarz, Sven Lautenbach, and Ralf Seppelt. Exploring indicators for quantifying surface urban heat islands of european cities with modis land surface temperatures. *Remote Sensing of Environment*, 115(12):3175–3186, 2011.

[86] A. Shreevastava, P.S.C. Rao, and G.S. McGrath. Emergent self-similarity and scaling properties of fractal intra-urban heat islets for diverse global cities. *Physical Reviews E*, 2019.

[87] Peter J Robinson. On the definition of a heat wave. *Journal of Applied Meteorology*, 40(4):762–775, 2001.

[88] Gerald A Meehl and Claudia Tebaldi. More intense, more frequent, and longer lasting heat waves in the 21st century. *Science*, 305(5686):994–997, 2004.

[89] P Ramamurthy, D Li, and E Bou-Zeid. High-resolution simulation of heatwave events in new york city. *Theoretical and applied climatology*, 128(1-2):89–102, 2017.

[90] G Brooke Anderson and Michelle L Bell. Lights out: impact of the august 2003 power outage on mortality in new york, ny. *Epidemiology (Cambridge, Mass.)*, 23(2):189, 2012.

[91] Karen C Seto, Anette Reenberg, Christopher G Boone, Michail Fragkias, Dagmar Haase, Tobias Langanke, Peter Marcotullio, Darla K Munroe, Branislav Olah, and David Simon. Urban land teleconnections and sustainability. *Proceedings of the National Academy of Sciences*, 109(20):7687–7692, 2012.

[92] Emily Black, Mike Blackburn, Giles Harrison, Brian Hoskins, and John Methven. Factors contributing to the summer 2003 european heatwave. *Weather*, 59(8):217–223, 2004.

[93] P Ramamurthy and E Bou-Zeid. Heatwaves and urban heat islands: a comparative analysis of multiple cities. *Journal of Geophysical Research: Atmospheres*, 122(1):168–178, 2017.

[94] Rahul Kumar, Vimal Mishra, Jonathan Buzan, Rohini Kumar, Drew Shindell, and Matthew Huber. Dominant control of agriculture and irrigation on urban heat island in india. *Scientific reports*, 7(1):1–10, 2017.

[95] Rahul Kumar and Vimal Mishra. Decline in surface urban heat island intensity in india during heatwaves. *Environmental Research Communications*, 1(3):031001, 2019.

[96] William H Press, Saul A Teukolsky, Brian P Flannery, and William T Vetterling. *Numerical recipes in Fortran 77: volume 1, volume 1 of Fortran numerical recipes: the art of scientific computing*. Cambridge university press, 1992.

[97] Daniel Harris, Efi Foufoula-Georgiou, Kelvin K Droegemeier, and Jason J Levit. Multiscale statistical properties of a high-resolution precipitation forecast. *Journal of Hydrometeorology*, 2(4):406–418, 2001.

[98] Kevin Pollock. Urban physics. *Nature*, 531(7594 S1):S64–S64, 2016.

[99] S Lovejoy. Area-perimeter relation for rain and cloud areas. *Science*, 216(4542):185–187, 1982.

[100] Marie S Oneill and Kristie L Ebi. Temperature extremes and health: impacts of climate variability and change in the united states. *Journal of Occupational and Environmental Medicine*, 51(1):13–25, 2009.